Design of a Silicon Microfabricated Rocket Engine Turbopump

by

Antoine Deux

Diplôme d'Ingénieur, Ecole Polytechnique, France (1998)

Submitted to the Department of Aeronautics and Astronautics
in partial fulfillment of the requirements for the degree of

MASTER OF SCIENCE

at the

MASSACHUSETTS INSTITUTE OF TECHNOLOGY

June 2001

Author .....
Department of Aeronautics and Astronautics
May 25, 2001

Certified by .....
Professor Alan H. Epstein
R.C. Maclaurin Professor of Aeronautics and Astronautics
Thesis Supervisor

Accepted by .....
Professor Wallace E. Vander Velde
Professor of Aeronautics and Astronautics
Chair, Committee on Graduate Students

Design of a Silicon Microfabricated Rocket Engine Turbopump

by

Antoine Deux

Submitted to the Department of Aeronautics and Astronautics
on May 25, 2001, in partial fulfillment of the
requirements for the degree of
MASTER OF SCIENCE

Abstract

The advances in silicon microfabrication technology suggest the feasibility of high-precision mechanical devices for power conversion. This thesis describes the design of a silicon demonstration turbopump for a micro-rocket engine, and the analysis and experimental investigation of liquid bearings that may be implemented in a future turbopump.

Liquid micro-scale lubrication is investigated. Models are developed to predict the performance of hydrostatic liquid thrust bearings, and hydrostatic and hydrodynamic liquid journal bearings. These models suggest that liquid operation of the existing micro-bearing rig is feasible. This device was tested with water to assess the bearings performance. The maximum speed achieved was 21,000 revolutions per minute, and was limited by the drag in this device designed for gas operation.

A micro-scale turbopump producing a pressure rise of 30 atm for water was designed, as a demonstration of this concept for fluid pressurization in the rocket engine system. This thesis addresses several of the key design trades and identifies the fundamental engineering issues. This micropump integrates high-speed turbomachinery and micro-gas bearings. An innovative arrangement is proposed with coplanar pump and turbine for ease of fabrication and reduction of imbalance.

Thesis Supervisor: Professor Alan H. Epstein
Title: R.C. Maclaurin Professor of Aeronautics and Astronautics

Acknowledgments

My graduate experience and the results of this research would not be what they are without the contributions of many people. I first extend my gratitude to Professor Alan Epstein for giving me the opportunity to live a unique graduate experience, for mentoring me, and for his support and encouragement during the periods of doubt. I also wish to thank Professors Jack Kerrebrock and John Brisson for providing valuable guidance.

I also had the privilege to work with an exceptional group of researchers and students. I am grateful to Dr Stuart Jacobson and Dr Fred Ehrich for the numerous discussions on bearings and insightful suggestions on design; Dr Xin Zhang and Dr Yoav Peles for their insight in microfabrication; Dr Luc Frechette for sharing simply his knowledge; Dr Gerald Guenette for his help in testing; Baudoin Philippon for his help in turbine design; Chee-Wei Wong for his help on bearings experiments; Sumita Pennathur for her good humor and for energy to put things together so fast in our common test rig; Laurent Jamonet for helping me in the turbopump design; Chiang-Juay Teo for letting me steal all his testing equipment; James Letendre, Jack Costa and Victor Dubrowski for their invaluable help in every obscur technical aspect of the experiment; Diana Park for the 3D rendering after each design I promised would be the last one; Lori, for keeping us well fed. I am also grateful to Chris, Carole, Erin, Shaun for their contributions to the micro-rocket program.

My experience at MIT would not have been that unforgettable journey without the friendship of so many, and most importantly the unconditional love from Marie. Thank you all.

This research was sponsored by DARPA. This support is gratefully acknowledged.

Contents

List of Figures

List of Tables

Nomenclature

Roman

A	Area, usually a cross-sectional flow area (m^2)
C	Chord (of a blade) (m)
C_D	Discharge coefficient
C_P	Specific heat (J.kg.K)
D	diameter (m)
D_h	Hydraulic diameter (m)
F	Force (N)
I_{sp}	Specific impulse (s)
L	Length (m)
M	Mach number
$\overline{M}$	Non-dimensional mass $(\overline{M}) = \frac{mP_a\psi^5}{72L\mu^2}$
P	Pressure (Pa or atm or psi) and power (W)
R	Gas constant and rotor radius (m) and resistance and turbine reaction
S	Stiffness (N.m)
T	Temperature (K)
W_r	Sommerfeld number $W_r = \frac{w_r}{\mu\omega r L}\psi^2$
c	Celerity of sound ($m.s^{-1}$) and bearing clearance (m)
dP	Axial differential pressure (psi)
e	Distance between bearing and journal centers (m)
f	Lens focal distance (m) and friction factor
$f_{/n}$	Lens focal number

g	Acceleration of gravity ($m.s^{-3}$) and thrust bearing gap (m)
h	Target optical diameter or enthalpy or blade height (m)
h''	Source optical diameter
l	Length (m)
m	Mass (kg) and optical magnification
$\dot{m}$	Mass flow ($kg.s^{-1}$)
r	Radius (m)
s	Distance lens - target
s''	Distance source - lens
u	Radial velocity ($m.s^{-1}$)
v	Tangential velocity ($m.s^{-1}$)
w	Resultant load in a journal bearing (N)
w'	Load per unit length

Greek

Λ	Non-dimensional bearing number $\Lambda = \frac{6\mu\omega}{\psi^2 P_a}$
Ω	Rotational frequency (Hz)
Ω_n	Whirl frequency (Hz)
Π	Pressure ratio
α	Pump backsweep angle (rad)
β	Swirl angle
γ	Specific heat ratio (gas constant), C_p/C_v
ϵ	Eccentricity ratio (axial or radial)
ζ	Load parameter $\zeta = \frac{w_r}{2rLP_a}$
η	Efficiency
λ	Wavelength
μ	Viscosity ($\mathrm{kg.m^{-1}.s^{-1}}$)
π	Pressure ratio
ϕ	Attitude angle (rad)
ρ	Fluid density ($\mathrm{kg.m^{-3}}$)
σ	Shear stress (Pa)
τ	Temperature ratio
ω	Angular velocity ($\mathrm{rad.s^{-1}}$)
ψ	Clearance to radius ratio $\psi = \frac{c}{R}$

Subscripts

1	At the pump blades leading edge
2	At the pump blades trailing edge
P	Pump
Po	Pump exit
T	Total
TBi	At the thrust bearing inside (for an annular geometry)
TBo	At the thrust bearing outside
a	Ambient
atb	Aft thrust bearing
b	At the turbine blade trailing edge
c	At the turbine blade leading edge
cap	Capillaries
ftb	Forward thrust bearing
in	At the inlet
inh	Inherent
ir	Interrow
min	Minimum
n	Whirl
$orif$	Orifices
r	Radial
rad	Radial
s	Static
sat	Saturation
$srad\_in$	Static at the inlet of the radial gap area
t	Tangential
tb	Thrust bearings
$visc$	Viscous

Acronyms

$1D$	one-dimensional
$2D$	two-dimensional
$3D$	three-dimensional
ATB	Aft thrust bearing
CFD	Computational fluid dynamics
DAQ	Data acquisition system
$DRIE$	Deep reactive ion etching
FTB	Forward thrust bearing
JB	Journal bearing
JPP	Journal pressurization plenum
$MCBR$	Motor compressor bearing rig
$MEMS$	Micro electro mechanical systems
MOP	Motor Outer Plenum
rpm	Rotations per minute

Chapter 1

Introduction

Made with the same silicon fabrication methods used to produce computer chips, micro-electromechanical systems (or MEMS) have over the last decade become well embedded in the high-tech landscape. MEMS offer large functionality and can offer a substantial cost advantage due to their fabrication technology. Current commercially exploited MEMS are low power, low energy devices, such as those used in automobile airbags, inkjet printers, pressure sensors.

A new class of MEMS devices, *power-MEMS*, have been investigated over the past few years [4]. They are silicon fabricated energy conversion microsystems. High speed rotating machinery is required to achieve high performance and power densities equivalent to those in the best large-sized machines produced today. Single-crystal silicon offers excellent structural characteristics for such applications. Its high strength-to-density ratio enables high rotating speeds.

The focus of this work is to design a demonstration millimeter-scale liquid turbopump and investigate the behavior of liquid microbearings as an enabling technology required for a micro-rocket engine. The realization of power MEMS presents new challenges to traditional disciplines, and low friction fluidic bearings are required to support the rotor. The demonstration micro-turbopump designed and fabricated in the focus of this work is part of the proof of the feasibility of this pumping system.

This chapter first briefly describes the work on-going at MIT in the power MEMS area, and then discusses the turbopump motivation and objectives.

1.1 The MIT Micro Gas Turbine and Micro Rocket Engine projects

Two power MEMS projects are on-going at MIT, referred as the Micro-gas engine and Micro-rocket projects.

The micro-engine concept was proposed in 1994 by Epstein *et al.* [3]. As shown in Figure 1-1, the baseline device is a centimeter-scale gas turbine engine for propulsion of Micro Air Vehicles or power generation. A demonstration micro-engine producing 10 grams of thrust was designed by Protz [34].

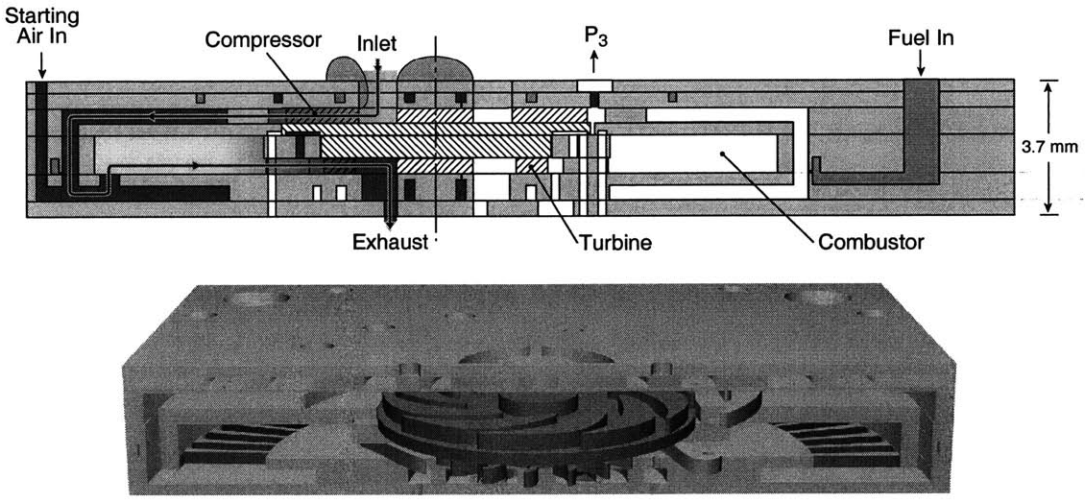

Figure 1-1: Baseline design for the MIT microengine. Demo engine cross-section at two different radial locations, and 3D section of the demo engine. (Illustration courtesy of Diana Park)

The micro-rocket engine concept was proposed and investigated by London [26]. The complete system is illustrated conceptually in Figure 1-2. The rocket thrust is 15 N at a mass flow of 5 g/s and I_{sp} of 300 sec [26]. The three primary components of a microrocket system are the valves, the pressurization system, and the cooled thrust chamber. A six-wafer stack demonstration cooled thrust chamber has been designed, fabricated, packaged, and tested.

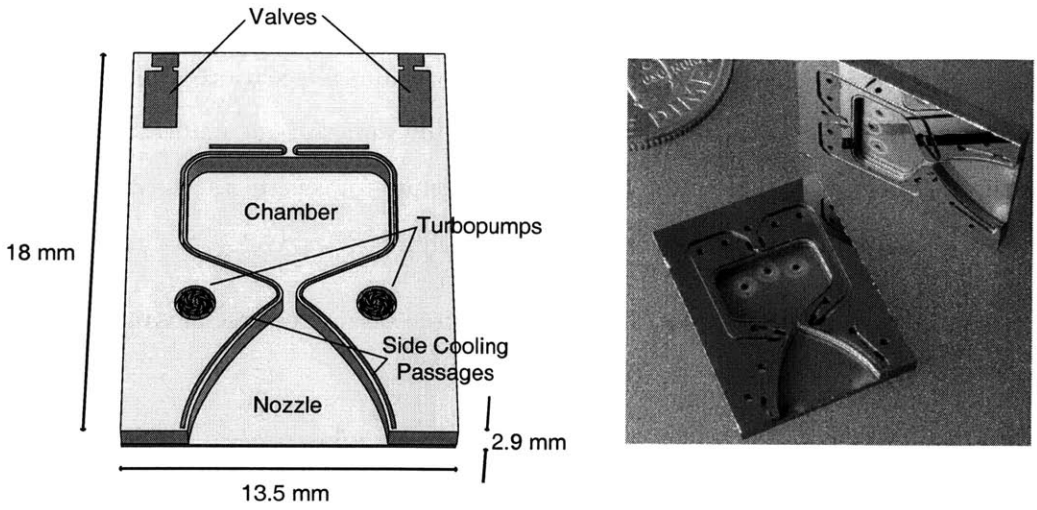

Figure 1-2: Conceptual view of the location of the various micro rocket system components, and picture of the thrust chamber before bonding. (Illustration courtesy of Diana Park)

1.2 Micro turbopump for the rocket engine

In liquid propellant rocket engines, the propellant must be fed into the combustion chamber at a high pressure. The two general types of propellant feed approaches are gas-pressure and turbopump systems. A turbopump feed system uses pumps to pressurize the propellants. These pumps are driven by turbines, which are themselves driven by the expansion of hot gas. A turbopump feed system has been selected for the microrocket engine [5]. Turbopump feed systems differ in the cycle they employ. An expander cycle was chosen for simplicity [33].

1.3 Motivation and objectives

Previous work on the micro rocket engine has focused on the cooled thrust chamber. Liquid valves have not yet been investigated. Preliminary investigation of the pumping system has been documented in [5, 33, 26].

The focus of this thesis is the turbopump. The required pressure at the inlet to the cooling passages and therefore at the pump exit is 300 atm. The primary objective of this work is to demonstrate the feasibility of the turbopump concept. To do so, a micro-scale turbopump producing a pressure rise of 30 atm for water has been designed. For this first design, the turbopump is not strictly considered as part of the rocket system but is rather

of proof-of-concept device .

Realizing such a device is a challenge for modelling and fabrication of high-speed turbomachinery, high speed fluid bearings, and in modelling micro-scale cavitation. To demonstrate the technology necessary for the rocket turbopump, several main components were chosen for individual demonstration :

- a cavitation cascade: Pennathur [31] has focused on micro-scale cavitation modelling, and experiments using a static cascade.
- liquid bearings: The integrated turbopump may require liquid bearings. One objective of this thesis is to model and demonstrate liquid micro bearing operation.

1.4 Organisation of Thesis

This chapter has introduced the concept of a micro gas turbine engine and a microrocket engine, and motivated the development of a demonstration turbopump, including the investigation of liquid microscale bearings.

Chapter Two describes the liquid bearing modelling effort. It addresses thrust and journal bearings. The behavior of an existing device, the micro bearing rig, in a liquid environment is analyzed.

Chapter Three describes the experimental apparatus that was used to test the liquid micro-bearing devices.

Chapter Four presents the results of the liquid bearing experiments.

Chapter Five presents the overall system design and layout of the demonstration turbopump.

Chapter Six concludes the thesis. A summary of the research, the contributions and recommendations for future work on this area are presented.

Chapter 2

Bearings and Rotor Dynamics : Theory

2.1 Introduction

The micro-gas turbine and micro-rocket engine turbomachinery require high rotational speeds in order to achieve high power densities. Low friction bearings are required to support the rotor against fluid forces, rotor dynamics, and externally applied accelerations while operating at speeds of the order of a million rotations per minute (rpm) . For the micro-gas turbine, gas film, electrical, and hybrid gas-electrical bearing concepts had been examined [28]. Gas lubricated bearings were selected on the basis of superior load bearing capability, low friction and relative ease of fabrication, and have been successfully operated at high speeds [42].

A pair of thrust bearings support the axial loads on the rotor. A journal bearing supports the radial loads.

To minimize technical risk, the micro-rocket engine project utilizes as much micro-engine gas turbine technology as possible, thus the same kind of bearing was selected. Since the micro-rocket runs with liquid propellants, both liquid or gas bearings could be used to support the turbomachinery rotor. Since micro gas bearings have been explored in some detail [28, 25, 42], this chapter examines the feasibility of using liquid bearings at this length scale.

Fluid lubricated bearings have two distinct modes of operation :

Hydrostatic In the hydrostatic bearing, fluid is supplied from an external source to form a lubrication film. The stiffness of the film is provided by the restoring pressure forces acting on the rotor, when displaced from equilibrium. Stiffness creation mechanisms are detailed in the following sections.

Hydrodynamic The hydrodynamic bearing is self-acting. The rotor system acts as a viscous pump: a pressure distribution in the bearing is obtained from the motion of the rotor. It can create stiffness to enable stable operation.

Both modes are considered herein. Special focus is given on liquid bearings that need to be investigated for the micro-rocket engine turbopump.

2.2 Thrust Bearings

The previous rotating devices designed and fabricated in the focus of the micro-engine project use a pair of hydrostatic gas thrust bearings as proposed by Lin [25]. The following sections describe the operation and the design parameters of these bearings. Liquid thrust bearings are then investigated. Operation of the micro-bearing rig with water is analyzed, and a liquid thrust bearing design is proposed. Wong [42] has recently demonstrated hydrodynamic thrust bearings using a self-acting spiral groove design. This kind of bearing is not considered herein.

2.2.1 Hydrostatic thrust bearing operation

Pressurized fluid is supplied to a plenum. As described above, the stiffness creation mechanism is linked to resistances to the flow, which entail pressure drops.

The fluid flows through two elements in series: a number of axial orifices (capillaries) and a radial outflow gap between the rotor and the stator as shown in Figure 2-1. As can be seen, the bearing total gap is defined as the sum of the distances between the front and aft sides of the rotor and their facing stator, and the axial eccentricity is the ratio of the rotor axial displacement from the center to half of the bearing total gap. The pressure drop results from the flow resistance of the capillaries, the turning of the flow from the capillaries into a much smaller gap between the stationery and rotating bearing members (inherent resistance), and the radial outflow resistance. The capillaries present a fixed resistance to

the flow. The radial outflow resistance varies with the axial eccentricity of the rotor. This variable resistance creates a restoring axial pressure force on the rotor [13]: a smaller gap results in a smaller flow, thus in a smaller pressure drop in the orifices where the resistance is fixed, and then in a larger pressure on the considered side of the rotor. The inherent resistance will increase with decreasing bearing gap, but its variation is smaller than the radial flow resistance if designed correctly [25].

The axial stiffness is computed from these restoring forces coming from both thrust bearings.

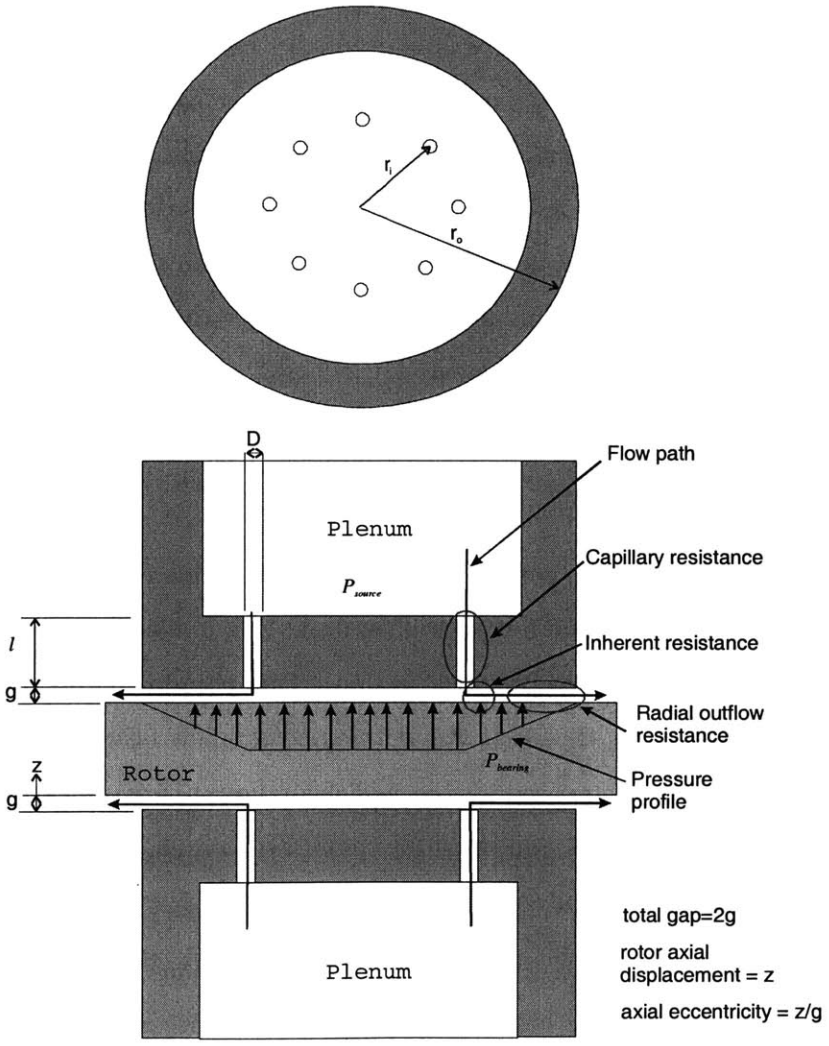

Figure 2-1: Schematic of hydrostatic thrust bearings (from Fréchette [13])

2.2.2 Design parameters

The key design parameters of the hydrostatic thrust bearings are the capillary diameter D, the length l and the bearing gap g. The rotor axial position is defined as axial eccentricity, which is axial displacement normalized by bearing gap.

The thrust bearing design goals are to maximize the axial stiffness, to obtain a sufficient load for balance, and to minimize the viscous drag.

The existing rotating micro devices were designed with a back plenum, so that the net axial load on the rotor at steady state is zero, without considering the action of the thrust bearings. The thrust bearings are intended to provide a restoring axial stiffness, which must overcome the destabilizing pressure forces or operation induced loads. The axial stiffness is maximal when roughly half the pressure drop occurs in the capillaries [13].

The thrust bearings must support a load large enough to overcome a change in pressure distribution during a transient (e.g., during a rotor acceleration). Yet, they do not support load at steady-state where the axial eccentricity is kept close to zero, but only supply stiffness. Therefore, a design goal is to maximize the load from the thrust bearings on the rotor at a 'limit' eccentricity[1]. This load has to be larger than any force variation that might occur on the rotor during a transient.

Finally, the drag in the gap area has to be considered. The flow in this region can be modelled as a Couette flow.

Design parameter studies are conducted using a combination of flow restriction models developed by Jacobson [20]. The forces, stiffness and flow rates are calculated from the three resistances described in the previous section. This pseudo-compressible model was investigated as a focus of this thesis. It was automated to allow faster parameter analysis, and transformed both to an incompressible model for liquid thrust bearings analysis as describes in the following section, and to a fully compressible model by including the proper definition of compressible total pressure,

$$P_T = P_s \times \left(1 + \frac{\gamma - 1}{2} \times M^2\right)^{\frac{\gamma}{\gamma - 1}}, \tag{2.1}$$

instead of the sum of static pressure plus dynamic pressure, which is only valid at low Mach

[1]This limit eccentricity is the empirical border of the safe operating range. A value of 0.4 has been assumed here [20].

number. A detailed description of this model is given in Appendix A.

2.2.3 Liquid thrust bearings

Liquid hydrostatic thrust bearings were investigated, since they could be used in a micro-rocket engine turbopump. Analysis is performed considering a static rotor. The pressures involved in the thrust bearings are larger than atmospheric, and thus do not allow for cavitation. Thus, liquid thrust bearings differ from gas thrust bearings in terms of viscosity and compressibility.

An incompressible model was developed, using the same flow restrictions models as described in the previous sections. These models yield the following pressure distribution on the rotor (on one side) :

$$P = \begin{cases} P_{srad\_in} & \text{if } r < r_o \\ P_{srad\_in} - \frac{6\mu\dot{m}}{g^3\rho\pi} \log(\frac{r}{r_i}) & \text{if } r_o < r < r_i \end{cases}$$

where P_{srad_in} is the static pressure at the inlet of the radial gap area. The force on the rotor is obtained by integration of this pressure distribution.

Results for the micro-bearing rig geometry are presented hereafter. The micro-bearing rig geometry is detailed in Section 2.4.1, and the thrust bearing geometry is described in Table 2.1.

Stiffness and mass flow rate

Figure 2-2 shows the axial stiffness derived from the thrust bearings in the micro-bearing rig geometry, and the corresponding total mass flow. These data are characteristic predictions, and not operating predictions, since they simulate a zero-eccentricity rotor, blocked in this position. Data for water are obtained with the incompressible model, and data for air with the fully compressible model. As can be seen, higher pressures are necessary in the liquid system to obtain the same stiffness as in a gas system, for a stiffness larger than $2.10^5 N/m$. This results in a much higher flow rate.

Both for liquid and for gas, the Reynolds number in the capillary is an order of magnitude higher than in the radial area. Second, at a given location, the Reynolds number in the gas bearing is an order of magnitude greater than in the liquid case. The pressure drop scales

Table 2.1: Thrust bearing geometry for the micro bearing rig

Forward thrust bearing	Axial gap	1.5 μm
	Number of orifices	14
	Location of orifices	0.55 mm
	Outer pad radius	0.7 mm
	Orifice diameter	11 μm
	Orifice length	100 μm
Aft thrust bearing	Axial gap	1.5 μm
	Number of orifices	18
	Location of orifices	0.55 mm
	Outer pad radius	0.9 mm
	Orifice diameter	11 μm
	Orifice length	100 μm

with the Reynolds number, and the stiffness is associated with the variation in pressure drop in the radial area when the rotor is slightly displaced axially. Consequently, the gas and liquid systems behave differently, and there is no simple physical explanation for the stiffness differences. The velocities in the gas case are found to be two order of magnitudes larger than in the liquid case, which suggests that the mass flow should be an order of magnitude lower as verified.

Operating map

The operating map of the water thrust bearings was investigated. Figure 2-3 presents the iso-stiffness and iso-eccentricity lines for the micro-bearing rig rotor in equilibrium (i.e., the net force is zero) under the action of two water hydrostatic thrust bearings. Empirical data suggests a desired axial stiffness of $3.10^5 N/m$ for high-speed operation [20]. Positive pressure forces will develop on the front side of the rotor while spinning, because of the pumping pressure. Thus, a slightly positive axial eccentricity (of 0.1 to 0.2) is desired at equilibrium under the sole contribution of the thrust bearings, so that the rotor is axially centered during operation. As can be seen from Figure 2-3, these requirements lead to the

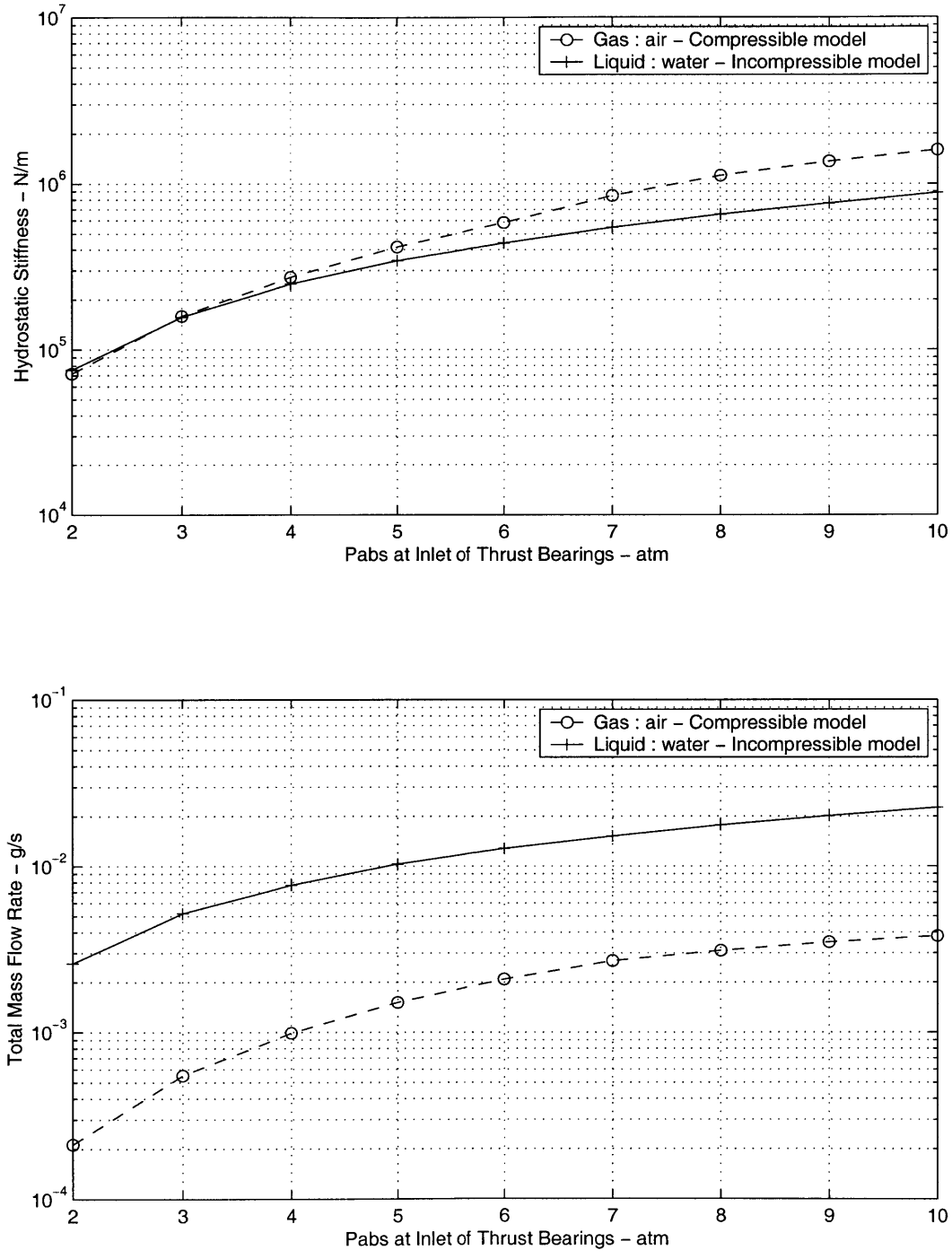

Figure 2-2: Hydrostatic thrust bearings characteristics for a fixed centered rotor for water and air

following operating range for the thrust bearings :

$$\begin{cases} P_{forward} \in [90psi, 95psi] \\ P_{aft} \in [50psi, 60psi] \end{cases}$$

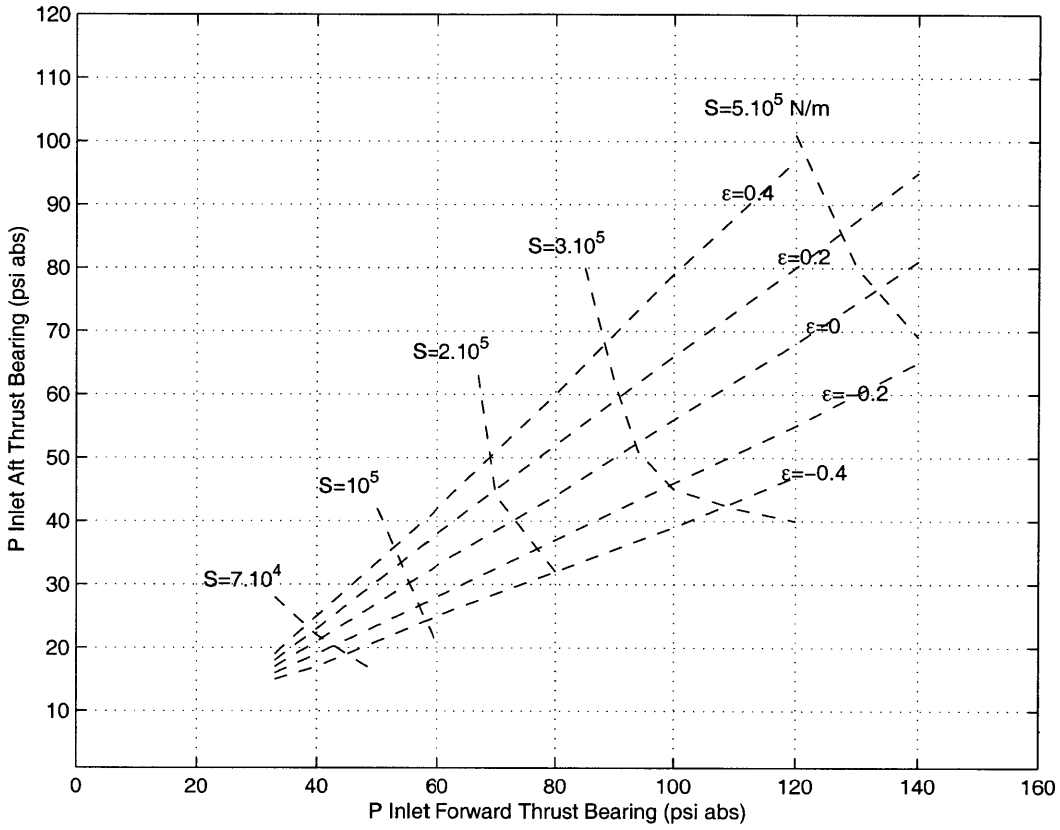

Figure 2-3: Stiffness S and eccentricity ε for a rotor in equilibrium with hydrostatic water thrust bearings (pressures forward and aft are different because the thrust bearing design is not symmetric)

Stability analysis

Finally, a stability analysis of these liquid thrust bearings was performed. When the pressure of one thrust bearing is modified, the rotor moves to a different equilibrium position. In other words, the system has to be able to present a net load to oppose the net force due to this pressure change. This must be achieved with a small variation of axial eccentricity to maintain the axial position in the safe range.

Figure 2-4 shows the predicted equilibrium eccentricity versus the pressure of one thrust bearing, while the pressure at the inlet of the other thrust bearing is constant. As can be seen from the flat shape of the curves, a moderate change in pressure results in a small change of eccentricity to maintain stability. Starting from an equilibrium position where $P_{atb} = 4atm \simeq 60psi$ and $P_{ftb} = 6atm \simeq 90psi$, a change of 0.5atm in the aft or forward thrust bearing pressure is overcome by a variation in eccentricity of 0.10 to 0.135. This allows safe operation for the rotor, considering the safe eccentricity range is assumed to be [-0.4 to 0.4].

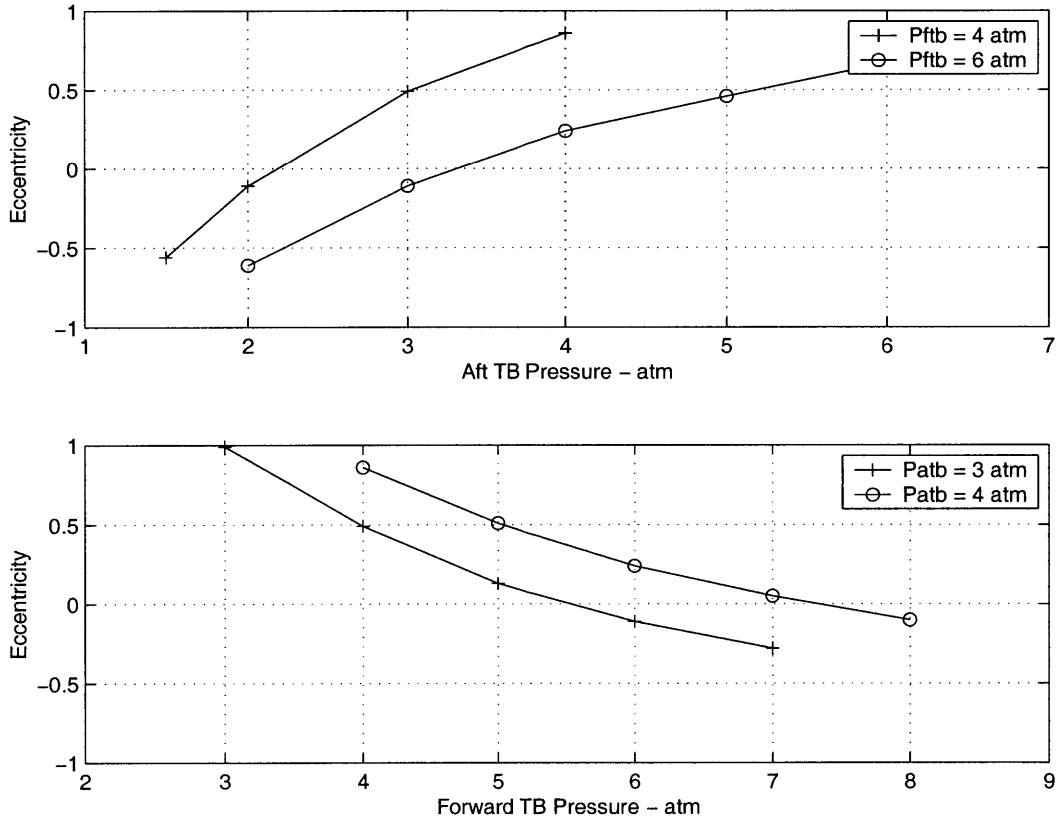

Figure 2-4: Eccentricity for rotor equilibrium with hydrostatic water thrust bearings

2.3 Journal Bearings

2.3.1 Introduction

This chapter deals with plain cylindrical journal bearings, where the bearing surfaces are parallel to the axis of rotation. Journal bearings are used to support shafts by carrying radial loads with minimum power loss and minimum wear. The journal bearing consists in a lubricant film trapped between a plain cylindrical sleeve (the bearing or stator) and the rotating shaft (the journal or rotor), as presented in Figure 2-5. The journal spins at an angular velocity ω inside the bearing.

The shaft does not normally run concentric with the bearing. The displacement of the journal center relative to the bearing center is the eccentricity e. The average gap between the journal and the bearing is the clearance c. The eccentricity ratio ϵ is the ratio of the eccentricity to the clearance c. The attitude angle ϕ is the angle between the line of centers that joins the bearing center and the journal center, and the load applied to the journal.

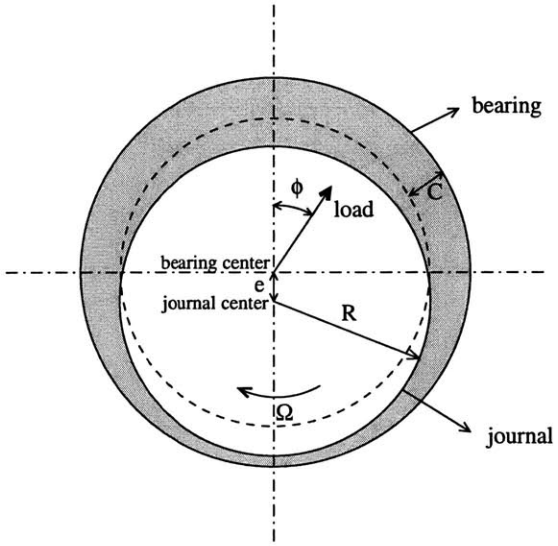

Figure 2-5: Journal bearing geometry and nomenclature

Liquid journal bearings, both hydrostatic and hydrodynamic, have been investigated. The geometry considered is that of the micro-bearing rig, developed for gas bearings experiments. The journal bearing of this device falls outside of the classic design space because of the large gap-to-radius ratio c/R, the small length-to-diameter ratio, the high Reynolds number, and the large surface area compared to the mass of the rotor [4].

2.3.2 Hydrostatic Journal Bearings

Hydrostatic bearings are externally pressurized and should be distinguished from hydrodynamic bearings, which are self-acting. In a hydrostatic bearing the surfaces are separated by a film of liquid forced between them under pressure. The pressure drop across the bearing supports the load. The pressure is derived from an external source. Because the pressurized film is not produced by the relative motion of the bearing surfaces, a complete film is present whenever the bearing is pressurized, even at zero speed [36]. The load-carrying capacity is independent of bearing motion and lubricant viscosity [18].

In practice, this bearing should be described as 'hybrid'. Indeed, the applied force on the journal will be reacted by the combined effect of hydrodynamic and hydrostatic bearing film pressures as soon as the shaft is rotating.

The gap is pressurized from a plenum that sits below both the rotor and the stator. The fluid flows axially, forced by a pressure differential dp between the plenum and the inter-blade row region. Wong [42] and Orr [28] provide insight in the previous work on axial through-flows and hydrostatic stiffness modelling. Orr proposes one explanation for the experimentally observed compensation mechanism. In reducing the Navier-Stokes equations to the Reynolds equation, inertia is neglected, and pressure-driven flows are assumed to be fully developed. The inertial effect of the growth of side-walls boundary layers at the entrance of the journal bearing is advanced to explain radial stiffness [28]. The hydrostatic natural frequency given by this model is in good agreement with the literature. Comparison of this model to the Tang-Gross model was performed by Wong [42]; he found that they differ by 15% for an axial pressure differential of 5 psi.

An incompressible model was developed by Breuer to account for this 'entry length' effect (the entry length being the distance needed for the flow to become fully developed). Figure 2-6 gives the hydrostatic natural frequency resulting from the axial flow driven by the pressure difference dp. A discharge coefficient C_D is set to account for the resistance to the flow. It is generally accepted that a realistic value of this coefficient is between 0.4 and 0.7 for a sharp edge geometry [20].

The whirl ratio is defined as $R_{whirl} = \Omega/\Omega_n$ where Ω is the rotor rotation frequency

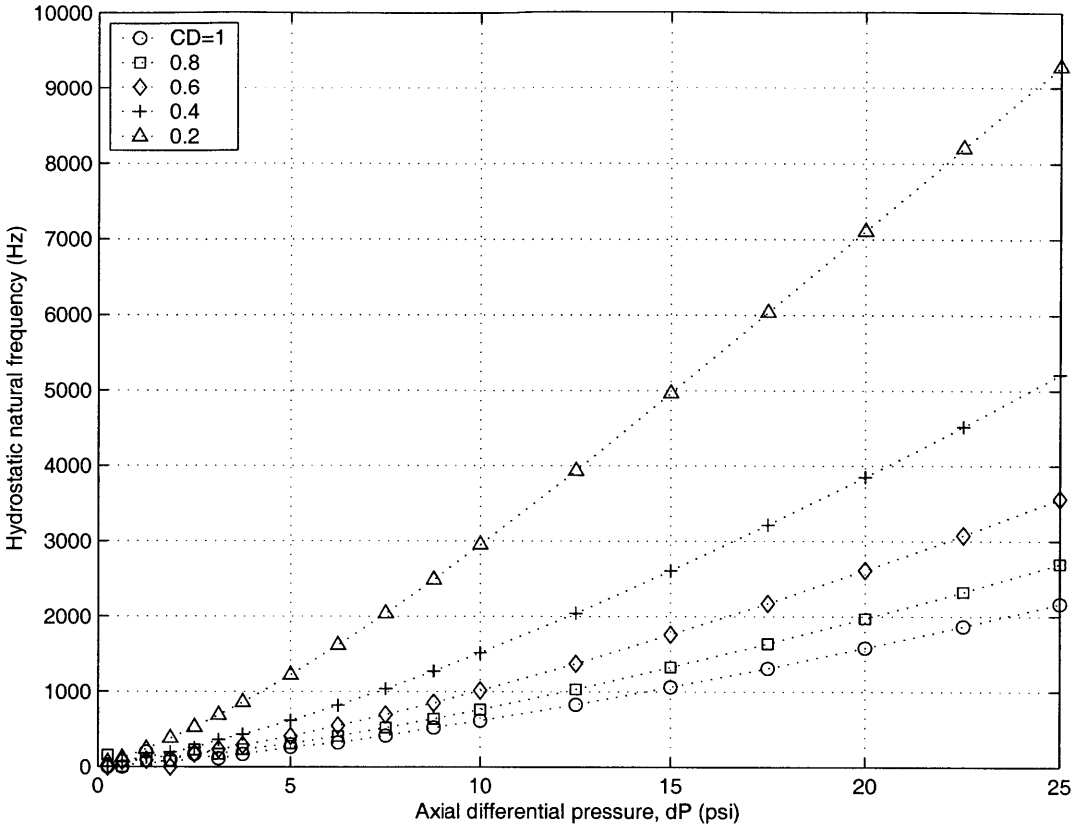

Figure 2-6: Hydrostatic incompressible natural frequency for the micro-bearing geometry as calculated with the Tang-Gross model implemented by Breuer.

and Ω_n is the whirl frequency. Subcritical operation refers to a whirl ratio smaller than 1, supercritical operation refers to a whirl ratio greater than 1. Larson and Richardson [35] state that stable operation is possible up to a whirl ratio of 5 to 6 for gas journal bearings. Wong [42] measured whirl ratios of 10 in high-speed micro-bearing operation.

Recent calculations performed by Dr Yifang Gong [16] suggest that the hydrostatic journal bearing mechanism comes from an inherent restrictor effect at the inlet to the journal bearing rather than from a boundary layer development mechanism as previously thought. This being the case, the stiffness developed will strongly depend on the geometry of the journal bearing at the entrance. High stiffness requires that the walls have sharp corners at the entrance. This effect is currently investigated.

2.3.3 Hydrodynamic Journal Bearings

A hydrodynamic journal bearing relies on shaft motion to generate the load-supporting pressures in the lubricant film. This bearing is said to be 'self-acting' because the hydrodynamic pressures which separate the two bearing surfaces are generated as a consequence of the movement of the bearing surfaces. The stiffness is derived from a moving surface acting as a viscous pump, but a non-zero eccentricity is required for stability. The surface of the journal drags liquid by means of viscous forces into the converging gap region between the two bearing surfaces. The result of the liquid being dragged into a more confined region is to create a back pressure. The squeeze mechanism of pressure generation provides a cushioning effect when the bearing surfaces approach each other.

Traditional approach

Pressure distribution in the film is modelled by Reynolds' equation which, with the shear stress at the journal surface, permits us to obtain the contact forces on the journal.

The assumption underlying the derivation of the Reynolds equation from the Navier-Stokes equations is violated in principle in the micro-bearing case, since the high Reynolds number results in non-negligible inertia effects in the bearing gap. Full Navier-Stokes computation results were compared to Reynolds lubrication solutions. The results showed that over the interesting range of bearing numbers, the Reynolds equation solutions remain accurate when compared to Navier-Stokes calculations [12].

The analytical solution of the Reynolds equation for the plain cylindrical journal bearing is known as the *full Sommerfeld solution* [18]. The pressure distribution is given by the following equation, in a non-dimensional form.

$$P = \frac{p - p_0}{\mu\omega}\left(\frac{c}{r}\right)^2 = \frac{6\epsilon \sin\phi.(2 + \epsilon\cos\phi)}{(2+\epsilon^2).(1+\epsilon\cos\phi)^2} \tag{2.2}$$

In Equation 2.2, p is the local absolute pressure, p_0 is the supply fluid pressure, called ambient pressure, and ϕ describes the running angular position in the bearing.

For an incompressible fluid, the full Sommerfeld solution is inherently unstable since the bearing has only cross-stiffness.

The Sommerfeld solution shows that the pressures in the divergent film are all lower than ambient pressure. Whenever the pressure falls below the saturation pressure, cavitation occurs. In traditional bearings, the saturation pressure is similar to the ambient pressure surrounding the bearing, then the gas liberation maintains the pressure in the divergent clearance space at close to the ambient level [18]. This approach is known as the *Half-Sommerfeld solution.* The analysis is restricted to the convergent film. Subambient pressures predicted by the analysis should be ignored. The pressure distribution is then given by

$$P = \begin{cases} \frac{p-p_0}{\mu\omega}\left(\frac{c}{r}\right)^2 = \frac{6\epsilon \sin\phi.(2+\epsilon\cos\phi)}{(2+\epsilon^2).(1+\epsilon\cos\phi)^2} & \text{if } 0 < \phi < \pi \\ 0 & \text{if } \pi < \phi < 2\pi \end{cases}$$

The pressure distributions for both Sommerfeld solutions at different values of the eccentricity ratio are presented in Figure 2-7.

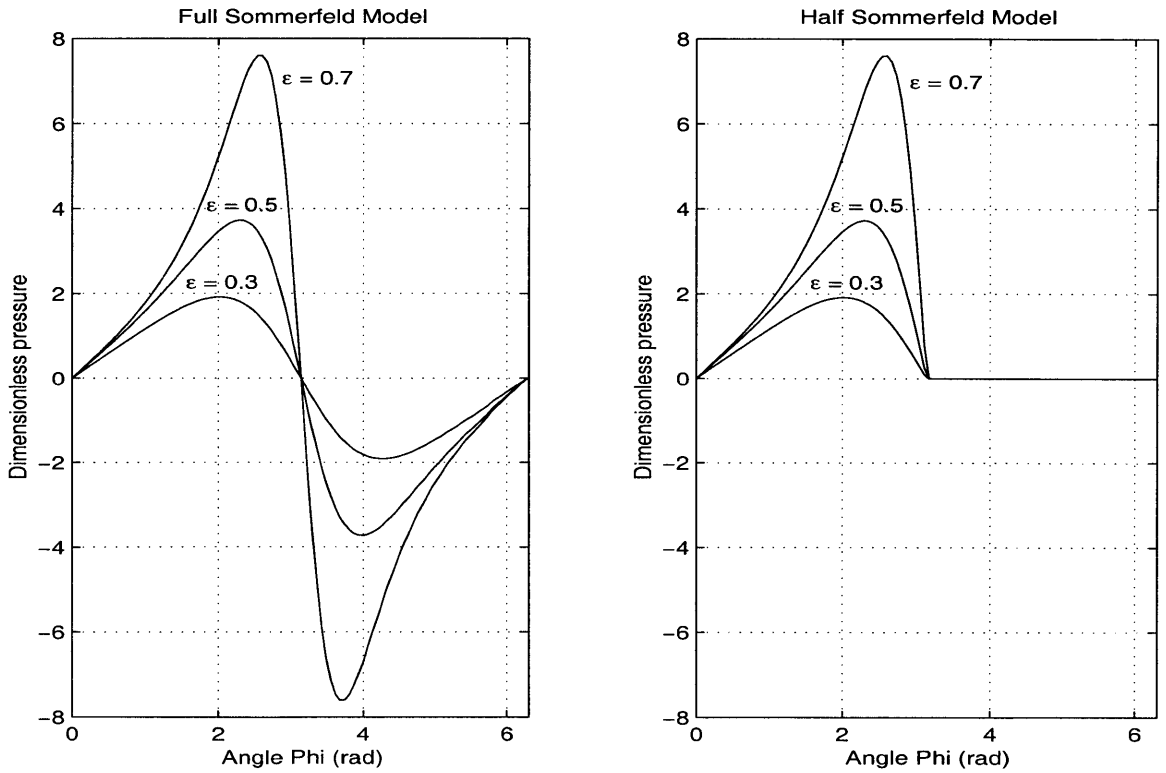

Figure 2-7: Pressure distribution from the Full and Half Sommerfeld solutions

Stiffness and damping coefficients can be obtained analytically, and then a stability analysis can be conducted.

New approach

Stability analysis were conducted, considering the Half Sommerfeld solution. The simple form of the pressure distribution allows an analytical calculation of the stiffness and damping coefficients, performed in [18]. The governing equation of the system can be reduced to a first-order differential equation, and thus solved by eigenvalues analysis.

This approach is valid as long as it is valid to consider that half the fluid region is cavitating. This assumption is usually valid since the ambient pressure in most bearings is similar to the saturation pressure of the fluid [18]. In a pump for the micro-rocket engine, it is possible that the journal bearing is supplied with high-pressure liquid. In this case, the previous assumption is not valid since the ambient pressure is much larger than the vaporization pressure.

A new stability model is proposed, where the cavitating region is more accurately modelled, if it exists. For each value of the bearing number Λ (which is a non-dimensional form of the speed), an iterative scheme on the eccentricity is run. At each step, the pressure distribution is computed. The vaporization pressure is neglected compared to the ambient pressure, then its non-dimensional form is a function of the speed (or of the bearing number) and the ambient pressure:

$$P_{sat} = \frac{-p_0}{\mu\omega}\left(\frac{c}{r}\right)^2 \tag{2.3}$$

If $P_{sat} > P_{min}$, there is no cavitating region. The exact solution is the Full Sommerfeld solution, and the bearing is unstable.

If there is a cavitating region (necessary for stability), its boundaries ϕ_1 and ϕ_2 are calculated. They verify the equation $P(\phi_1) = P(\phi_2) = P_{sat}$, and then are obviously function of ϵ. The new pressure distribution is then

$$P = \begin{cases} \frac{p-p_0}{\mu\omega}\left(\frac{c}{r}\right)^2 = \frac{6\epsilon \sin\phi.(2+\epsilon\cos\phi)}{(2+\epsilon^2).(1+\epsilon\cos\phi)^2} & \text{if } 0 < \phi < \phi_1 \text{ and } \phi_1 < \phi < 2\pi \\ P_{sat} & \text{if } \phi_1 < \phi < \phi_2 \end{cases}$$

The resultant load is computed. Following the notation adopted in [18] and detailed in the nomenclature, the resultant load is $w'_r = \sqrt{{w'_x}^2 + {w'_z}^2}$ where

$$w'_x = \int_0^{2\pi} pr\sin(\pi - \phi)\, d\phi \tag{2.4}$$

$$w'_z = \int_0^{2\pi} pr\cos(\pi - \phi)\, d\phi \tag{2.5}$$

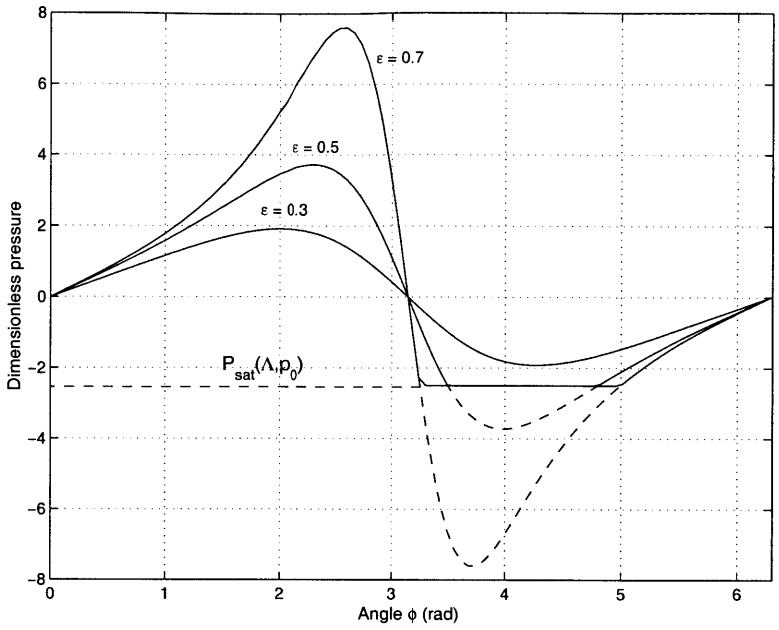

Figure 2-8: Pressure distribution from the new hydrodynamic model

The Sommerfeld number W_r and the attitude angle Φ are calculated. Damping and stiffness coefficients can then be obtained, and a eigenvalue analysis is performed to determine the stability of the system. This analysis is similar to the one conducted by Savoulides [37] and is not detailed hereafter.

Results

In this new hydrodynamic stability and load prediction model, the Sommerfeld number and the attitude angle are calculated considering the cavitation region that depends on the supply pressure P_0, the rotating speed ω, and the eccentricity ϵ.

The performance of the micro-bearing rig geometry was computed using this model, using water as fluid. The minimum eccentricity for stability is plotted in Figure 2-9 in the (Λ, ζ) plane, and in the (Λ, ϵ) plane, and for two values of the ambient pressure surrounding the bearing (average, or supply pressure). As can be seen, two stability boundaries exist, related to two different physical phenomenon. Hydrodynamic journal bearing stability requires stability for both these two phenomenon, the Full Sommerfeld instability, and the whirl instability.

At low rotational speeds (low bearing number Λ, below 0.1), stability is very difficult to achieve because a cavitation region only happens at eccentricities close to 1. The Full

Sommerfeld instability is the limiting factor; the model behaves very closely to the Full Sommerfeld model in terms of stiffness and damping.

As the speed increases ($0.1 < \Lambda < 1.2$ for P_a=30atm, 5 for P_a=1atm), the saturation pressure in its non-dimensional form increases, then the minimum eccentricity required for stability decreases, the bearing cavitates at lower eccentricities.

At higher speeds still ($\Lambda > 1.2$ for P_a=30atm, 5 for P_a=1atm), a different physical phenomenon becomes the limiting factor. A large cavitation region exists since P_{sat} is small, and the behavior is now closer to that of the Half Sommerfeld model. In this model, the minimum eccentricity required for stability increases with the bearing number. This is a characteristic of the Half Sommerfeld incompressible model [18]. A rotor whirl instability develops, and a larger eccentricity is necessary for a larger stiffness. Whirl is a self-excited vibration in a journal bearing which is caused by forces inherent in the hydrodynamic lubricant film [22].

Finally, the stability boundary asymptotes to a constant eccentricity ratio of 0.762, which is a characteristic of the half-Sommerfeld model.

As can be seen in Figure 2-9, the whirl instability boundary appears at lower speeds when the pressure is raised. For a given speed, a bearing surrounded by a higher pressure liquid needs a higher eccentricity to run stably. Indeed, higher ambient pressure is equivalent to a more massive journal from the mass parameter $\overline{M} = mP_a\psi^5/72L\mu^2$ (terms are defined in the nomenclature). When whirl is the limiting stability factor, higher pressure journal then requires more load, i.e. more eccentricity, to run stably.

For a better understanding of the cause of instability, an eigenelements analysis was performed. Figure 2-10 presents the locus of the eigenvalues of the matrix describing the motion of the bearing, in the complex plane, for several values of Λ. There are two couples of complex conjugate eigenvalues, corresponding to two physical modes of vibration. A detailed analysis of the eigenvectors shows that one mode is a *radial mode*, it is associated to vibrations in the radial direction, whereas the other mode is a *whirling mode*. As can be seen on Figure 2-10, the mode associated with rotor whirl produces a Hopf bifurcation at all speeds (the real part of the eigenvalue changes sign). The radial mode does not produce a Hopf bifurcation at any speed. This is the second major difference from gas journal bearings. Liquid hydrodynamic journal bearings do not exhibit radial instability, at any speed or eccentricity.

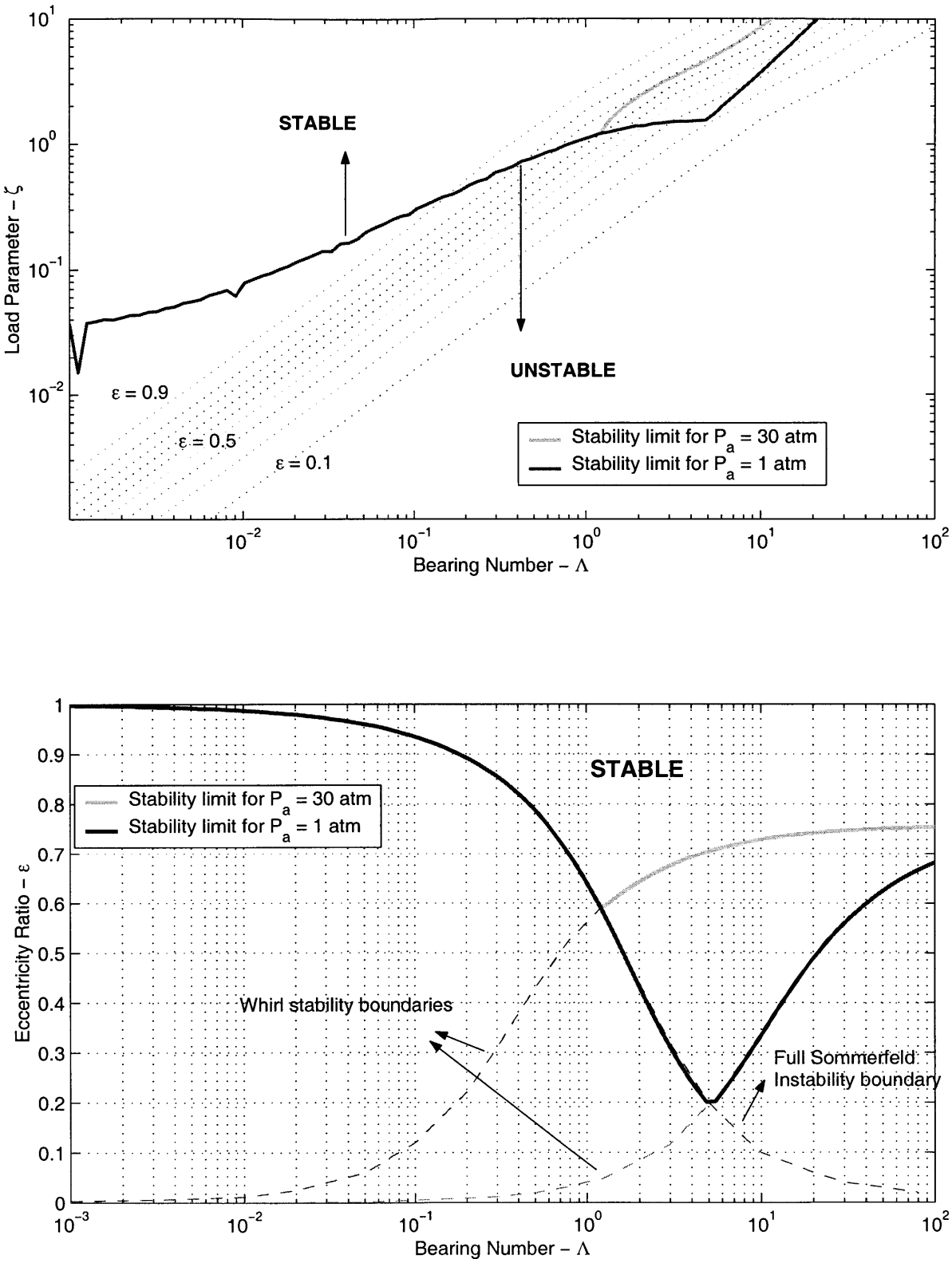

Figure 2-9: Minimum eccentricity for stability - Hydrodynamic water journal bearing

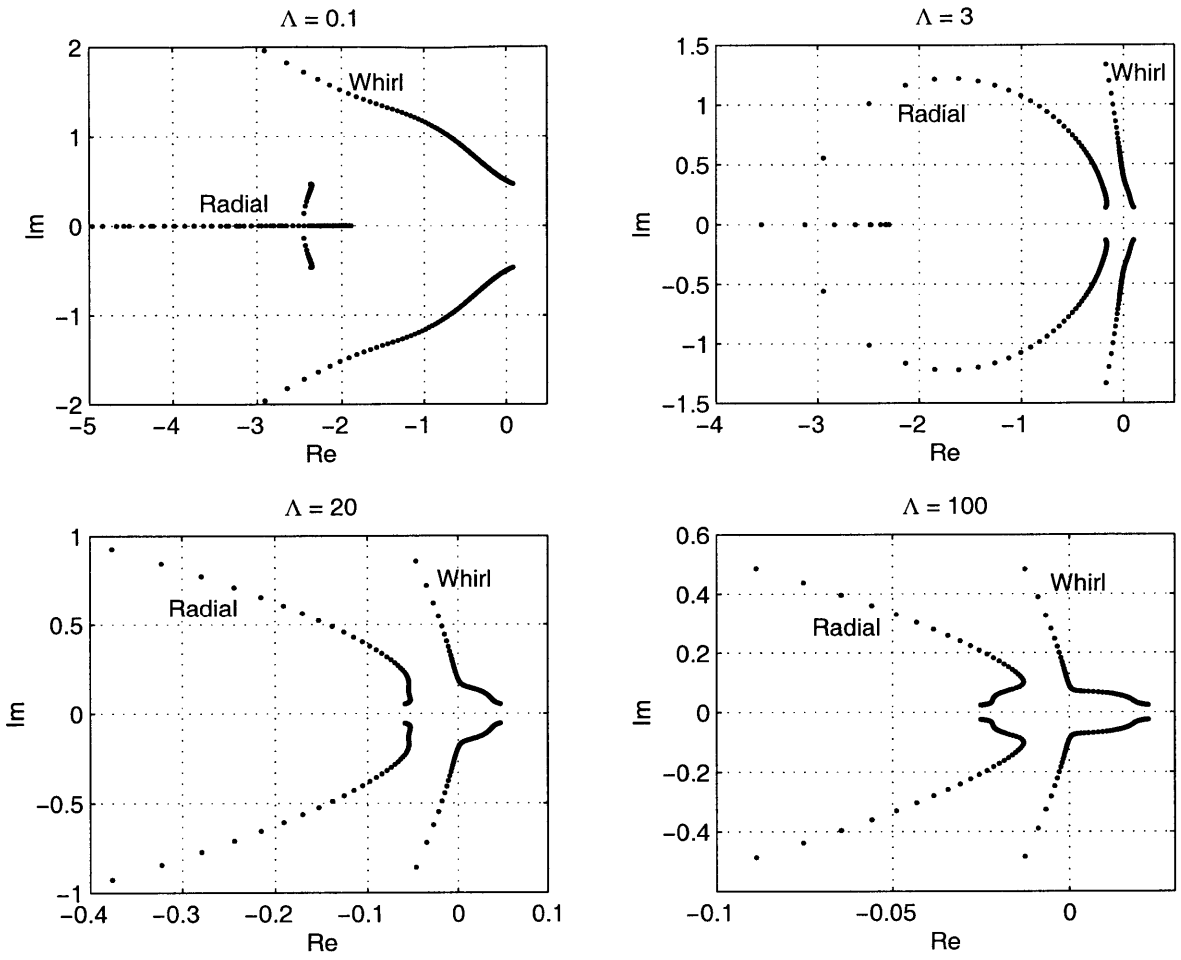

Figure 2-10: Eigenvalue root locus in complex plane of hydrodynamic water journal bearings

2.4 Analysis of operation of a liquid micro-bearing rig

As part of the micro-rocket engine program, liquid bearings have been investigated for application to a future micro-turbopump. For programmatic reasons, it was decided to demonstrate the feasibility of liquid bearings at micro-scale by running experiments on an existing device, the micro-bearing rig, designed for gas bearings.

In the following sections, the device geometry is briefly presented. Using the bearing analysis performed in the previous sections, feasibility of micro-bearing rig operation in a liquid environment is investigated. Bearings operating points are proposed, and axial balance is analyzed. A drag calculation is performed.

2.4.1 Micro-bearing rig geometry

The first micro bearing device was built and tested by Lin [25]. Fréchette improved the design and demonstrated high-speed operation [13]. Wong has recently implemented hydrodynamic thrust bearings [42]. The geometry presented here is the current design with pure hydrostatic bearings.

The micro-bearing rig device consists of a 4.2 mm diameter rotor enclosed in a fusion-bonded stack of five wafers. Fluidic ports lay on the top and bottom surfaces of the die for the fluidic interconnects for the hydrostatics bearings supply, the turbine supply, and pressure taps. A cross-section SEM and a schematic of the concept are shown in Figure 2-11.

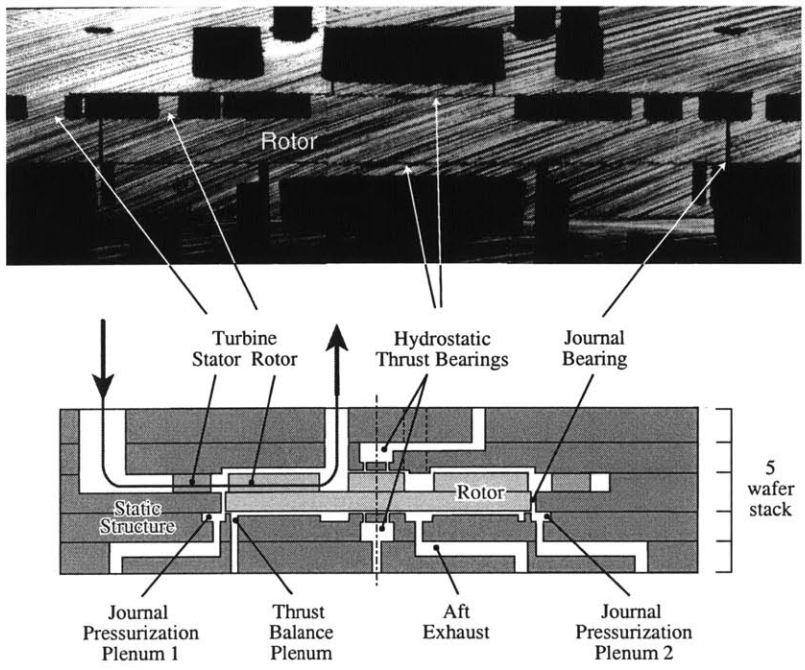

Figure 2-11: Micro-bearing rig cross-section and schematic (Fréchette [13])

The journal bearing clearance is 12 μm, and its length is 300 μm. The aft thrust bearing is stronger than the forward thrust bearing to accommodate the pressure forces on the front side of the rotor. It has 18 orifices, each 10 μm diameter and 100 μm long, located on a radius of 0.75 mm. The outer radius of the pad is 0.9 mm. The forward thrust bearing has 14 of the same orifices; their center is 0.55 mm from the centerline, and the pad radius is 0.7 mm. The design axial gap is 1.5 μm on each side.

The radial inflow turbine blades were designed by Jacobson using the MIT MISES code [9, 27]. The vanes and blades radius and angles are summirazed in Table 2.2.

Table 2.2: Micro-bearing rig turbine blades design parameters

NGV inlet radius	2.8 mm
NGV outlet radius	2.2 mm
NGV trailing edge angle	83.2 deg
Rotor leading edge radius	2 mm
Rotor trailing edge radius	1.3 mm
Rotor leading edge angle	83.2 deg
Rotor trailing edge angle	-57.1 deg

2.4.2 Bearings and force balance

Liquid micro-bearings are investigated for a future application in a liquid pump. Preliminary analysis show that a rotating speed of 750,000 rpm is desired. This speed is taken as the design speed of the liquid micro-bearing.

As stated in Section 2.2.3, high-speed operation requires an axial stiffness from the thrust bearings of $3 \times 10^5 N/m$, which is achieved with a pressure of 6 atm in the forward thrust bearing, and a pressure of 4 atm in the aft thrust bearing.

We mentioned in Section 2.3.2 that with gas, whirl ratios on the order of 10 have been demonstrated at micro-scale. Assuming this result can be obtained in liquid, a hydrostatic natural frequency of 1,250 Hz is necessary to achieve stability at a speed of 750,000 rpm. From Figure 2-6, an assumed discharge coefficient of 0.6 yields a necessary axial pressure differential of approximately 12 psi. These results are summarized in Table 2.4.2.

Table 2.3: Hydrostatic liquid bearings operating point

Design rotating speed	750,000 rpm
Forward thrust bearing pressure	6 atm
Aft thrust bearing pressure	4 atm
Journal bearing axial dp	12 psi

The axial forces on the rotor have three different origins[2]; they are shown in Figure 2-12:

- net axial pressure force from the thrust bearings
- viscous shear stress form the axial flow in the journal bearings
- pressure force through the turbine blades

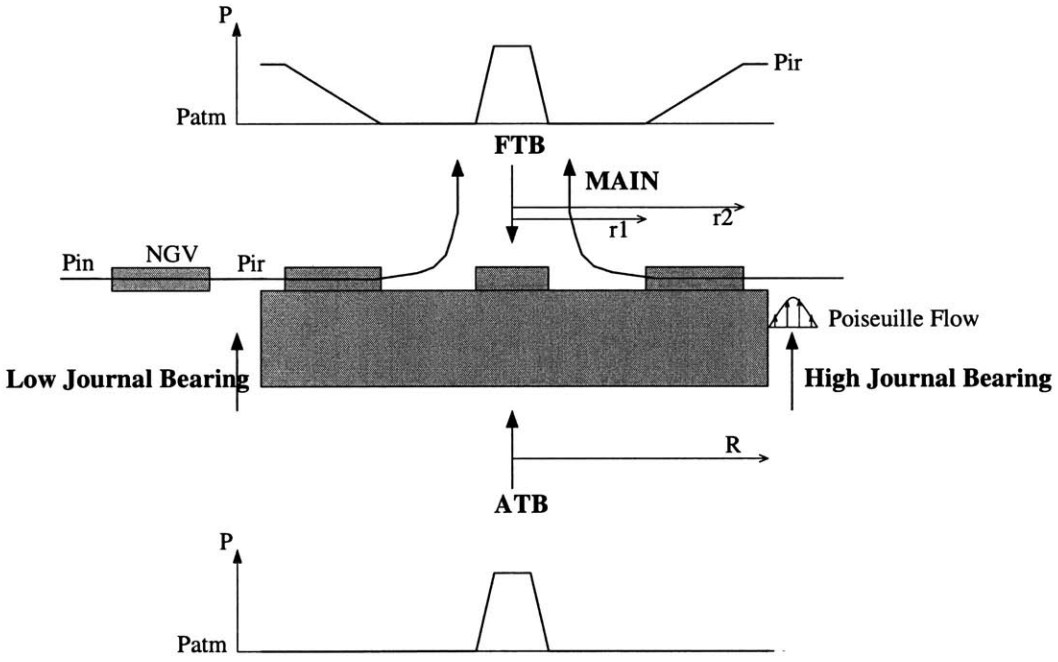

Figure 2-12: Schematic of axial and viscous forces acting on the rotor

For the thrust bearing operating point described above, the net axial force obtained from the thrust bearings varies with the axial eccentricity. Figure 2-13 shows the results of the computation of this net axial force.

The viscous shear stress is proportional to the radial pressure gradient. The rotor radius is R, and the running radius in the journal bearing gap is r. Assuming a Poiseuille flow in the journal bearing, the axial component of the velocity is

$$v(r) = \alpha\Big(r - R - c/2\Big)^2 \tag{2.6}$$

[2]The micro-bearing device also includes a Motor Outer Plenum that is externally pressurized to give axial load to the rotor from the aft side. It is usually not used during experiments, and is not considered in this force balance analysis.

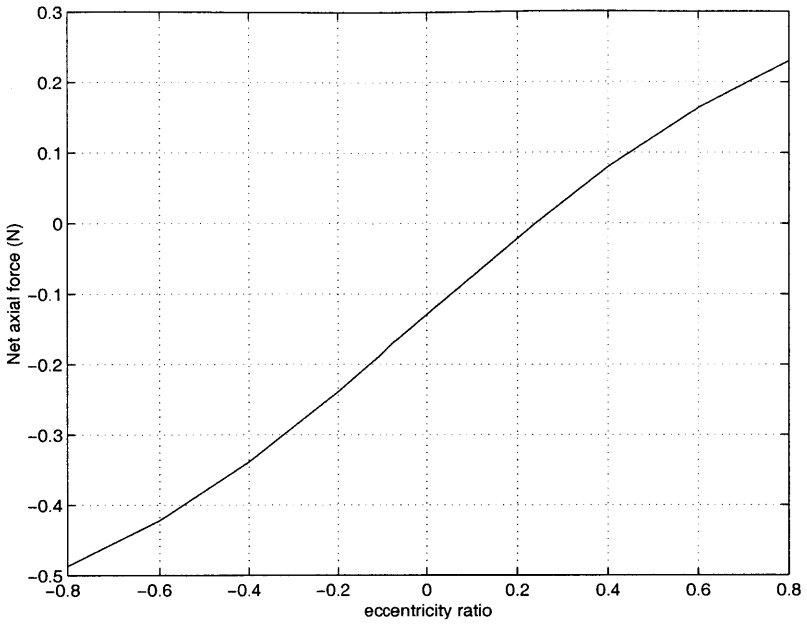

Figure 2-13: Net axial force from water thrust bearings

where α can be obtained by integration since we know the mass flow (given by the code from which the natural frequency is derived). Indeed,

$$\dot{m} = \rho 2\pi \int_R^{R+c} v(r) r dr \tag{2.7}$$

The vertical component of the shear stress is uniform,

$$\sigma_z = \mu \frac{\partial U}{\partial r}(R) = \mu \alpha c \tag{2.8}$$

Then, the axial force associated to this viscous shear in the journal bearing gap is

$$F_{JB} = 2\pi R L \sigma \tag{2.9}$$

For an axial pressure differential $dp = 12psi$, the mass flow is 1 mg/s. This gives an axial viscous force of $2.22 \times 10^{-5} N$. This force is negligible compared to the net axial pressure force due to the thrust bearings.

Finally, the force due to the pressure distribution though the turbine blades is computed. The pressure at the entrance of the blades is the inter-row pressure P_{ir}, and the exit pressure is the atmospheric pressure P_{atm}. Only the pressure differential with P_{atm} is considered,

since the back side of the rotor is vented to atmosphere. Thus, we neglect the integration of P_{atm}, which is zero to first order[3].

A linear variation of the pressure though the turbine blades is assumed. By pressure integration, the pressure force on the front side of the rotor is, with the notation presented on Figure 2-12 :

$$F = (P_{ir} - P_{atm})\pi(R^2 - r_2^2) + 2\pi\frac{P_{ir} - P_{atm}}{r_2 - r_1}\left[\frac{r^3}{3} - r_1\frac{r^2}{2}\right]_{r_1}^{r_2} \tag{2.10}$$

Combining these force calculations, we can compute the axial eccentricity necessary for axial equilibrium versus the inter-row pressure. Extrapolation from gas experiments yields the estimate that $P_{ir} - P_{atm} = 8psi$ should be enough to drive the rotor at the desired design speed. The results are presented in Figure 2-14. As can be seen, over the range of inter-row pressure (and then, over the range of speed), the axial eccentricity moves from 0.25 to -0.3 for the given thrust bearings pressures (6 atm and 4 atm). This suggests that axial balance should not be an issue in operating the liquid micro-bearing device.

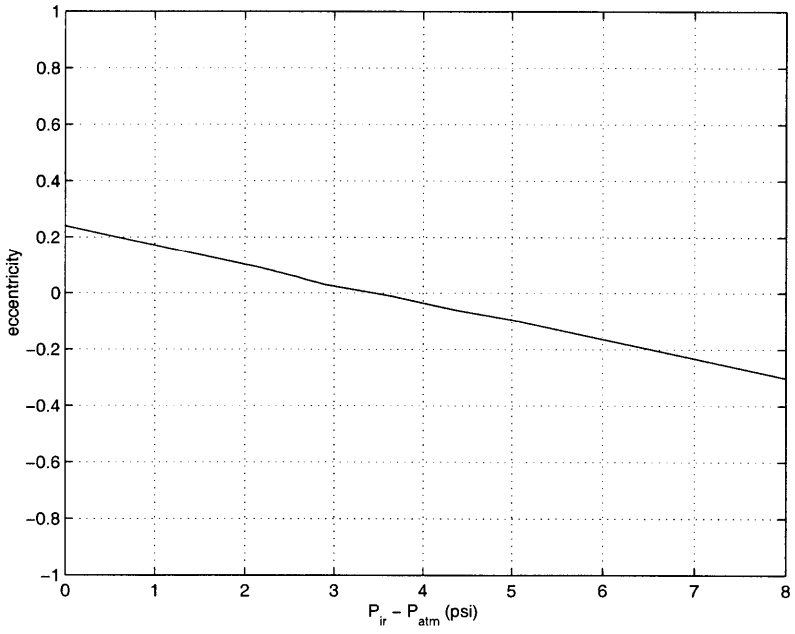

Figure 2-14: Eccentricity needed for axial equilibrium vs inter-row pressure, P_{ir}

[3]Indeed, the thrust bearing pads on both sides are not the same size. The atmospheric pressure then applies to a different area on each side.

2.4.3 Drag

The combination of small gaps, high rotating speeds, and larger viscosity than gas results in highly sheared flows, and large viscous dissipation. In the micro-bearing rig, drag arises from the tangential flow in the journal bearing gap, in the thrust bearing gaps, and in the aft plenum. In these areas, the flow is dominated by viscous effects, and can be represented as Couette flow.

In the journal bearing, assuming the rotor is perfectly centered, the tangential component of the shear stress is

$$\sigma_{r,\theta} = \mu\Big[r\frac{\partial}{\partial r}\Big(\frac{V_\theta}{r}\Big) + \frac{1}{r}\frac{\partial U_r}{\partial \theta}\Big] = \mu\frac{\Omega R}{c} \tag{2.11}$$

The viscous torque is obtained by integration of the product of the shear stress along the radius over the journal surface,

$$T_{visc,jb} = \iint \sigma_{r,\theta}\, r\, d\theta\, dz = 2\pi\mu L\omega R^3/c \tag{2.12}$$

This leads to the dissipated power in the journal bearing gap,

$$P_{visc,jb} = 2\pi\mu L\omega^2 R^3/c \tag{2.13}$$

The same method allows computation of the components $\sigma_{z,\theta}$ and integration of them over the rotor back side and on the thrust bearing pads. This yields

$$P_{visc,tb} = \frac{\mu\pi\omega^2}{2g}(r_f^4 + r_a^4) \tag{2.14}$$

$$P_{visc,back} = \frac{\mu\pi\omega^2}{2g_{mop}}(R^4 - r_a^4) \tag{2.15}$$

The total power dissipated $P_{visc} = P_{visc,jb} + P_{visc,tb} + P_{visc,back}$ is calculated over the speed range (up to 750,000 rpm) as shown on Figure 2-15. As can be seen, the power dissipated is relatively large with water, greater than 25 Watts at design speed. This is 47 times the value for air at this same speed. For steady-state operation, the power delivered by the turbine has to match the viscous power dissipation.

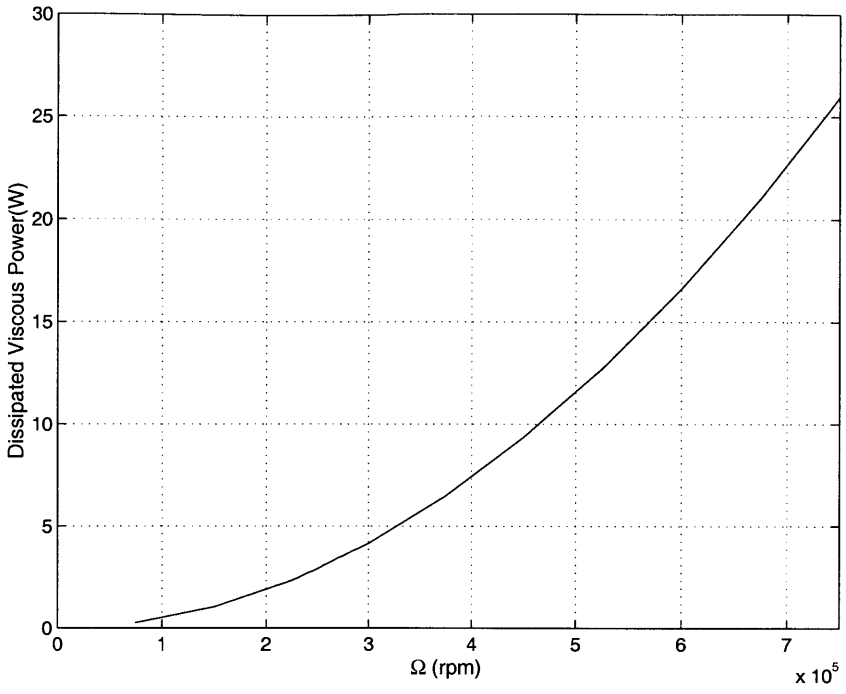

Figure 2-15: Dissipated viscous power for the water operation of the micro-bearing rig

2.4.4 Turbine power

The torque on the turbine blades equals the variation of absolute angular momentum through the blades. The power is the torque multiplied by the rotating speed. Intensive computational fluid dynamics could be performed to obtain the turbine power, but we can obtain an approximate value from the velocity triangles. For a given mass flow, the radial velocity at each stage (guide vanes leading edge and trailing edge, rotor blades leading edge and trailing edge) was deduced from the geometry since the fluid is incompressible. We assumed that the flow angle equals the blade angle, then the relative tangential component of the velocity was calculated from the radial component and the flow angle. Finally, the absolute velocity was calculated by simple vectorial addition. The velocity triangles for the water operation of the micro-bearing rig at design speed are shown in Figure 2-16.

The turbine of the micro-bearing rig was not designed to produce positive power. At equilibrium, the turbine power matches the viscous drag. For given values of the speed and flow rate, the torque and turbine power were calculated from the variation of angular momentum. For each value of the speed, the drag was obtained from 2.4.3, and iterations

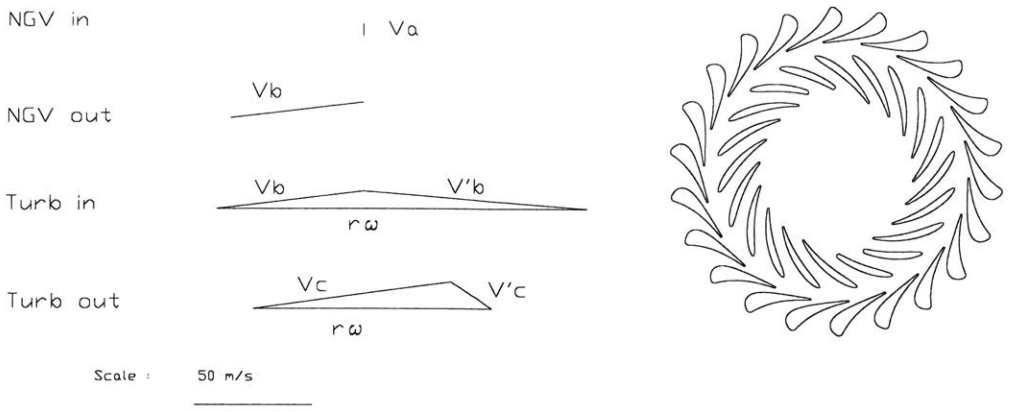

Figure 2-16: Micro-bearing turbine profile and velocity triangles for water operation at design speed $\omega = 750{,}000$ rpm. Velocities in the relative frame are primed.

on the flow rate were performed until the turbine power matches the dissipated power. The flow rate necessary for a given speed, and the corresponding turbine torque, are presented in Figure 2-17.

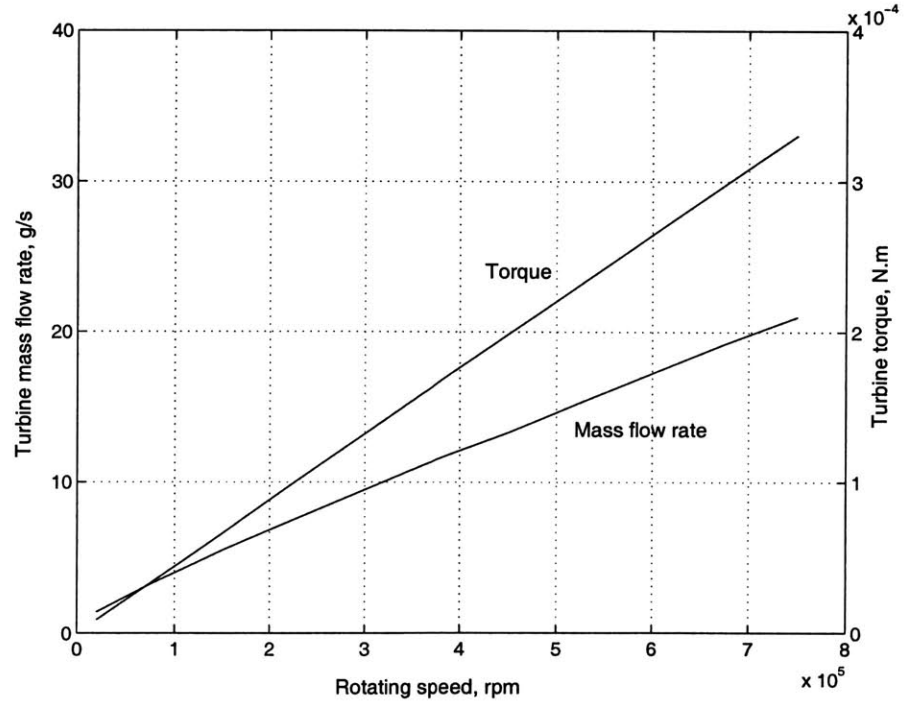

Figure 2-17: Necessary mass flow rate versus rotating speed and corresponding torque for water operation of the micro-bearing rig.

2.4.5 Liquid operation start-up

The non-conventional aspect of the velocity triangles, due to the large rotational speed and small mass flow, raises some concerns about the start-up of this device. Flow through the static rotor should create a torque in the correct direction, one large enough to overcome any forces that might prevent spinning. These forces could be associated with friction in the thrust or journal bearing, or stiction of the rotor.

The same calculation as in the previous section was performed, except that the rotating speed is zero. The torque equals the variation of angular momentum through the turbine blades. Results are presented in Figure 2-18. It was verified that the torque has the correct orientation to start the turbine.

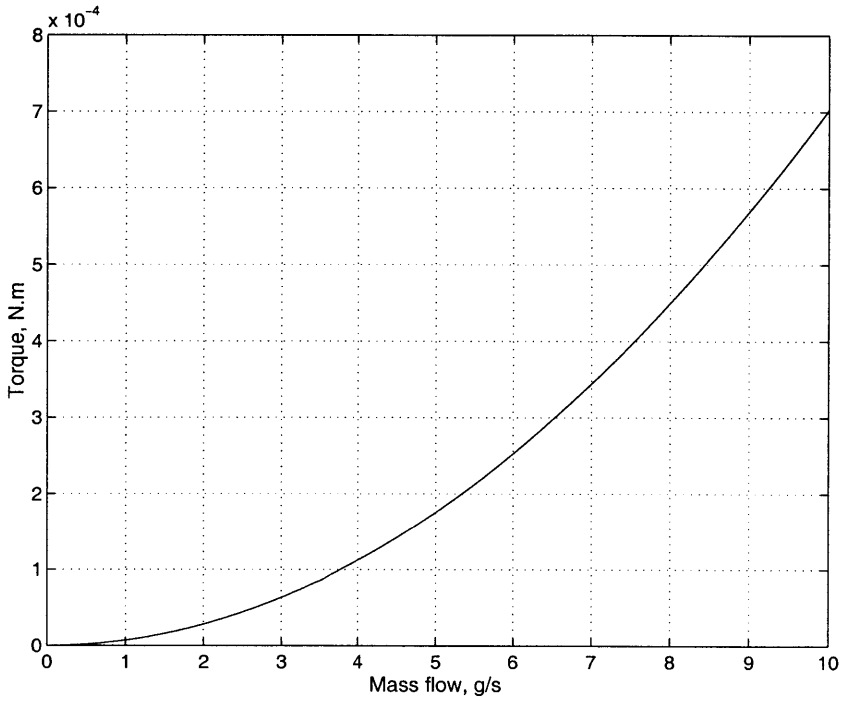

Figure 2-18: Turbine torque versus mass flow rate for a static rotor.

2.4.6 Comparison of the predicted performance of the micro-bearing rig geometry with water and gas

Liquid operation of the micro-bearing rig in a liquid environment was analyzed with the models developed and used in this Chapter. A comparison of the water and nitrogen (which is used for gas experiments) predicted operation of this device was performed. Performance

of the turbine, of the thrust and journal bearings, and drag are compared. Data are presented in Table 2.4.

Table 2.4: Comparison of the predicted performance of the micro-bearing rig geometry with gas and liquid

	Gas : N_2	**Liquid : water**
Thrust Bearings		
total flow at 50 psig	50.3 sccm = 1.0 mg/s	5.3 mg/s
total flow at 100 psig	116.4 sccm = 2.3 mg/s	10.4 mg/s
stiffness at 50 psig	4.4×10^5 N.m	2.8×10^5 N.m
stiffness at 100 psig	1.2×10^6 N.m	6.0×10^5 N.m
Journal Bearing (gap 12 microns)		
flow rate at dp=2 psi	305 sccm = 6 mg/s	98.1 mg/s
flow rate at dp=5 psi	808 sccm = 15.9 mg/s	245.3 mg/s
natural frequency at dp=2 psi	458 Hz	128 Hz
natural frequency at dp=5 psi	1113 Hz	388 Hz
Turbine Power		
flow conditions for power = 5W :		
mass flow rate	5750 sccm = 113 mg/s	10.2 g/s
turbine inlet pressure	27 psig	–
Dissipated Power		
drag at 20,000 rpm	4.3×10^{-4} W	0.02 W
drag at 500,000 rpm	0.25 W	11.5 W
drag at 1.4×10^6 rpm	1.93 W	90.5 W

The 1D model used to calculate the liquid turbine power only accounts for the water mass flow, and does not supply a mass flow/turbine inlet pressure relation. CFD calculations should be performed to obtain this relation.

2.4.7 Conclusion

This analysis suggests that operation of the existing micro-bearing rigs is feasible with water. The hydrostatic bearings have adequate stiffness, and the balance is acceptable. However,

viscous drag is very large. In future designs, parametric analysis must be performed on the bearings to maximize stiffness and at the same time reduce drag.

Chapter 3

Experimental Setup

This chapter describes the experimental setup and instrumentation for the liquid micro bearings device tests. The experimental setup includes a package that interfaces the micro-scale test device with the external environment. The apparatus is illustrated in Figure 3-1. It allows fluidic connections of the die to the liquid handling and instrumentation system, sensors, and a computerized data acquisition system. The packaging and the water handling and instrumentation system are derived from their equivalents in [13].

The micro-bearing device is presented in Section 2.4. It accommodates bearings that were designed for gas, but the whole system is tested with water.

3.1 Packaging

The test device requires packaging that realizes fluidic interconnections. The packaging brings pressurized water for the bearings and the turbine, and lines for the pressure taps. It must allow leak-free water connections, and optical speed measurement. The only functional difference with the gas packaging presented in [25] and [13] is that the exhaust is not to atmosphere, but connected to a dump tank. This prevents the same speed sensor configuration where an optical fiber is inserted in the die through the packaging exhaust. This issue is discussed in Section 3.3.

A brass/aluminum package was designed and built. It consists of top and bottom plates of brass that sandwich the die and accommodate fluidic interconnect flow paths, and an aluminum spacer plate that positions the die. The spacer plate is two mils thicker than the device, ensuring that the silicon die does not contact the top and bottom brass plates.

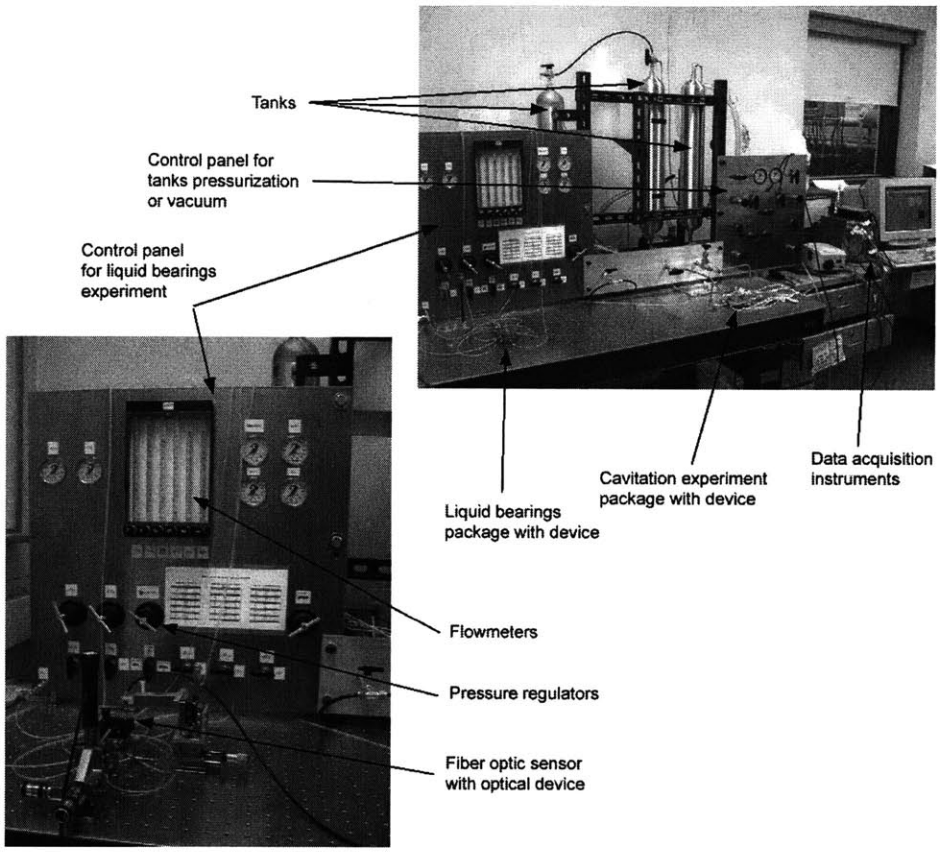

Figure 3-1: Photographs of the liquid bearing rig test set-up.

Instead, the die is supported by the rubber o-rings that seal the fluidic ports at the plate/die interface. The test device being the same as the one used in [13], the same interconnect design was used. Parker 2-002 and 2-004 o-rings are chosen for the interconnects, and the package is designed to create a 20% compression on the o-rings. A Parker 2-005 is chosen to seal the exhaust, and the groove is designed for a 10% compression. A higher compression of this center o-ring would result in a large deflecting force on the die, which could close the thrust bearing gap.

The flow channels are connected to the water handling system by quick couplers from Scanivalve (model QC063-TH) that are screwed in the top and bottom plates, 0.063" stainless steel bulged tubulations, and 0.063" plastic tubing. This system allows high pressure operation and flexible operation at the same time. The plastic tubing was changed to copper tubing after realizing that the plastic was the source of the die contamination. This issue is detailed in Appendix C.

A window is accommodated on the top surface of the top plate. It allows speed measure-

ment as described in 3.3, and observation of the rotor motion with a long-range microscope. This device is composed of a 10 mm diameter sapphire window from Edmund Scientific Company (model F43366), and is hold by an aluminum cover. A 2-008 o-ring is used to seal this window.

The CAD drawings of the packaging are presented in Appendix B. The packaging is illustrated in Figure 3-2.

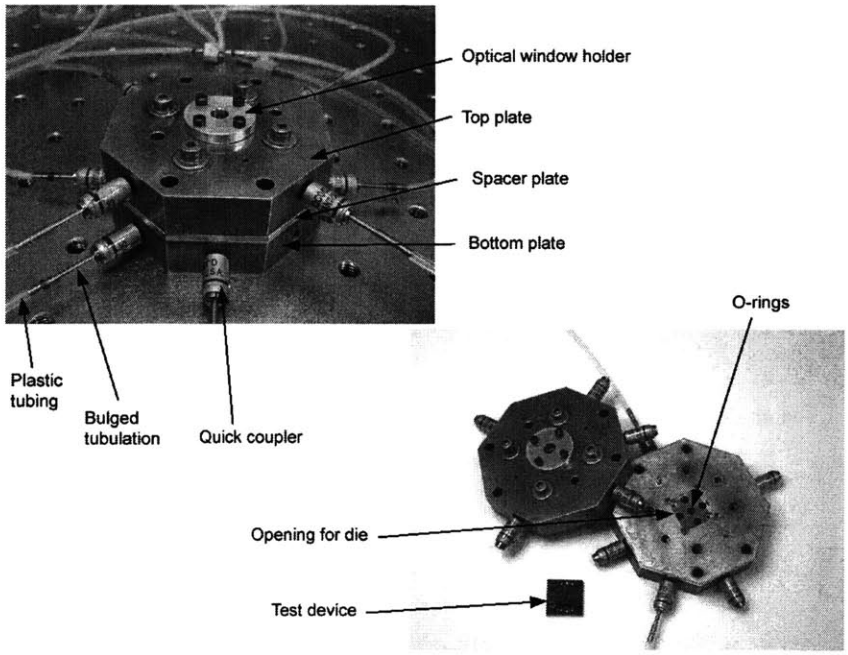

Figure 3-2: Photographs of the liquid bearing rig packaging.

3.2 Water handling and instrumentation system

The water handling and instrumentation system supplies water to the test device, gathers water out of it, measures pressures and mass flows into the device, and senses rotor speed.

The upstream part of the water handling system, which brings pressurized water from a supply tank, and collects water in a dump tank, was designed by Pennathur [31]. Figure 3-3 shows a schematic diagram of this part. As can be seen, an extra supply tank was added in order to be able to run the cavitation experiment and the liquid bearing experiment with distinct liquids. Deionized water filtered to 0.5 μm is used. Downstream of each tank, in-line filters from Swagelock retain the particles larger than 0.5 μm that might come from external contamination. 0.3 μm in-line filters from Cole Parmer are added downstream of

each line in the water handling system. A vacuum pump allows degasing of the water in the supply tanks, and evacuation of the lines and the experiment before filling them with water. The tanks are pressurized with bottled helium.

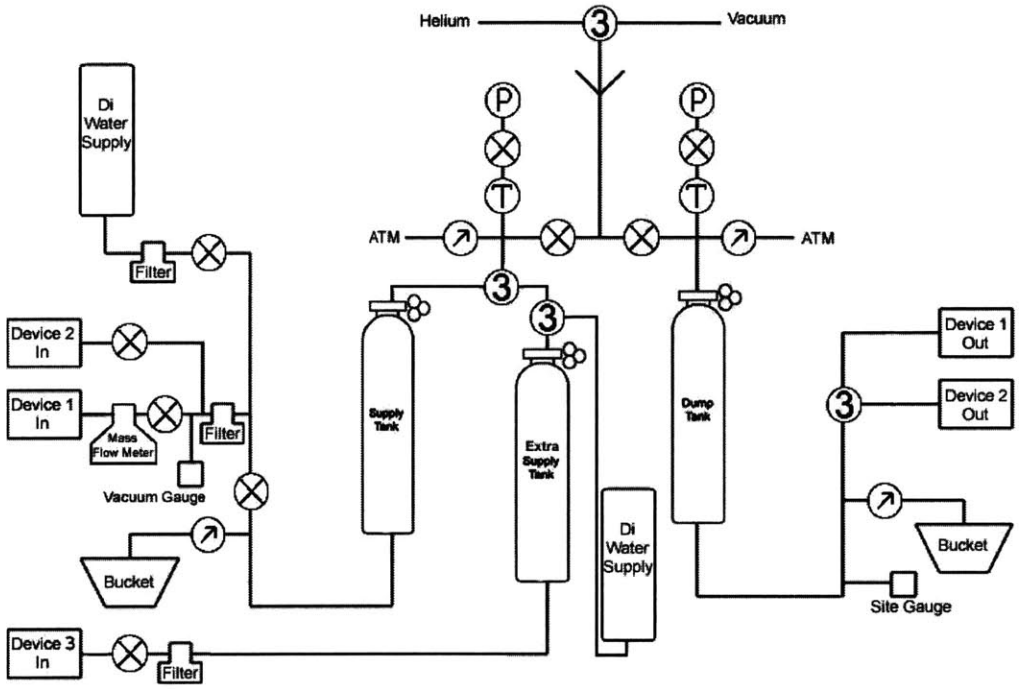

Figure 3-3: Upstream part of the water handling system - courtesy of Chris Rakowski

The downstream part of the water handling system is based on the gas handling rig designed by Lin and Fréchette for gas bearing experiments [25] and [13]. It provides:

- controlled pressures and mass flow measurement to six individual ports: main turbine inlet, forward and aft thrust bearings (FTB, ATB), high and low journal bearings pressurization plenum (high JB, low JB), motor outer plenum (MOP)
- measurement of the inter-row static pressure (IR)
- controlled pressure at the exhaust.

Figure 3-4 shows a schematic of the downstream part of the water handling and instrumentation system. It has two major branches. A primary branch supplies the thrust bearings and turbine main flow. Pressure is controlled in each port by a Norgren R43-210-

NGSA water pressure regulator. A secondary branch supplies water to the journal plenum for hydrostatic journal pressurization, to the motor outer plenum, and to the turbine inlet [1]. The journal, turbine and MOP flow are controlled with metering valves downstream of a common pressure regulator. This configuration proposed by Fréchette [13] allows simultaneous increase in journal bearing stiffness and MOP pressure with speed, following a predetermined protocol.

The pressure in each port is measured directly upstream of the packaging by a Omega pressure gage, and by a Kulite XT-190 pressure transducer. The mass flows are measured with variable area flowmeters from Cole Parmer. A multitube flowmeter system is chosen. A aluminum frame accommodates the six flowmeters, and six high-resolution valves. Each flowmeter is a 150-mm flowtube correlated for water. The fluid enters bottom of the flowtube and exits through the top. The upward pressure causes float to rise in flowtube. The range of the selected flowtubes is chosen from the model results [8].

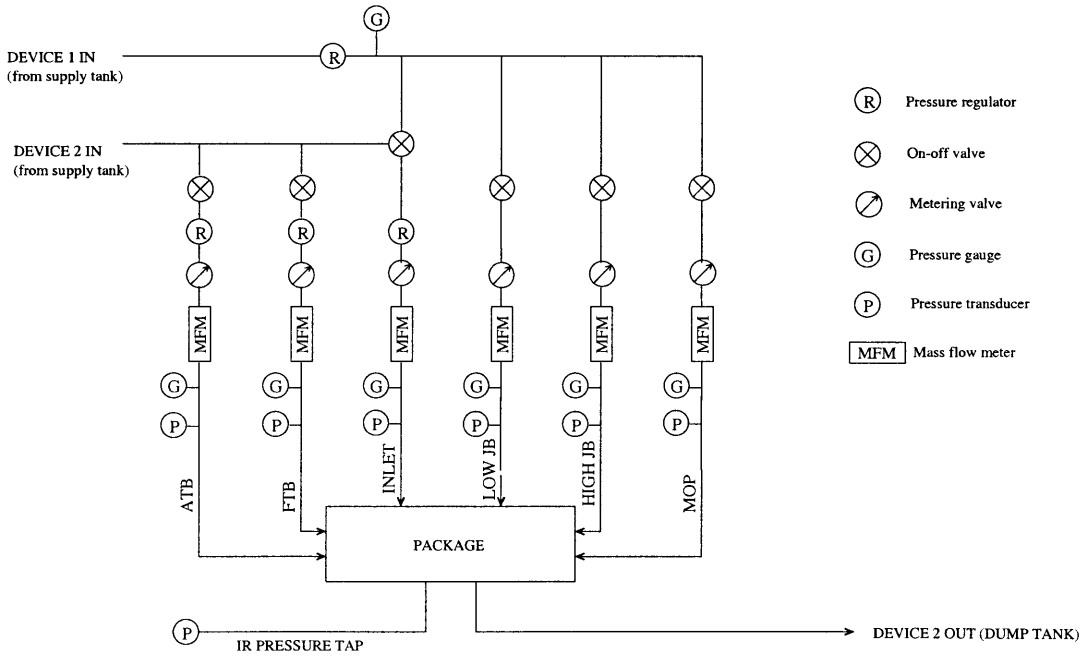

Figure 3-4: Downstream part of the water handling system

The rotational speed is measured with a Philtec D6-A1H2M1QTV high-frequency fiber optic sensor. It was originally put together by Lin [25] and Fréchette [13]. The sensor

[1]The turbine inlet can be connected to either line, depending if one chooses to couple it to the journal bearings and MOP or not

detects the passage of two 'speed bumps' that are features built on the silicon rotor, and located in the exhaust flow from the turbine. The speed sensor output is converted into a frequency in a spectrum analyzer. The specified bandwidth of 1 Mhz makes it useful for rotational speed up to 2.5 million RPM, with sufficient resolution to capture the passing of four speed bumps if this solution was implemented in a future device.

In the gas bearings experiments, the speed sensor intrudes into the die. The optic fiber is operated in the far field, close to its optical peak for maximum output and resolution **??**. For this reason, the probe tip is positioned approximately 150 μm from the top of the speed bumps. It is inserted through the packaging exhaust inside the die with a high-precision XYZ stage. The specified sensor range is 50 mils, or 1.27 mm. This was verified experimentally. When the probe is lifted 1.5 mm from its optimal position, the speed information is lost.

The liquid packaging has an exhaust connected to the water handling system. In the water experiment, contrarily to the gas experiment where the turbine exit is vented to atmosphere, the speed sensor can not be simply inserted into the die through the packaging exhaust. Different solutions have been proposed and investigated, they are presented in the following section. As can be seen on Figure 3-5, the solution adopted is a coupling of the optic fiber to an achromat lens to increase the standoff distance of the sensor. The lens is placed 37 mm above the die with a XYZ high-precision stage, and the optic fiber is positioned 13 mm above the lens with an independent stage.

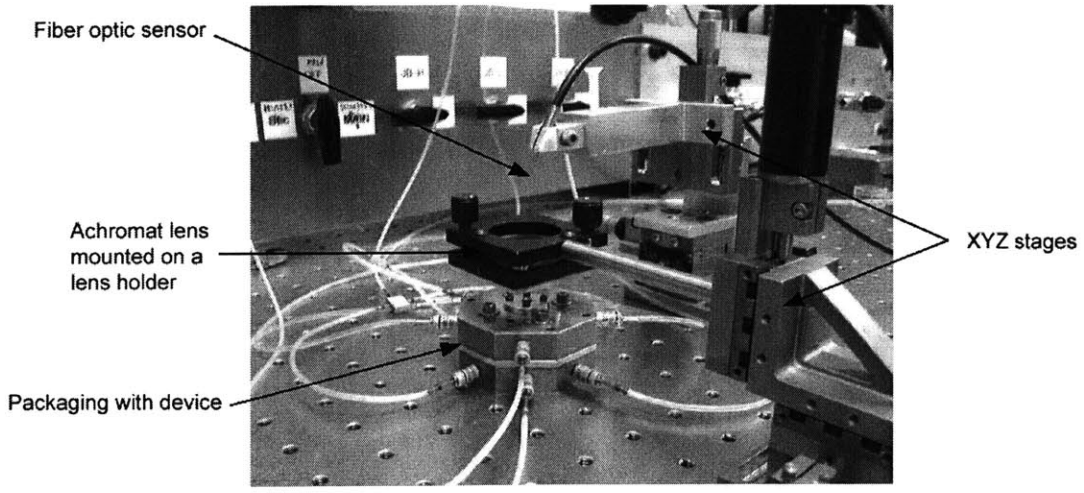

Figure 3-5: Photographs of the liquid bearing rig speed sensor set-up.

3.3 Validation of the speed sensor setup

3.3.1 Speed sensor configuration solutions

Since the water packaging does not allow direct access to the die exhaust, an innovative solution has to be proposed to use the fiber optic as a speed sensor. Two solutions are envisioned. They are shown in Figure 3-6. An intrusive solution was proposed by MTI Instruments [1]. The MTI-2000 Fotonic sensor probe has a special configuration with a high-pressure water casing. A Conax fitting with O-ring seal allows crossing the packaging. The drawback of this scheme is that a slight non-verticality of the probe makes it impossible to position the tip into the specified hole in the die. This hole is only 380 μm in diameter.

The second proposition is non-intrusive, with the optic fiber positioned outside of the packaging, in which a window is provided. Optic fibers do not present the required large standoff distance and small resolution at the same time. The D6 optic fiber is then coupled by a focusing lens system. This allows a spatial displacement of the optical peak. The range and the resolution of the fiber stay the same, but the standoff distance is increased.

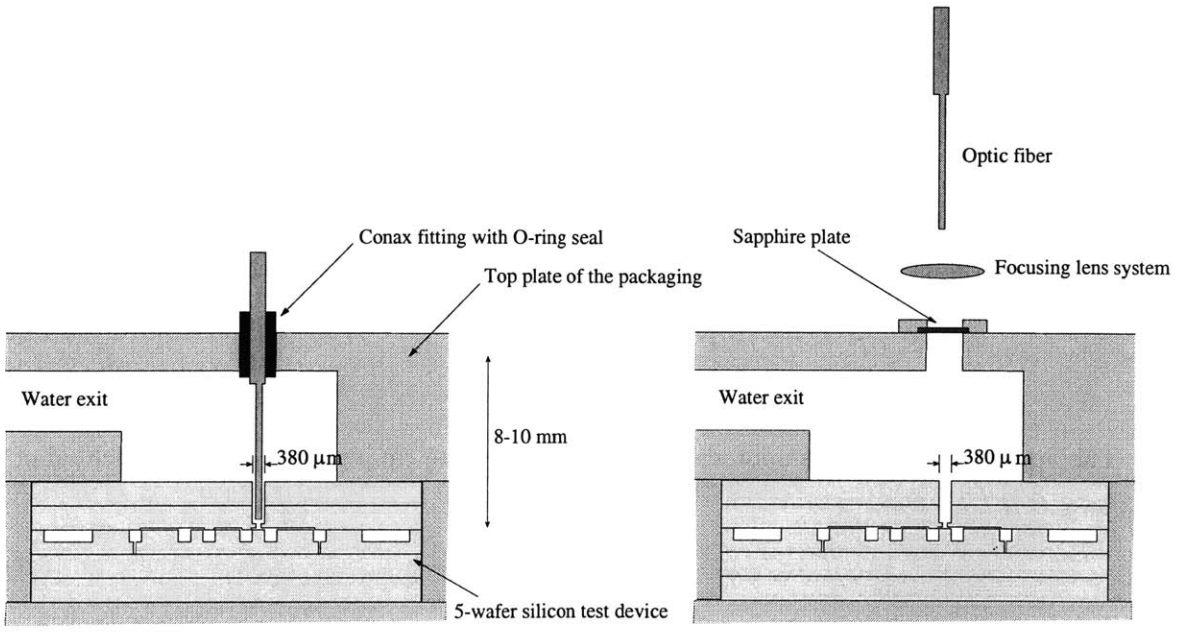

a/ intrusive sensor with pressure casing and Conax fitting

b/ non-intrusive sensor with optical focusing system

Figure 3-6: Speed sensor configuration propositions

3.3.2 Optical systems for an external sensor solution

The non-intrusive solution was investigated. The optic fiber needs coupling to a focusing lens system. Five optical systems were proposed:

- a plano convex singlet lens - its small size makes it difficult to mount and position, and this lens leads to a large spot size due to spherical aberration
- an achromat lens - has better performance in terms of spherical aberration, and allows a large standoff distance
- a pair of identical achromats - allows correction of spherical aberration, but two lenses must be positioned
- a gradient index lens - performance and correction of aberration make it interesting; it is easier to position and mount, but the image distance is limited to 6.5 mm
- a group of collimating and focusing lenses for diode lasers - this more expensive solution presents optimal performance, since spherical and off-axis aberrations are corrected; yet, two optical systems have to be positioned.

The first four systems have been tested. A plano-convex singlet lens 01LPX415, achromat lenses 01LAO001, and a gradient index lens 06LGO214 were bought from Melles-Griot. For the first two systems, the distances s between the lens and the target (hole in the die, diameter h = 380 μm) and s" between the fiber and the lens are calculated from the paraxial formulas. The fiber has an active diameter h" = 160 μm, the optical magnification is then $m = h''/h = 0.42$. The paraxial formulas are, with f the focal distance of the lens :

$$\begin{cases} f = m.\frac{s+s''}{(m+1)^2} \\ s(m+1) = s + s'' \end{cases}$$

The approximate on-axis spot-size diameter at infinite conjugate due to spherical aberration is [17]

$$D = \frac{0.067f}{f_{/n}^3} \tag{3.1}$$

where the focal number $f_{/n}$ is the focal distance to lens diameter ratio f/Φ.

This gives a die to lens distance of 8.5 mm for the plano convex singlet lens (f=2.8mm), and 33.8 mm for an achromat lens (f=10mm). The spot size diameters are respectively 238 and 144 μm.

With the pair of achromats, each lens works at its focal point. The correction of spherical aberration allows a diffraction-limited spot size[2] of 8 μm. This system allows a 10 mm die - lens distance.

Finally, the gradient index lens only allows a 6.5 mm distance from the die to its extremity.

The four optical collimating systems previously described have been successfully operated. The signal to noise ratio is lower than when the fiber optic sits right on top of the speed bumps, but is large enough so that the rotor speed information could be obtained with each optical configuration. A comparison of the signals obtained is shown on Figure 3-7.

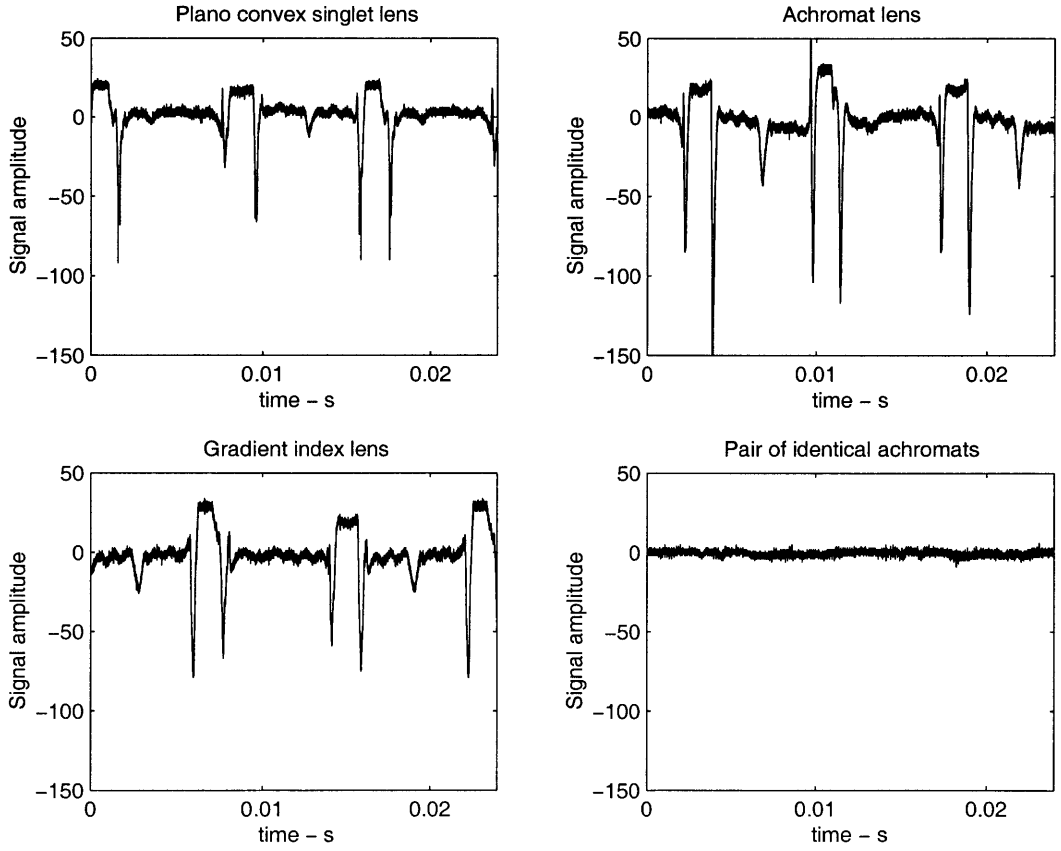

Figure 3-7: Comparison of the optic fiber output for the four optical collimating systems

The signal to noise ratio is maximum when the achromat lens is coupled to the Philtec. Moreover, this lens was found to be the easiest to use experimentally, is the most tolerant

[2]The approximate on-axis spot size of a lens at infinite conjugate due to diffraction is [17] $D = 2.44\lambda f_{/n}$ where λ is the wavelength of the light beam

since the output is less sensitive to a spatial displacement of the lens or the fiber, and allows the greatest standoff distance. The achromat lens was thus the selected optical device for the liquid bearings experiments. The maximum output is reached when the lens is positioned 37 mm above the die (top to top), and the fiber probe tip 13 mm above the lens. The rotor speed information is lost when the lens is displaced 25 μm radially, or 1 mm axially, or when the fiber is displaced 70 μm radially, or 1.25 mm axially.

Figure 3-8 shows a comparison of the fiber output obtained in the die-intrusive configuration as used in the gas bearings experiments, and of the output obtained when the fiber is coupled to the selected achromat lens. As previously shown in Figure 3-6, an optical window in the packaging is necessary for the light beam to reach the die while ensuring a sealed exhaust. To prove the validity of this concept, half-inch thick plates of pyrex and quartz are positioned between the die and the lens. The signal output are presented on Figure 3-8.

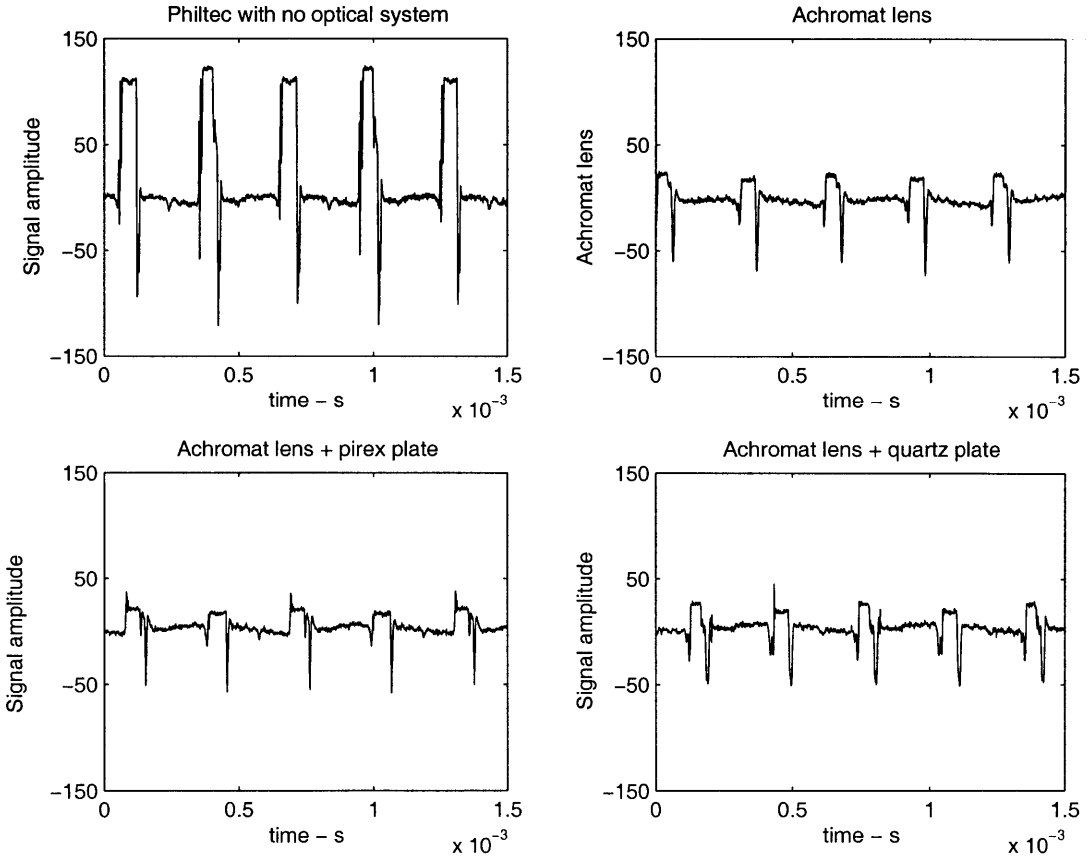

Figure 3-8: Comparison of the optic fiber output in its optimal configuration as used in the gas bearings experiments, and coupled to an achromat lens. Thick pyrex and quartz plates are inserted between the lens and the die to simulate a glass window

As can be seen, the signal to noise ratio is reduced by 50% while increasing the standoff distance of the optic fiber with the lens. The pyrex or quartz plate result in another 30% reduction in the signal output. However, the standoff distance of the speed sensor system has been increased to 37 mm, which is enough to accommodate the top plate of the packaging, an optical window and its cover, and bolts heads; and the signal strength of this system allows speed measurement.

3.4 Data acquisition system

The operating parameters are recorded using a PC-based data acquisition system (DAQ). The liquid bearing experimental setup shares its data acquisition system with the setup of [31]. A 300 Mhz Dell PC acquires and records the output of the pressure transducers and speed sensor. The transducers are connected to a National Instruments terminal block SCXI-1303. The pressure signals are conditioned in a 32-channel adjustable gain signal conditioner SCXI-1000and then sampled at 50 kHz on a National Instruments PCI-6043 Card. Labview software is used to implement the DAQ, and to display real-time data on the computer terminal. The average of 200 samples is recorded and displayed.

Chapter 4

Liquid Bearings Experiments

This chapter presents the results of the liquid bearings experimental test effort. As explained in Section 2.4, the goal of the experiments is to demonstrate the feasibility of liquid bearings at micro-scale by running experiments on an existing device, the micro-bearing rig, designed for gas bearings. The micro-bearing rig geometry is presented in Section 2.4.1. The analysis performed in Section 2.4 suggests that operation of these micro-bearing rigs is feasible with water.

Four types of tests are reported here: packaging assessment, capillaries flow characterization, thrust bearing flow characterization, journal bearing static flow characterization, and rotor spin tests. The packaging assessment establishes functionality, and that the center O-ring does not affect operation. The static flow tests characterized the functional behavior of the thrust bearings and journal bearing pressurization system and validated that behavior against theoretical predictions. The dynamic tests demonstrated the feasibility of liquid micro-scale bearings, and characterized the behavior of spinning devices.

4.1 Packaging assessment

The packaging presented in Section 3.1 is assessed with three experiments: leak test, gas static flow tests, spin test.

A leak test was performed with a blank die. This die is fabricated by bonding five silicon wafers identical to the wafers used in the micro bearing rig device fabrication, which has the same dimensions as the test devices. The blank die was inserted in the packaging, and

each port was pressurized to 150 psi. No leaks were observed, which shows that the O-ring compression is sufficient to ensure leak-free water connections.

Gas static flow tests were performed with a same die both with the gas and liquid packaging. These tests are intended to verify the functionality of the packaging. As was seen in Section 3.1, the packaging/die interface is the same for the gas and water packages, except that the liquid packaging has a supplementary center o-ring to enable a pressurized exhaust. The groove for this center o-ring was designed for a 10% o-ring compression, to avoid closing the thrust bearing gap with too large a deflection force. Given that the sealing of this o-ring has been demonstrated, a thrust bearing gas flow comparison between the two packages is necessary to quantify this effect.

Figure 4-1 presents the results of gas flow tests in the thrust bearings and in the journal bearing, for a same die in the gas packaging, in the water packaging without the center o-ring (this o-ring is not necessary for the present test since the exhaust is to atmosphere), and in the water packaging with the center o-ring.

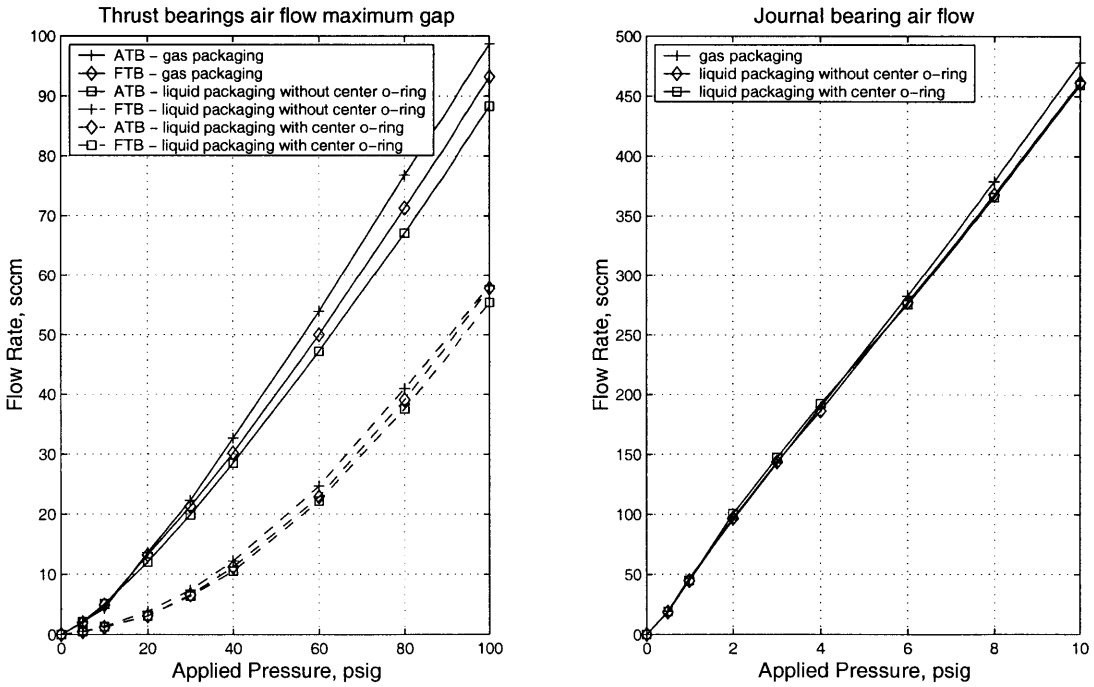

Figure 4-1: Packaging comparison - Left : Thrust bearings air flow at max gap - Right : Journal bearing air flow.

As can be seen from the thrust bearings flow tests, the liquid packaging without the

center o-ring introduces extra resistance to the flow, since the flow rate is lower by roughly 5% than in the gas packaging, for a given pressure. This effect is probably explained by the fact that the liquid packaging is larger in size, and the ports are longer. The diameter of the ports is the same in both packages, and is smaller than the rig line diameters. The resistance of these ports to the fluid is not negligible, and is relatively more important in the liquid packaging.

The center o-ring introduces a decline in flow rate that is the same order of magnitude of the one previously noted. This shows that this o-ring deflects the die, but that this effect is minor. The deflection was quantified using the thrust bearing gas model. It was found to be approximately 0.015 μm (i.e., the relative closure of the gap due to the deflection force is 0.5%).

The journal bearing flow tests indicate that the center o-ring does not play a role here, as expected. The flow rate for a given pressure is 3.5% lower with the liquid packaging. The extra resistance is probably due to the longer ports, as for the thrust bearings.

4.2 Thrust bearings water flow tests

Experimental performance evaluations of the thrust bearings are needed to evaluate the models. Lin stated that the gas flow measurement is a tool for deducing feature dimensions [25]. In this section, we use the gas model to deduce the dimensions of the microfabricated flow channels, and we compare the liquid thrust bearing simulation results on this inferred geometry to the experimental results. This allows us to recalibrate and modify the model.

4.2.1 Thrust bearing capillary flow tests

Pressure-flow characteristics of the capillary alone were performed on the die MCBR 6-7 (the rotor fell out during fabrication). The thrust bearing is then composed only of a set of capillaries, so it is possible to evaluate the capillary model independently.

Gas and water flow experiments were performed on the aft thrust bearing capillaries of the die 6-7. This die fabricated by Wong has hybrid thrust bearings, and thus has 20 capillaries [42]. The gas and liquid capillary models presented in Section 2.2 and more precisely described in Appendix A are used to predict the pressure-flow characteristics for several values of capillary diameter. The tests and models results are presented in Figure

4-2.

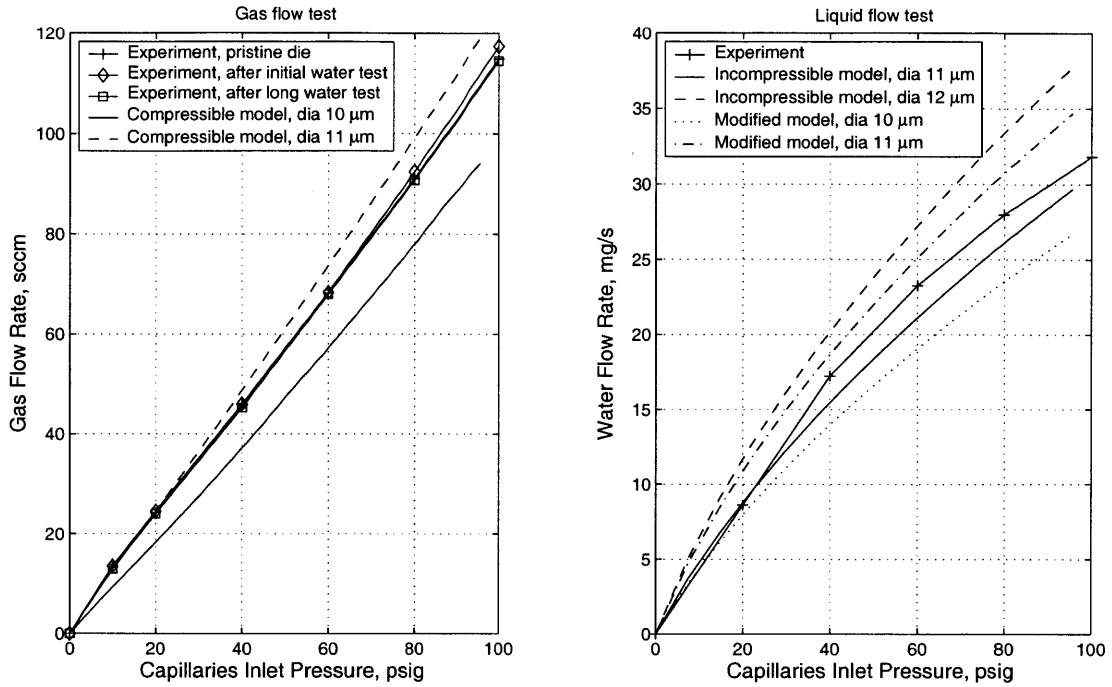

Figure 4-2: Capillary flow test. Comparison of experimental and model results for gas and liquid flow. Tests are run with die MCBR 6-7.

The gas tests are a reliable way to estimate the geometry [25]. The nozzle diameter was inferred from the gas tests/model comparison. As can be seen from Figure 4-2, the gas flow test indicate a capillary diameter of 10.7 μm. Liquid experiments were performed, and the results were compared to the incompressible capillary model prediction. The liquid model was modified by adding an additional, empirical parameter to decrease the flow resistance to compensate the flow rate under-prediction. Figure 4-2 shows the predictions from the baseline model, and from the modified model.

These results also show that the gas flow is the same for a pristine die [1] and after a 2 hours long water flow test. This shows that a properly conducted water flow test does not leave residue, film or other source of flow blockage, after the die is dried. The contamination issue is treated more extensively in Appendix C. It is also seen that the flow after a short water test is slightly larger than before the test, and than after a long water test. There is no physical explanation for that, except a packaging difference in this experiment. Perhaps

[1] We call *pristine* die a die that has not been put in contact with water, except during the manufacturing process

an o-ring misplacement might have caused this.

4.2.2 Complete thrust bearings flow tests

Flow tests on complete thrust bearings were performed. Following the same procedure as in the previous section, these tests allow calibration of the radial outflow resistance in the incompressible model [2]. The geometry was inferred from tests/model comparison with gas. Flow tests were performed with water for the forward and aft thrust bearings, and were predicted for the liquid model on the inferred geometry. Tests are performed on a die whose rotor is not released, and hence the thrust bearing gap is constant. The results are presented in Figure 4-3.

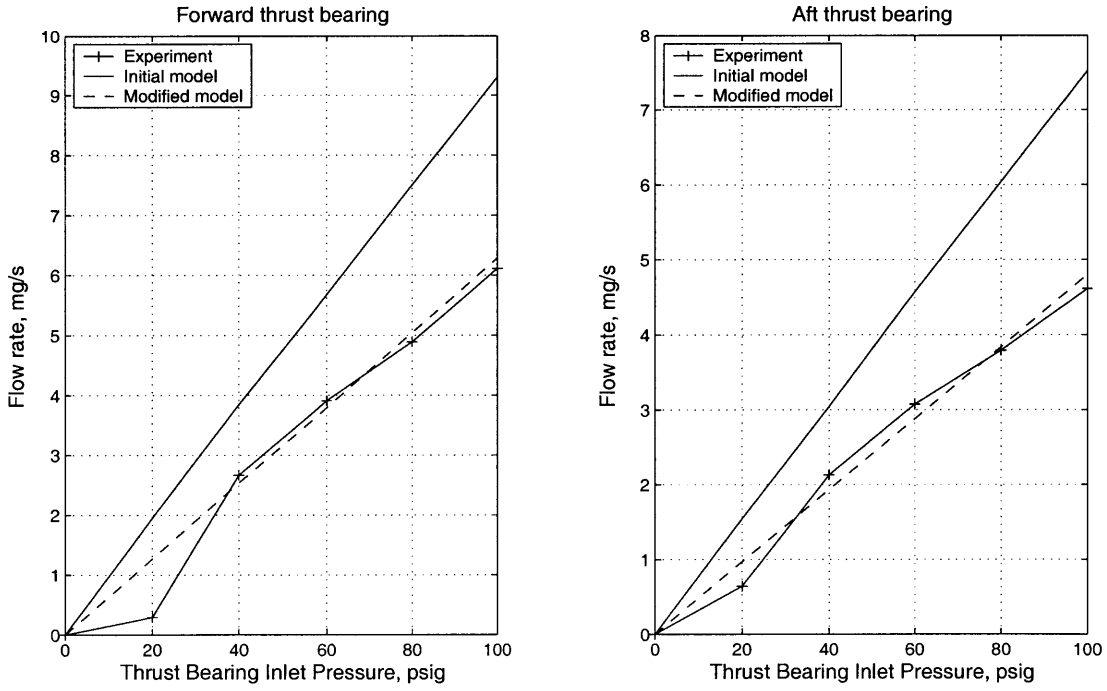

Figure 4-3: Thrust bearing liquid flow test. Comparison of experimental and model results. Tests are run with die MCBR 5-4. The rotor has not been released.

As can be seen, the flow predicted by the model is approximately 50% larger than that observed in the experiments. The radial flow resistance model assumes a fully developed

[2]As was seen, the flow encounters three resistances in the thrust bearing: the capillary resistance, the inherent resistance, and the radial outflow resistance. Both with gas and water, the inherent resistance represents a small fraction of the total resistance, and its calibration is not necessary to the full model first-order calibration.

Poiseuille flow, for which the friction factor is $f = 64/Re$. This resistance is increased in the modified model to account for this over-predicted flow. This observation is consistent with a number of papers on microchannels water flow. Mala and Li [15] state that the correlations between the friction factor and the Reynolds number for microchannel flow are very different from that in classical theory of fluid mechanics. The apparent viscosity and the friction factor of a liquid flowing through a microchannel may be several times higher than that in the conventional theories. Wilding et al. [29] analyzed flow of water in trapezoidal cross-sections silicon microchannels. Their data indicated an approximately 50% increase in the friction factor from theoretical values. Similar results were obtained by Jiang et al [43].

The experimental results follow correctly a linear pressure/flow rate characteristic, except at low pressures ($P_{in} < 40psig$) where the flow rate is smaller, as shown in Figure 4-3. This blockage at low pressure is believed to be due to surface tension. It is likely that some air bubbles were trapped in the thrust bearing gap during these flow tests. The pressure drop across a water/air interface of radius of curvature r is

$$\Delta P = \frac{2\sigma}{r} \tag{4.1}$$

where $\sigma = 0.0728N.m^{-}1$ is the surface tension of water at room temperature. The gap dimension of this die, for each thrust bearing, is approximately 1.6 μm. An interface of this diameter would then sustain a pressure differential of 26.4 psi. This value is consistent with the observations. Some gas bubbles trapped in the thrust bearing gap could block a large part of the flow for pressures lower than 30 psi. At a larger pressure, these bubbles are convected downstream.

The modified model was evaluated for larger gaps. A die for which the rotor has been released and is free to move axially was tested. Pressure/flow characteristics were performed successively on each thrust bearing. Pressure is applied in only one thrust bearing, and the other is vented. This closes the vented bearing gap, resulting in a known, maximum gap. The geometry is obtained from gas tests, and is used in the liquid modified model to predict the thrust bearing flow rate. Results are presented in Figure 4-4.

As is seen, the modified model is only a rough estimate of the flow. Experimental results show a flow rate lower by 8 to 20% than predicted for the aft thrust bearing, and 5 to 40%

lower for the forward thrust bearing.

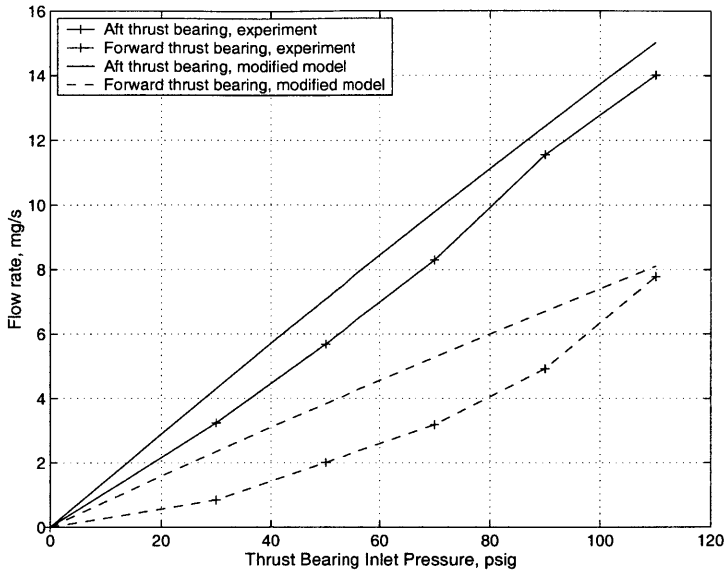

Figure 4-4: Thrust bearing water flow test at maximum gap. Comparison of experimental and model results. Tests are run with die MCBR 3-11. The rotor has been released.

4.2.3 Rotor axial position flow tests

The load capacity and stiffness of the thrust bearing can not be directly measured experimentally, since it was not possible to implement a force and position sensor. A rotor axial position test designed by Lin [25] is used to provide data to confirm the accuracy of the force predictions of the model.

One thrust bearing is pressurized to a fixed pressure, and the pressure in the second thrust bearing is increased from zero. Initially, the rotor is clamped to one side. As the higher pressure in the second thrust bearing pushes the rotor, the flow rate in the first thrust bearing decreases due to the decreasing gap.

Experimental results were obtained, and are compared to the modified incompressible model in Figure 4-5. The transition from high flow to low flow is smoother than predicted by the model. This indicated a stiffer bearing.

From these comparisons, it appears that the modified thrust bearing model is a useful tool to approximate the thrust bearing flow rates, and then predict bearing stiffness and load capacity. However, this model is not a satisfactory tool to provide a non-destructive

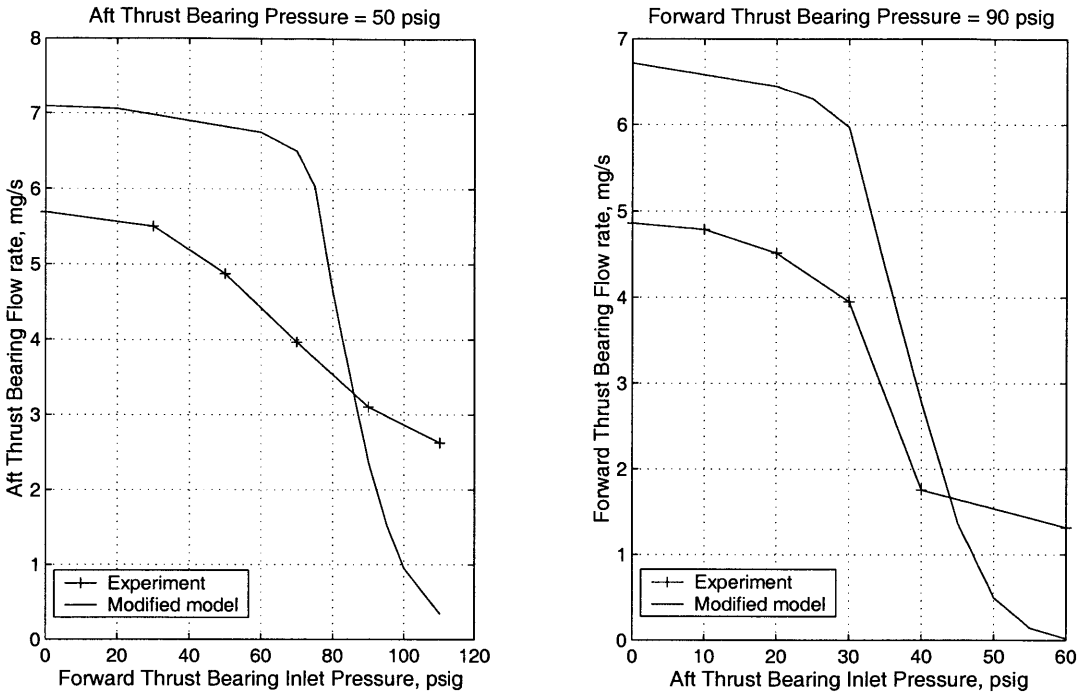

Figure 4-5: Rotor axial positioning test result from die MCBR 3-11. Comparison of experimental and model results for water flow.

measurement of the geometric characteristic of the bearings. The bearing stiffness sensitivity to the geometry imposes tight fabrication tolerances. If used as a measurement tool, the model/experiment deviation must be small compared to these tolerances. The model may be improved by implementation of the friction factor correlations found in the microchannel flow literature [15, 43, 29].

4.3 Journal bearing flow test

The axial journal bearing flow was measured for three different dies, and compared to the prediction of a Poiseuille model. Experimental and modelling results are presented in Figure 4-6, for an axial pressure differential of 0 to 20 psi. As can be seen, the flow measured for the two dies from build 3 are close; they differ by less than 10%. This result is expected since these two journal bearings were etched at the same time, and should have similar geometries. For a given dp, the flow for the die from build 2 is 15% larger.

In the range $dp = 5$ to $20psi$, the results are in rough agreement with a $10 \pm 0.3\mu m$ gap, as predicted by the conventional theory. For smaller dp, the results are closer to the

11 μm gap simulations. We know that the time-multiplexed DRIE generally produces a journal gap of 11 to 12 μm. The flow rate observed is smaller than the Poiseuille prediction, and the departure of the flow characteristics from the theory is larger when the pressure gradient is increased.

These observations are in good agreement with the literature. Mala and Li [15] have observed that for a given flow rate, the required pressure gradient to force the liquid through the microtube is higher than predicted by the conventional theory, and that the deviation increases with the Reynolds number. They propose a roughness-viscosity model to explain their data.

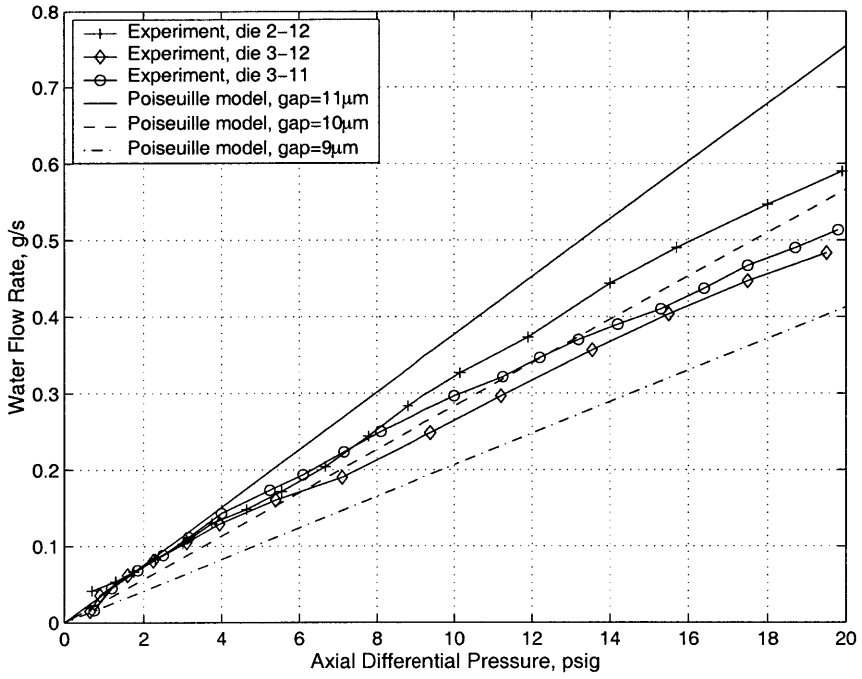

Figure 4-6: Journal bearing water flow tests and Poiseuille model prediction.

The journal bearing gap is critical to the bearing performance. We can estimate the gap size of the devices by matching the measurement to simulation results. As was seen, the Poiseuille model is not an accurate tool. With careful calibration of the model, or implementation of roughness model, the flow measurement could be a valuable measure of the journal bearing dimensions.

4.4 Rotor spin tests

A single device was successfully spin tested. We have demonstrated stable micro water-bearing operation. The maximum rotational speed achieved by the liquid micro-bearing device is 21,000 rpm. The rotor crashed at this speed, but the limiting factor to bring this device to higher speeds is the test rig. The turbine inlet absolute pressure required to drive the bearing rig at 21,000 rpm was 120 psi, which is the upper limit of the experimental rig. This section introduces the setup, summarizes the tests and identifies the main issues with water micro bearing operation. Emphasis is given on the differences with gas operation.

4.4.1 Setup and experimental requirements

The experimental setup is presented in Chapter 3. Prior to an experiment, the supply tank was filled with water, vacuumed to degas the water, and pressurized to 250 psi. The dump tank was almost emptied and pressurized to 15 psi. It was observed that it is necessary to pressurize the exhaust to get rid of gas bubbles in the die and the packaging, and test the rotor in a continuous media. Spin tests with the exhaust to atmosphere were unsuccessful. Gas bubbles would almost continuously flow from the exhaust of the die, blocking the optical path for observation and speed sensing.

Occasionally, gas bubbles would be convected by the flow, and get trapped by the sapphire window in the packaging. Unscrewing the aluminum cover allows a slight leakage from the packaging window, and getting rid of these bubbles.

Depending on the tests performed, the tank allows a test duration of 25 to 50 minutes. It is important to stop the test before the tank is empty so as not to contaminate the rig tubing with gas.

Finally, the speed sensor configuration proposed in Section 3.3 was successful. The presence of the sapphire window and the water resulted in a higher noise-to-signal ratio, but did not modify by a large amount the optimal positions of the lens and the fiber. It was difficult to obtain a signal at first, but this configuration proved efficient and easy to reposition. The vertical alignment of the fiber is believed to be the critical issue.

4.4.2 Summary of tests

A single device, MCBR 2-1, was tested. We know from gas operation that this die has a slightly leaky forward thrust bearing. It was found that both for starting and operation, the axial balance was critical, and that this was a stronger requirement than for gas. This is due to the larger pressures involved with water.

The pressure in the forward thrust bearing was 100 to 110 psig. The pressure in the aft thrust bearing was 30 to 40 psig. Outside of this range, it was not possible to start the turbine. A turbine inlet pressure of 30 to 50 psig[3] was necessary to start the turbine. This is very high compared to gas where this same die would start spinning without main air, or just with a fraction of a psi. A MOP pressure of 13 to 25 psig was necessary to start. It is surprising that the turbine would not start without MOP and with a higher aft thrust bearing pressure, since they both bring load capacity at the same location on the rotor. Moreover, the MOP imposes a larger load to the back of the rotor than what seemed to be tolerated from the aft thrust bearing. Indeed, a change in the aft thrust bearing supply pressure from 20 to 50 psig increase the force on the rotor by 0.13 N (the rotor did not spin, or crashed, at 50 psig), while a MOP differential pressure of 15 psig (observed to necessary) imposes a force of 0.8 N. This issue needs to be explored in further tests.

Figure 4-7 shows a typical spin test. The rotor starts, accelerates while the main pressure is increased, crashes three times at 14,000 rpm, but continues to spin (after perhaps hitting a wall) and then crashes without automatic recovery[4]. The turbine is restarted, and accelerates up to 21,000 rpm before crashing.

Figure 4-8 illustrates a spectrogram from a die accelerating from 1,400 to 7,500 rpm. It is verified with an oscilloscope that the main peak is at the rotating frequency. Depending on the fiber optic position, the highest signal is sometimes twice the rotating frequency since the rotor has two speed bumps.

[3]This is a differential pressure, relative to the exhaust pressure

[4]Around t=300 sec on Figure 4-7, the rotor does not spin and the rotating speed is zero. The speed is acquired from the spectrum analyzer, which makes a Fourier transform of the signal from the fiber optic, and takes the frequency of the highest amplitude peak. When the rotor is static, the frequency corresponds to the ambient noise.

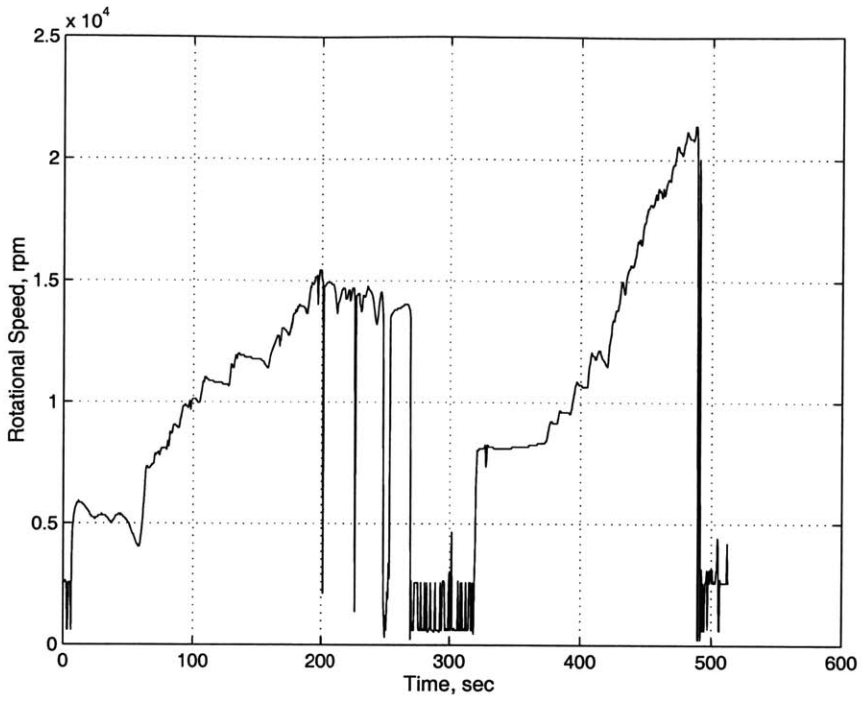

Figure 4-7: Spin test of the liquid micro-bearing device 2-1. The device accelerates and then crashes. It is restarted, and accelerates up to 21,000 rpm.

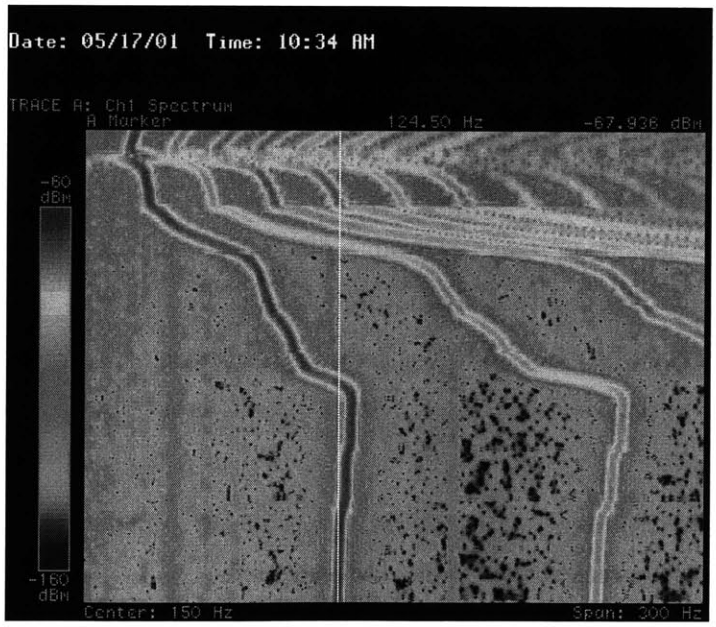

Figure 4-8: Spectrogram for the water bearing accelerating to higher speed.

The operating line is presented in Figure 4-9. Rotating speed is plotted versus the turbine inlet differential pressure, for three runs. The curves are very repeatable, and suggest that very high pressure is necessary to drive the turbine to high speed. As previously anticipated in Section 2.4, the turbine has to overcome large viscous drag, which results from a combination of small gaps and large density. This device was designed for gas, and has a too large viscous drag for high-speed operation, since it has a simulated high drag electric generator region on the back of the disk.

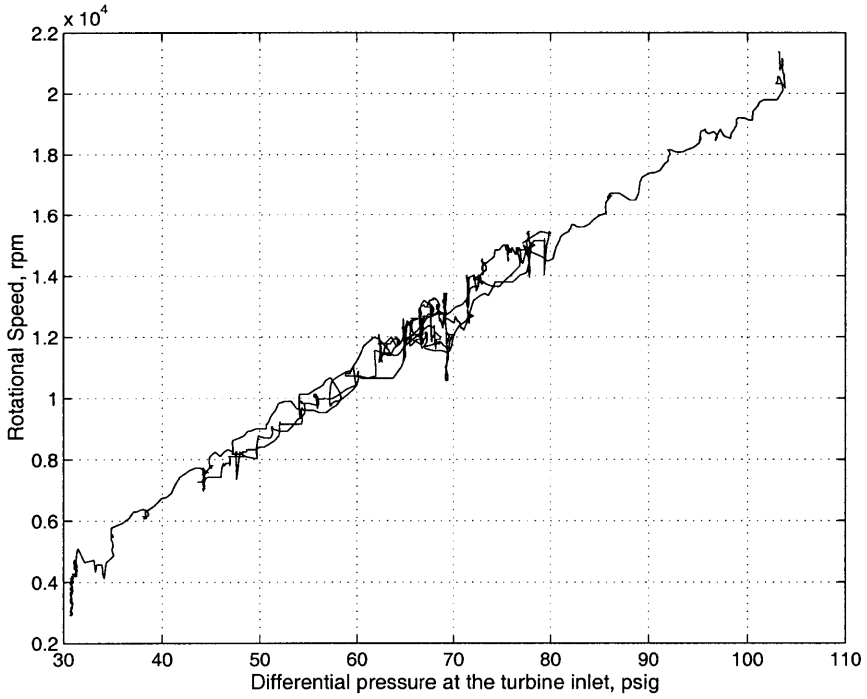

Figure 4-9: Operating line. Main pressure - speed relationship for die 2-1.

The rotating speed of 21,000 rpm was achieved with a turbine mass flow of 2.05 g/s. This is consistent with the 1-D model based on velocity triangles and viscous drag presented in Section 2.4.4. For this speed, a mass flow of 1.45 g/s was predicted. The difference may be due to 3D effects in the turbine, or larger viscous drag than predicted.

The secondary flow rate is the sum of the journal bearing, the thrust bearings and the MOP flow rates. This flow is only 0.02 g/s at 21,000 rpm. The secondary mass flow rate at the maximum speed achieved is thus less than 1% of the turbine flow rate.

The large axial, rearward load on the front side of the rotor associated with the high pressure in the turbine must be balanced. This requirement is more stringent here than for

gas bearings where the turbine pressure is of the order of only a few psi, and the thrust bearings are strong enough to carry the associated loads. Figure 4-10 presents that MOP operating line for three spin tests. As can be seen, the results are very repeatable.

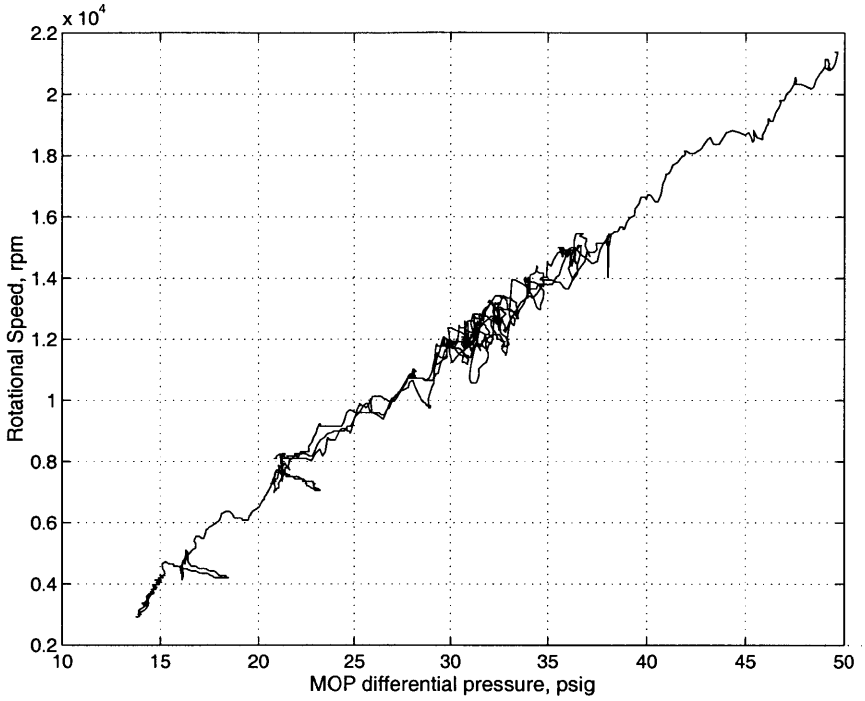

Figure 4-10: MOP operating line. MOP differential pressure - speed relationship.

The journal bearing behavior is investigated. The spin tests performed and the multiple crashes have suggested that axial balance was more challenging than radial balance. Spin tests are run, and journal bearing pressure is modified while the main pressure remains constant. Impact on the rotating speed, and on the stability, is observed.

Figure 4-11 shows the rotating speed and the turbine differential inlet pressure for this test. The journal bearing tests are performed during the several plateau of turbine inlet pressure. Such a plateau can be seen from seconds 390 to 515 on Figure 4-11.

Figure 4-12 shows how the journal bearing pressure affects the rotational speed. These data are acquired on nine plateau of the turbine inlet pressure. It is observed that for a given inlet pressure, the speed varies as dp is modified, and that there is a value of dp that maximizes the rotational speed. If dp is slightly different from this optimal, the rotational speed decreases. It was observed during the tests that if dp is too small or too large, the turbine goes unstable.

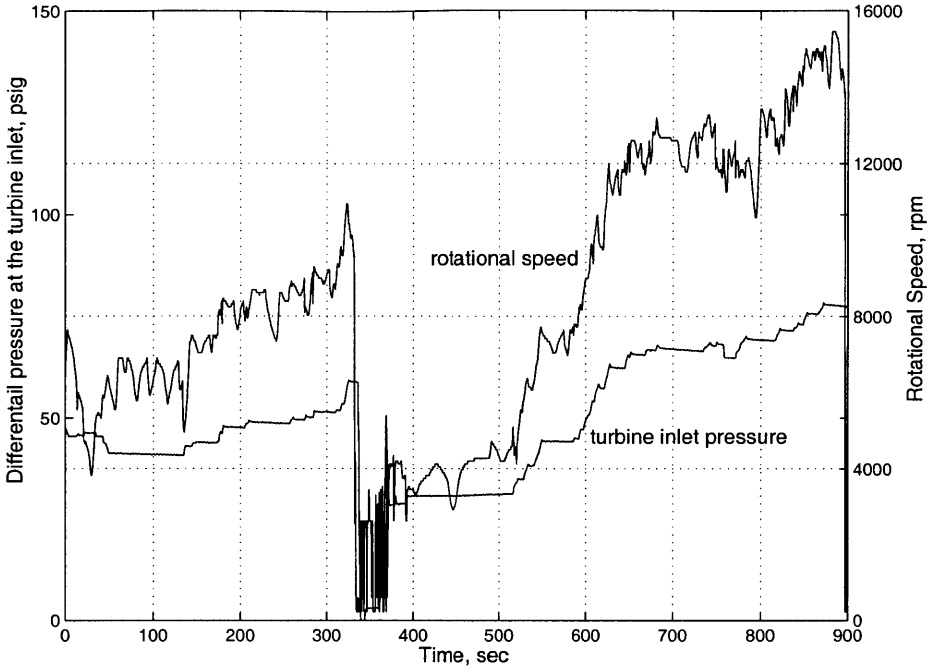

Figure 4-11: Rotational speed and turbine inlet pressure for the journal bearing investigation. Plateau of turbine inlet pressure are reached, during which the rotating speed is only a function of the journal bearing inlet pressure.

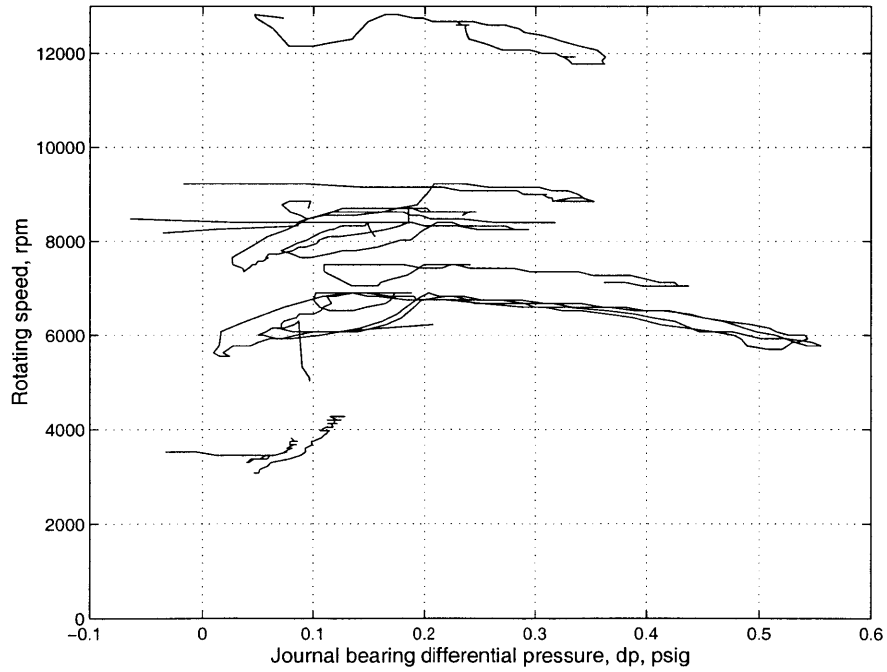

Figure 4-12: Rotational speed - journal bearing axial differential pressure relationship.

More extensive tests must be performed, but these early data suggest that a dp of 0.15 to 0.2 psig maximizes the speed and the stability for rotational speeds of the order of 10,000 rpm. From the model presented in Section 2.3.2, a dp of 0.2 psig yields a bearing natural frequency of 15 Hz, suggesting that the bearing is operating super-critically. From gas bearing experience of transition from subcritical to supercritical operation, it is not likely that the bearing is rotating super-critically in this case. The journal bearing model should be investigated.

As can be seen from Figure 4-12, stable operation was achieved with zero dp, or negative dp. This might suggest hydrodynamic operation. Future experiments are needed to confirm this hypothesis. The aft thrust bearing flow and the MOP flow exit through the journal bearing, which may be an unaccounted for source of additional hydrostatic stiffness.

4.5 Conclusion and future tests

Water micro-bearing operation was demonstrated. Static flow tests were used to calibrate the thrust bearing model. Spin tests allowed a first assessment of the journal bearing behavior, and a verification of the predicted drag on the rotor. A successful experimental setup was implemented for these tests, and is of use for future liquid tests.

Only low-speed operation was achieved. The maximum speed of 21,000 rpm was limited by the experimental rig. The pressure is limited by the mass flow meters and the filters used. The rig is not compatible with high-speed water operation in this device designed for gas. A large mass flow is required, and the pressure drop in the main flow and exhaust lines was large during the tests.

For future tests on the same die, the rig must be transformed for higher pressure and larger flow operation. For high-speed operation, a new device must be designed. Bearings must be designed with the thrust liquid bearings model, and a incompressible journal bearing model must be investigated. Drag is a major design parameter for a liquid device. Therefore, two obvious changes are to increase the depth of the aft plenum to decrease the drag, and to increase the blade height to obtain a larger power from the turbine.

Chapter 5

Design of a Micro Turbopump

This chapter describes the overall design of a demonstration micro turbopump. The functional requirements and design constraints are defined. The design of the two primary subsystems, the rotating turbomachinery and the gas-bearing system, is presented. The fundamental engineering issues are identified, and the tradeoffs are quantified.

5.1 Introduction

The microrocket engine concept requires propellant internal pressurization. A turbopump feed system employing an expander cycle has been selected for the engine. The required pressure at the inlet to the cooling passages and therefore at the pump exit is 300 atm. To demonstrate the feasibility of the concept, a micro-scale turbopump producing a pressure rise of 30 atm for water was designed. For this first design, the turbopump is not strictly considered as part of the rocket system. In the cycle envisioned for the rocket engine, liquid propellant is pressurized in the pump, then heated in the cooling jacket, enters the turbine in a gaseous or supercritical state, and finally is injected into the combustion chamber. The enthalpy rise that occurs in the cooling jacket is converted to kinetic energy by the turbine, which drives the pump. The demonstration or 'demo' turbopump presented here has two different fluid and flow paths, one for the turbine and one for the pump. It also has externally pressurized air bearings.

The pumping power is provided by a turbine driven by pressurized air. An innovative annular arrangement is proposed, where the centrifugal pump blades and the radial inflow turbine blades are coplanar, on the same side of a single wafer rotor. A seal is provided by

an annular hydrostatic thrust bearing positioned between the two. Rotor radial support is provided by a hydrostatic gas journal bearing. A cross-section of the turbopump concept is shown in Figure 5-1. The device consists of five fusion-bonded silicon wafers and one anodic bond of a pyrex wafer. Top and bottom views of the exploded 6-wafer view are presented in Figure 5-2. The outer diameter of the rotor is 6 mm, and both the pump and turbine blades are 225 μm high. The turbopump is designed for a mass flow of 2.5 g/s of water, at a pressure rise of 30 atm. The lower pump pressure was selected for two reasons:

- to lower technical risk in demonstrating the world's first MEMS turbopump,
- 30atm is the pressure rise required of a boost pump if cavitation behaves at micro scale as it does at larger scale.

The design of each component: turbomachinery and bearings, is detailed in the following sections. A complete list of design or functional requirements, specifications, and realizations is presented in Appendix D. It represents a summary of this design as well as a convenient reference.

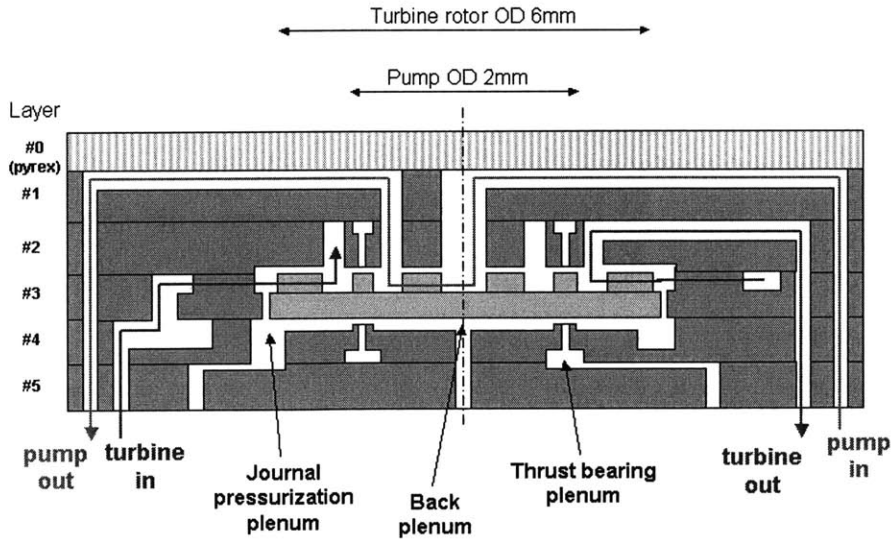

Figure 5-1: Cross section of the micro-turbopump concept. Vertical dimension not to scale.

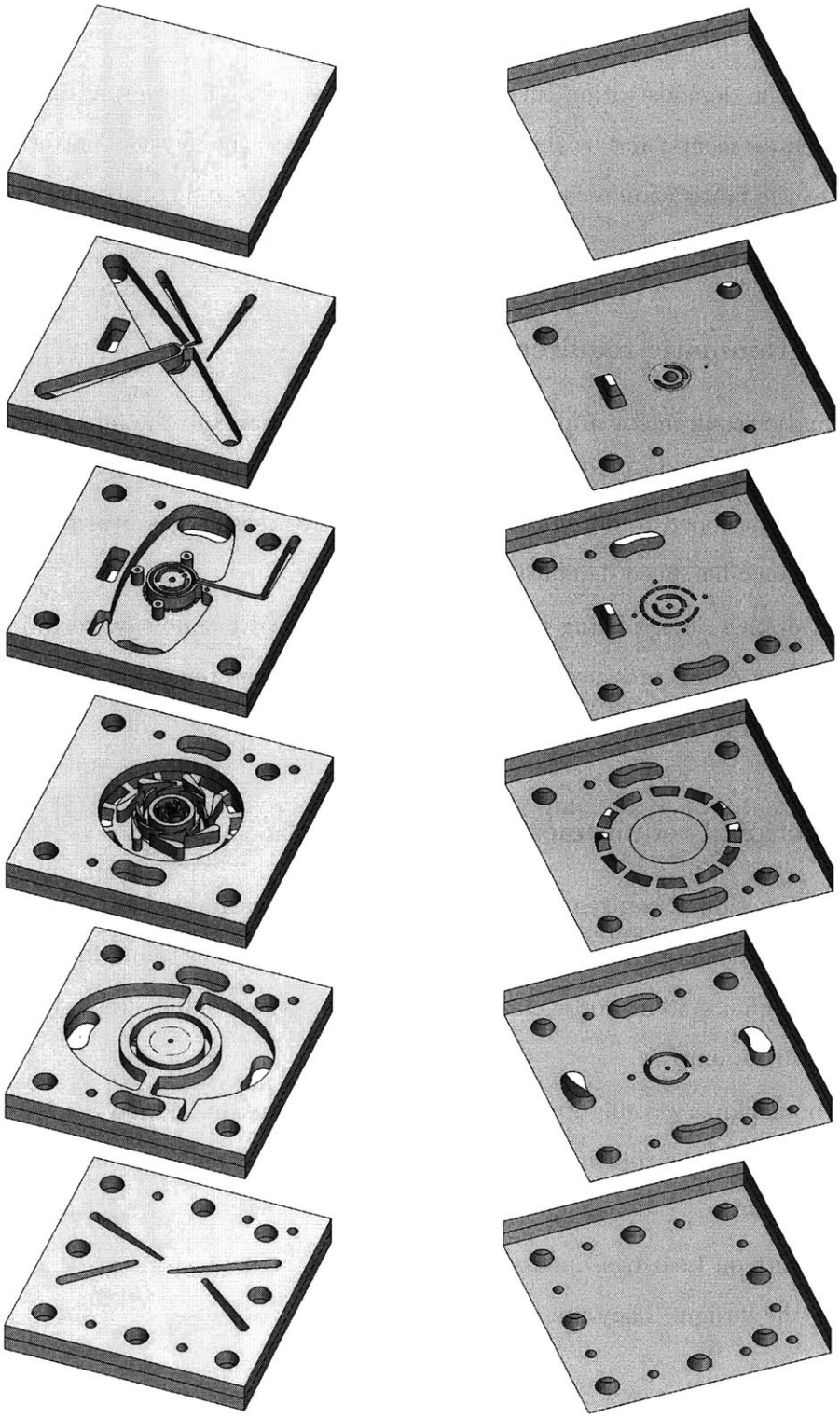

Figure 5-2: Exploded top and bottom views of the turbopump stack. 3D rendering realized by Diana Park. Vertical dimension not to scale. The horizontal separation that appears on each layer comes from the rendering and is not representative of the design.

5.2 Requirements and constraints

The design of the demonstration turbopump was driven by the programmatic, functional and testing requirements, and by the constraints inherent to the physical performance of the device and to the fabrication technology. These requirements and constraints are presented in this section.

5.2.1 Programmatic requirements

A programmatic requirement imposed was to keep the design and the fabrication processes as close as possible to those of the existing micro-bearing rig so as to make best use of the experience developed to date in these fields. For this reason, gas bearings were chosen. Their performance has been demonstrated.

The goal of this device being to demonstrate a critical technology, technical risk was mitigated. Lower pump pressure than the rocket engine requirement is chosen, and water is selected as demonstration fluid.

5.2.2 Functional requirements

The principle functional requirement is to demonstrate the feasibility of a MEMS turbopump system. Since 30 atm is believed to be the pressure rise required from a boost pump in the micro rocket engine system, for a mass flow of 2.5 g/s, these values were the design goals of the demo turbopump.

The turbomachinery configuration chosen and presented in Section 5.3.1 imposes that the turbine has the same rotating speed, the same mass flow, and the same blade height as the pump.

Requirements on bearings, internal pressure drops, structural integrity and drag have been driving the design. They are presented in Appendix D.

5.2.3 Experimental requirements

The demo turbopump design is constrained by the need to instrument the device for testing. This instrumentation is necessary to make performance measurements, and adds a level of complexity to the device.

Pressure, mass flow and speed measurements are necessary to understand the turbomachinery and bearings behavior. Cavitation understanding requires the observation of the pump blades trailing edge. The device is connected to the outside environment with o-rings that ensure sealed interconnects. For experimental convenience, all the connections are realized on the same side of the die. Finally, a center connection is avoided, since compression on the center of the die might result on the closure of the thrust bearing gap.

5.2.4 Performance constraints

The pump performance is limited by cavitation, which occurs when the pressure on the blade surfaces falls below the saturation pressure of the liquid.

The turbine must have sufficient mass flow, pressure ratio, and efficiency to deliver enough power to the pump. The large aspect ratio of the blades in a MEMS turbomachine leads to large 3D losses, and losses associated with tip-clearance effects. Conservative efficiencies of 30% are assumed both for the turbine and the pump.

5.2.5 Manufacturing constraints

MEMS fabrication technology is a severe constraint on the design. Three-dimensional features are formed by assembling two-dimensional shapes. Using nested masks allow a limited number of depth steps in a single wafer.

A feature of a silicon-micro fabricated turbopump is that it does not have an inducer like most macro-scale pumps. An inducer imparts swirl to the flow at the inlet of the pump, and is typically a three dimensional feature that can not be obtained with current micro-fabrication technology.

5.3 Turbomachinery and Fluid Dynamics

5.3.1 Configuration

The turbomachine consists of a single, thin disk, centrifugal rotor. It is radially supported by a gas journal bearing.

Preliminary studies of the pumping system layout considered several different configurations, shown on Figure 5-3. The configurations differ on a number of physical aspects that are discussed hereafter.

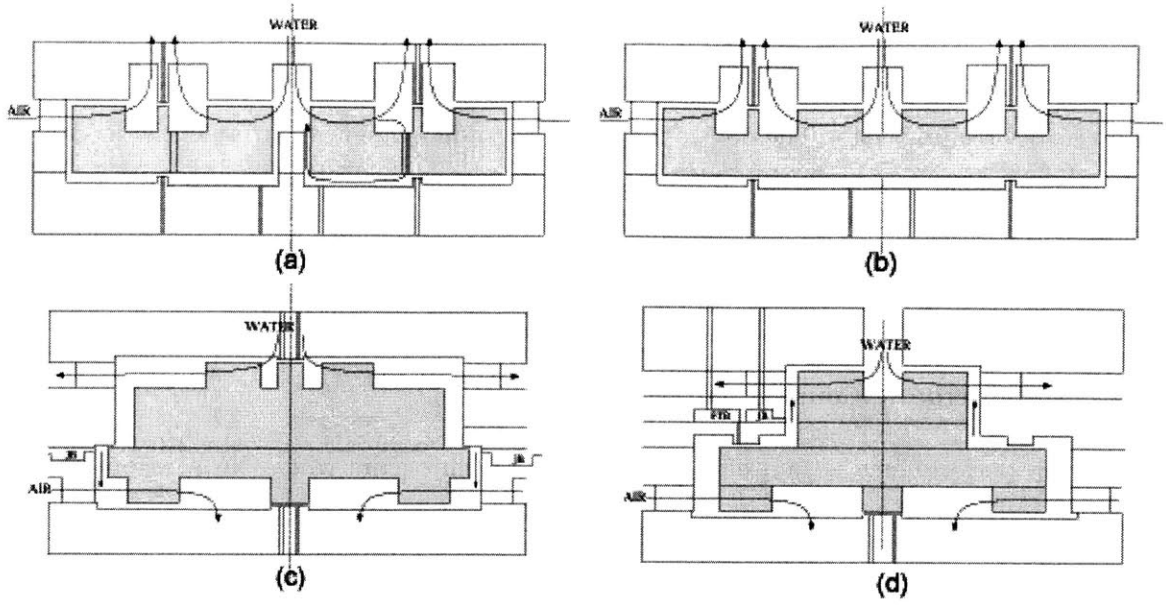

Figure 5-3: Initial concepts of the turbopump layout

- *thrust bearing center pad at the pump inlet* : this feature is undesirable since it yields a larger pump inlet radius to allow the right-angle turning of the flow. For a given rotating speed, a larger pump inlet radius means a larger tangential velocity, making the pump operation more sensitive to cavitation.

- *single- or multiple-wafer rotor* : a single-wafer rotor presents considerable advantage. It decreases the number of unproven fabrication and operation process steps, and reduces the potential for rotor unbalance, since no rotor wafer alignment in necessary. More experience is available with fabrication and high-speed operation of single-wafer rotors in the micro-bearing rig.

- *pump diffuser* : a diffuser consists of static vanes row at the pump exit. It improves performance due to static pressure recovery, and, thus, increases the pump efficiency.

- *center shaft* : the journal bearing can be implemented as a center static shaft, or at the edge of the rotor. The current fabrication capability limits the length to gap ratio to approximately 30:1. Thus, the circular bearing gap has been chosen to be 10 μm wide and 300 μm deep, the same dimensions as the micro bearing rig device. Hydrodynamic journal bearing theory states that the loading capacity and stiffness increase with the bearing length to diameter ratio (L/D) and with the inverse of the

gap to rotor radius ratio (c/R). A center shaft increases the L/D ratio, and the c/R ratio. The second effect is the predominant one on hydrodynamic stiffness. Further work needs to be performed to compare the two approaches in terms of hydrostatic stiffness, since hydrostatic bearings are used. The edge journal bearing is desirable since its operation and fabrication have been demonstrated. Moreover, a center shaft implies a liquid journal bearing, which has not yet been demonstrated at this scale.

Advantages and drawbacks of the configurations proposed are summarized in Table 5.1.

Table 5.1: Advantages and draw backs of the turbopump cinfigurations

Configuration (from Fig 5-3)	Advantages	Drawbacks
(a)	- single wafer rotor - no center pad - process close to the micro-bearing rig fabrication technology	- center shaft - no pump diffuser
(b)	- single wafer rotor - no center pad - edge journal bearing	- no pump diffuser
(c)	- edge journal bearing - pump diffuser	- center thrust bearings pad - two-wafer rotor
(d)	- no center pad - edge journal bearing - pump diffuser	- three-wafer rotor

Because of the large density difference between the liquid in the pump and the gas in the turbine, it was possible to design a rotor with the pump and turbine blades co-annular and planar. From the previous discussion, configuration (b) was chosen. The turbine is separated from the pump by an annular seal that also serves as a gas thrust bearing pad.

5.3.2 Pump and turbine design requirements

The pump functional requirement is a pressure rise of 30atm for a water mass flow rate of 2.5g/s, without cavitation, at an inlet pressure less than 3atm. To include rocket system design requirements, we also require

- the same mass flow rate in the turbine as the pump, 2.5 g/s
- the turbine inlet pressure to be less than the pump exit pressure (simulating the cooling jacket losses)
- the turbine exit pressure must be higher than the combustion chamber inlet pressure.

The fabrication process of the chosen configuration imposes the same blade height for the pump blades and the turbine blades, and the same rotating speed.

Finally, conservative efficiencies of 30% are assumed both for the turbine and the pump. In the expander cycle proposed by Protz [33], the enthalpy rise that had occurred in the cooling jacket is converted to potential energy by the turbine. The pump and turbine efficiencies are playing a role only in this energy conversion. Thus, in this regenerative rocket engine turbopump, efficiency is not an issue as long as the turbine delivers sufficient power to drive the pump to the desired speed. The rate of heat absorbtion in the cooling passages is large enough so that the heat load is two orders of magnitude larger than the pumping power needed [33]. This suggests that pump efficiency is not a driver in this design.

5.3.3 Pump design

In a centrifugal pump, the pressure rise comes from the change of potential energy of the fluid in the centrifugal force field of the rotor [24] caused by the rotation of the impeller. Integration of the radial pressure gradient on the radial direction yields to the pressure rise ΔP through the impeller :

$$\Delta P = \rho \Delta h = \rho (r_2 \omega)^2 \Big[1 - \frac{u_2}{r\omega} tan\alpha \Big] \tag{5.1}$$

where r_2 is the radius of the pump, ω the angular velocity, u_2 the radial velocity at the exit of the pump, and α the exit swirl angle. The radius of the pump blades leading edge is r_1. For a preliminary design, it is reasonable to assume a value of 0.5 for the coefficient into brackets in Equation 5.1 [39]. This assumption is verified later by CFD calculations. All

the pressure rise should occur in the impeller since there is no diffuser. The rotor tip speed corresponding to the required pressure rise of 30 atm is $v = r_2\omega = 78m/s$.

Pump sizing

The sizing is a tradeoff between

- *Mechanical design* The pump must achieve a 30 atm pressure rise without cavitating. As stated before, the pressure rise requirement is equivalent to a pump rotor tip speed $r_2\omega$ of 78 m/s. The cavitation is a strong function of the centrifugal speed $r_1\omega$ at the pump leading edge. The functional design of the pump is then driven by the ratio r_2/r_1.

- *Fluid mechanics* The fluid is supplied axially, and enters the pump radially since there is no inducer. The fluid mechanics for the right-angle turn is governed by the radius r_1 and the blade height h. The axial tube area πr_1^2 must be at least of the same order as the pump inlet area $2\pi r_1 h$. The ratio r_1/h is the governing parameter and must be greater than 1. Second, the endwalls 3D effects scale with the inverse of the aspect ratio h/C where $C = r_2 - r_1$ is the chord of the blade. For this concern, it is preferable to have a high and short blades. A h/C smaller than 0.15 is not desirable.

- *Microfabrication limitations* The blade height for the microengine-related devices is 225 μm. Using the same height would permit use of a well-established fabrication process. Ayon and Protz [34] have demonstrated the ability to etch 400 μm blades. Yet, such advance feature aggravate the difficulty of rotor balance.

- *Bearings capability* On-going experiments prove that the bearings are a critical issue and a major technical challenge. Rotational speeds lower than a million rpm are desired to reduce technical risk.

The following radius, angular velocity and blade height have been adopted :

$$\begin{cases} r_1 = 250\mu m \\ r_2 = 1mm \\ \omega = 77,500rad/s \simeq 750,000rpm \\ h = 225\mu m \end{cases}$$

These dimensions reflect the previous requirements. Pennathur [31] suggests that the blades designed by Youngren with these dimensions and presented hereafter should not cavitate.

Power required

The power required to drive the pump at this rotating speed, for a mass flow $\dot{m}$, is

$$P_{pump} = \frac{1}{\eta_{pump}} \dot{m} \frac{\Delta P}{\rho} \tag{5.2}$$

The required power is calculated for a mass flow of 3.5g/s. Indeed, we expect a 30% loss in mass flow rate between the 2D design and the physical pump, because of 3D effects such as tip clearance flows [32]. Then, the shaft power required is

$$P_{pump} = 36W \tag{5.3}$$

Pump blade design

Harold Youngren designed the pump blades using a 2D CFD code (MISES) [44]. The design and the pressure coefficient distribution are shown in Figure 5-4.

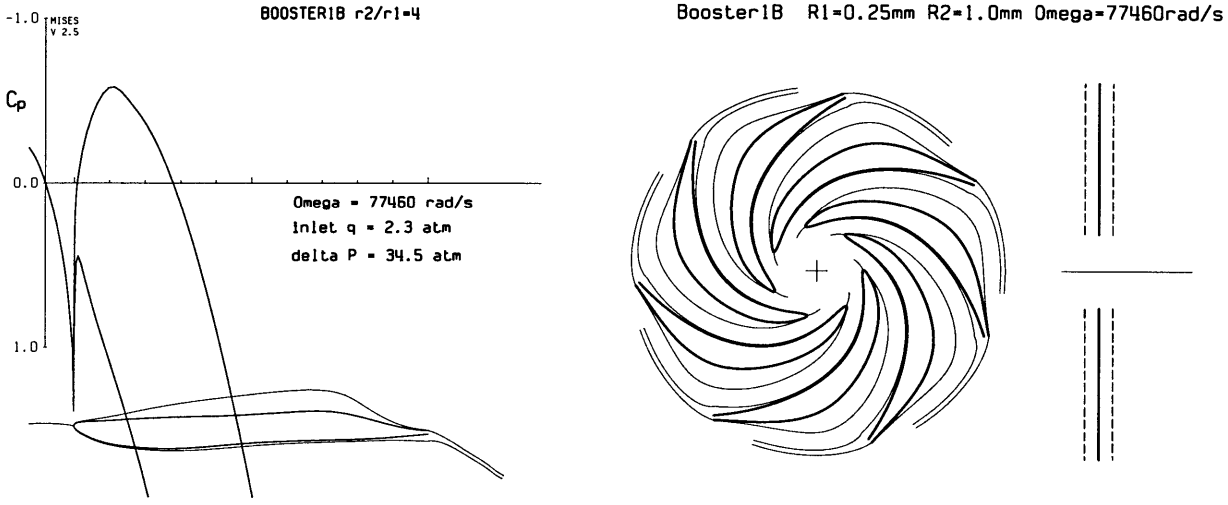

Figure 5-4: MISES pump design and C_p distribution

Pump CFD

CFD calculations on the pump blade design were performed by Jamonet [21] with Fluent, a commercial 3D Navier-Stokes solver. 2D simulations predicted a pump efficiency of 54% in

the laminar case, and 47 to 50% in the turbulent case (two turbulence models were used), and a pressure rise of 29 to 30 atm at a mass flow of 2.5 g/s. 3D simulations taking into account the turning of the flow and the tip-clearance predicted an efficiency of 47%, the losses implying a reduced pressure rise of 24.5 atm. Detailed results may be found in his thesis [21].

5.3.4 Turbine design

Assuming an efficiency of 30% for both turbine and pump, the power required by the pump is 36W . Some viscous losses occur in the bearings and in the back plenum -they are calculated in Section 5.4.5-, and a safety margin is required. The turbine is thus designed to produce roughly 50W of mechanical power.

Turbine blade sizing

The simple model of a radial inflow turbine with radial blades is used to perform a preliminary dimensioning. r_b is the radius of the trailing edge, and r_c is the radius of the leading edge. The ideal power obtained from this turbine is

$$P_{turb} = \dot{m}\omega(r_c v_c - r_b v_b) = \dot{m}\omega^2(r_c^2 - r_b^2) \tag{5.4}$$

To obtain an power of 50W, we can choose $r_c = 3mm$ and $r_b = 2.4mm$. This leading edge radius is consistent with the system design since it leaves a 1400 μm gap between the pump blades and the turbine blades. As detailed later, a bearing pad of 400 μm in width is adopted, allowing vaneless areas of 500 μm in width for the pump exit and the turbine inlet. These area dimensions are believed to be enough to allow the fluid right angle turn since the axial to radial area ratio is 2.8 and 2 for the pump and the turbine, respectively [11]. The trailing edge radius of 3mm is consistent with the programmatic requirements.

Turbine blade design

This preliminary solution was used as a baseline input in a 1D iterative model developed by Philippon [32]. This model assumes a 30% pump and turbine efficiency and a pressure loss coefficient (representing 3D losses) was imposed.

The required power is achieved with a turbine inlet pressure of 24 atm, and an exit pressure of 9 atm, for a rotor radius of 3 mm. These values were chosen since they are

considered a good match to the requirements. They lead to the desired mass flow and power, while being consistent with the system design where the difference between the pump exit pressure and the turbine inlet pressure is the loss in the cooling jacket. The most important inputs and outputs of the turbine design tool are summarized in Table 5.2.

Table 5.2: Turbine 1-D design results

NGV inlet radius	4.5 mm
NGV outlet radius	3.1 mm
NGV trailing edge angle	73.9 deg
Inlet total pressure	24 atm
Mass flow	2.5 g/s
Rotor rotational speed	750,000 rpm
Rotor leading edge radius	3 mm
Rotor trailing edge radius	2.4 mm
Stage exit static pressure	9 atm
Rotor inlet relative swirl	-79.5 deg
Rotor oulet relative angle	-68.8 deg
Total work extraction	50.2 W
Stage efficiency	30%

With these results, Youngren designed the turbine blades using MISES. The design of the nozzle guide vanes and of the turbine blades is shown in Figure 5-5 and in Figure 5-6.

5.3.5 Conclusion on turbomachinery blading

Blading of a microturbopump has been designed. This section summarizes that design. The pump outlet diameter is 1mm. The turbine inlet diameter is 3mm. Blade height for both is 225um. Tip clearances are 20 μm for both. The rotor is designed to rotate at a speed of 750,000 RPM, giving the turbine a peripheral speed of 225 m/s. At this design speed, the pump produces a pressure rise of 30 atm for a mass flow of 2.5 g/s. Assuming an efficiency of 30% for both turbine and pump, the power required by the pump is 36W . The turbine is designed to produce roughly 50W of mechanical power, to overcome the mechanical losses inherent to the system . The required power is achieved with a turbine inlet pressure of 24 atm, and an exit pressure of 9 atm.

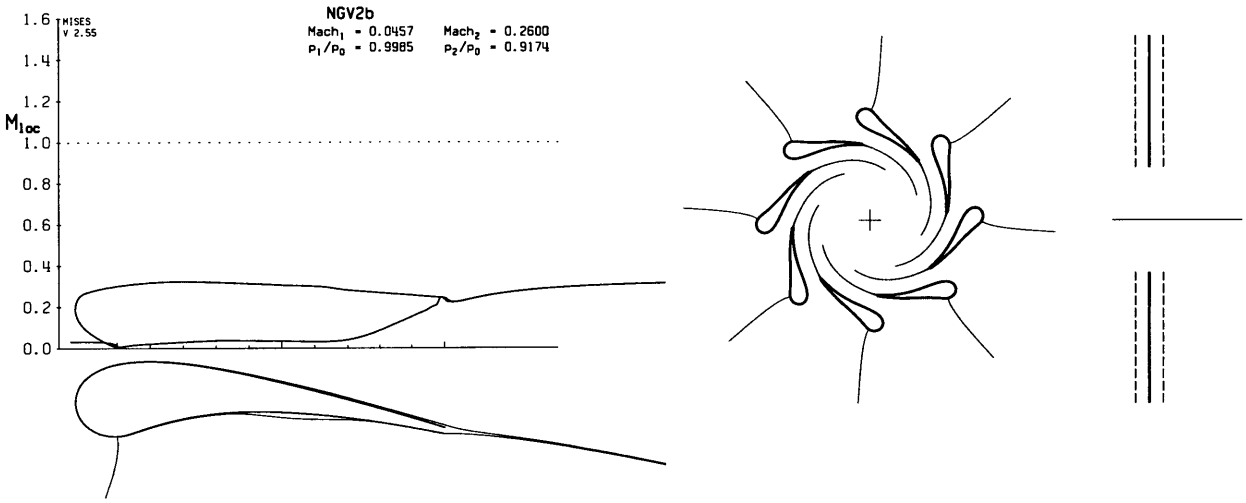

Figure 5-5: MISES nozzle guide vanes design and Mach number distribution. Symbols are defined in the nomenclature.

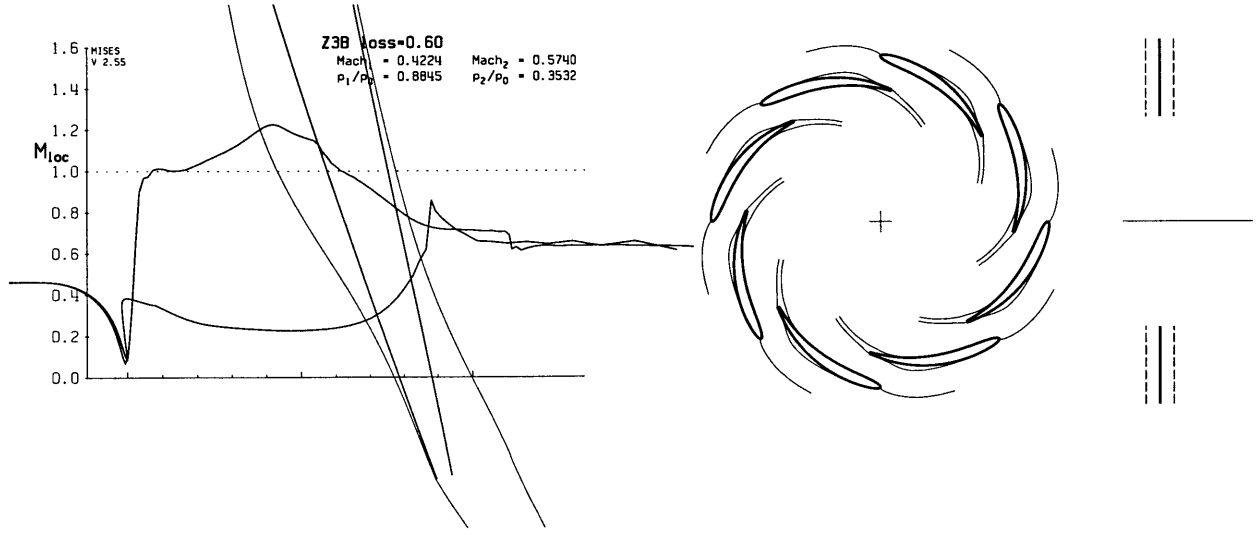

Figure 5-6: MISES turbine design and Mach number distribution. Symbols are defined in the nomenclature.

5.3.6 Piping and pressure losses

The design options were constrained to current microfabrication capabilities. Features are formed by assembly of two-dimensional features. The piping in the die thus includes right angle turns, and also the desire to avoid multilayer etches results in high-aspect ratio piping flow channels. These features engender pressure losses, which can impact system efficiency.

Calculations were performed by Jamonet [21] on the piping geometry to determine the pressures level at the turbine inlet (from the inlet of the die to the NGV inlet), the turbine exit, the pump inlet and exit. He used an empirical model of flow resistance developed by Fried and detailed in [14]. This model estimates the pressure drop in each connection, elbow, or round pipe. The results are presented in Table 5.3 for the initial design, the improved design (explained hereafter). The regions are referred to as turbine inlet or exit, and pump inlet or exit, and are presented on Figure 5-7. A incompressible model is used for water. Isothermal and adiabatic models were used for the air paths. Results are given in absolute losses (in Pa) and as a fraction of the total pressure drop (for the turbine) or pressure

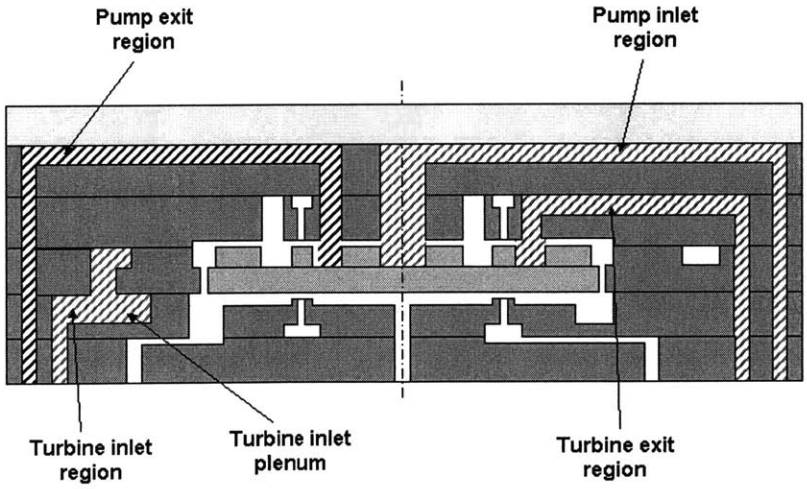

Figure 5-7: Cross section of the turbopump concept. Definition of the regions for piping losses.

As can be seen, calculations showed that these pressure losses were not large (3%) for the pump inlet and exit. However, losses are higher for the turbine where high Mach numbers are required due to the low density fluid.

	Initial design		Improved design	
Turbine Inlet - Isothermal model	149396 Pa	9.96%	36709 Pa	2.45%
Turbine Exit - Isothermal model	242210 Pa	16.15%	116371 Pa	7.76%
Turbine Inlet - Adiabatic model	370503 Pa	24.7%	91039 Pa	6.07%
Turbine Exit - Adiabatic model	453608 Pa	30.24%	217938 Pa	14.53%
Pump Inlet	88329 Pa	3.15%	76801 Pa	2.74%
Pump Exit	9524 Pa	0.34%	9904 Pa	0.35%

Table 5.3: Pressure losses in the turbopump at flow rates of 2.5 g/s

The initial design featured the turbine inlet and exit in the same layer, and had high losses. The piping and plena layout were then redesigned for maximum flow area. As can be seen from Figure 5-7, the turbine inlet plenum is in wafer 4 [1] , and some solutions have been included to lower the losses in the right angle turns. This arrangement can be seen in Figure 5-2, which presents the improved design. This yields an acceptable loss level for a turbopump.

5.4 Bearing Design and Rotor Dynamics

5.4.1 Introduction

The rotor requires axial and radial support. To simplify the design and reduce technical risk, hydrostatic thrust and journal gas bearings are used. The performance of such designs has been demonstrated in the micro bearing rig. Unlike the previous work, however, the thrust bearings on an annular pad, rather than a center pad. The bearing also serves as a seal between the pump and the turbine. The aft thrust bearing is of annular geometry as well, but the annular pad is part of the stator, unlike the forward thrust bearing where this feature is etched into the rotor. Thrust bearings can support an axial load on the rotor, but it is preferable to have an axially balanced rotor (i.e., no load is presented to the

[1] A trivial solution for this plenum would be to place it in wafer 3, directly around the guide vanes. This approach is not adopted. Some extra features would have to be added between the plenum and the guide vanes. Indeed, the pressure drop that occurs in the injectors from the turbine inlet plenum to the guide vanes (between wafers 3 and 4 in the current design) is desirable to improve uniformity of the flow on the turbine blades.

thrust bearings at the design point). For this reason, we choose to control the pressure in the rear plenum (inside the aft thrust bearing) to balance high pressures on the front side of the rotor. A pipe enters this plenum or thrust bearing piston, where pressurization or ventilation will be provided, with independent control of the pressure. The depth of this plenum (50 μm) is chosen to reduce drag on the rear of the rotor.

5.4.2 Axial balance

Figure 5-8 shows the pressures on the front side of the rotor at full design speed. Integration of this pressure yields a load on the rotor front side of 38N. To relieve the thrust bearings from the need to support this load, a balance force is needed. This is implemented by connecting the aft plenum to an external pressure source. The back plenum is hatched on Figure 5-8.

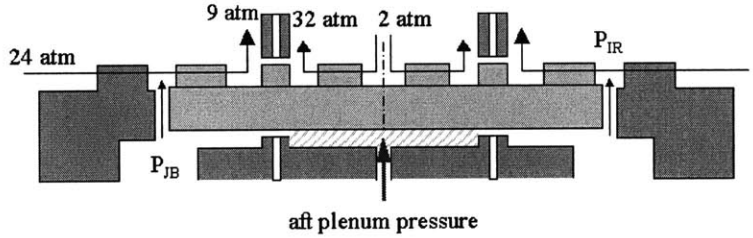

Figure 5-8: Pressures on the front side of the rotor and back plenum. The pressures indicated are the design pressures for, respectively, the turbine inlet, the turbine exit, the pump exit, the pump inlet.

We will now describe a detailed axial balance model. The thrust bearing forces are not considered, since equilibrium without them is wished. The model takes into account the pressure distribution on the front side (assuming linear pressure distributions through the pump and turbine blades), flow turning at the pump inlet and exit, and at the turbine exit (momentum is transferred to the rotor when the flow makes a right angle turn). For the pump exit turning, integration of the momentum equation leads to a force $\vec{F}$ on the rotor. Its direction is forward and its value is

$$F = \frac{\dot{m}^2}{\rho_{water}\pi(r_{TBi} - r_{Po})} \tag{5.5}$$

Similar formulas apply to the pump inlet and the turbine exit.

On the back side of the rotor, the aft plenum pressure applies inside the thrust bearing inside radius r_{TBi}, and the journal bearing pressure applies outside the thrust bearing outside radius r_{TBo}. The required journal bearing pressure calculation is performed in Section 5.4.4.

Viscous drag on the journal bearing wall is accounted for in the axial forces. It is shown that this force, as well as the forces resulting from the turning of the flow, are negligible compared to the pressure forces.

Three design points were considered. Pump and turbine performance were calculated for three speeds: the design speed 750,000 rpm, and lower speeds, 190,000 rpm and 50,000 rpm. For each point, the axial forces were computed, and the back plenum pressure necessary for axial balance was calculated. Results are presented in Table 5.4.

Rotor speed	750,000 rpm	190,000 rpm	50,000 rpm
Pump pressure rise for $\dot{m}$=2.5g/s	30 atm	2 atm	0.137 atm
Pumping power required	36W	2.33W	0.16W
Turbine inlet pressure	24 atm	2.5 atm	1.15 atm
Turbine exit pressure	9 atm	1.5 atm	1 atm
Turbine mass flow rate	2.5 g/s	0.42 g/s	0.078 g/s
Turbine power delivered	50W	3.82W	0.24 W
Pressure force on the forward side of the rotor	38 N	5 N	2.7 N
Aft plenum pressure needed for axial balance	10 atm	1.7 atm	1 atm

Table 5.4: Pressure required in the aft plenum for axial balance at three speeds

5.4.3 Thrust bearings

Axial support is provided by a pair of gas thrust bearings. As described above, they consist of gaps that sit above 400μm wide annular hubs (from 1.5 to 1.9mm from the center of the rotor).A parametric analysis was performed, where the driving factors were, as explained in Section 2.2:

- the stiffness for an axial eccentricity $\epsilon = 0$,
- the load for an axial eccentricity $\epsilon = 0.4$.

Model

Each bearing is formed by a number of capillaries fed by a plenum that sits above them. The fluid flows in these capillaries or nozzles, and then turns both radially inward towards the pump exit, and radially outwards towards the turbine exit, as shown in Figure 5-9. An electric analogy similar to the one presented in Section 2-1 is used to compute the pressure distribution on the rotor pad. Since the mass flow is split into two parts, we have now two variable resistances in parallel.

The pressures are different on both sides of the forward thrust bearing. The pressure on the pump exit side is 32 atm, whereas the pressure on the turbine exit side is 9 atm. To simplify the model, we assume that all the forward thrust bearing flow exits on the turbine side. This gives the pressure distribution presented on Figure 5-9. The pressure profile between the nozzle exit and the pump exit area is considered linear. The pressure profile between the nozzle exit and the turbine exit area has a log shape, it corresponds to a radially diverging flow.

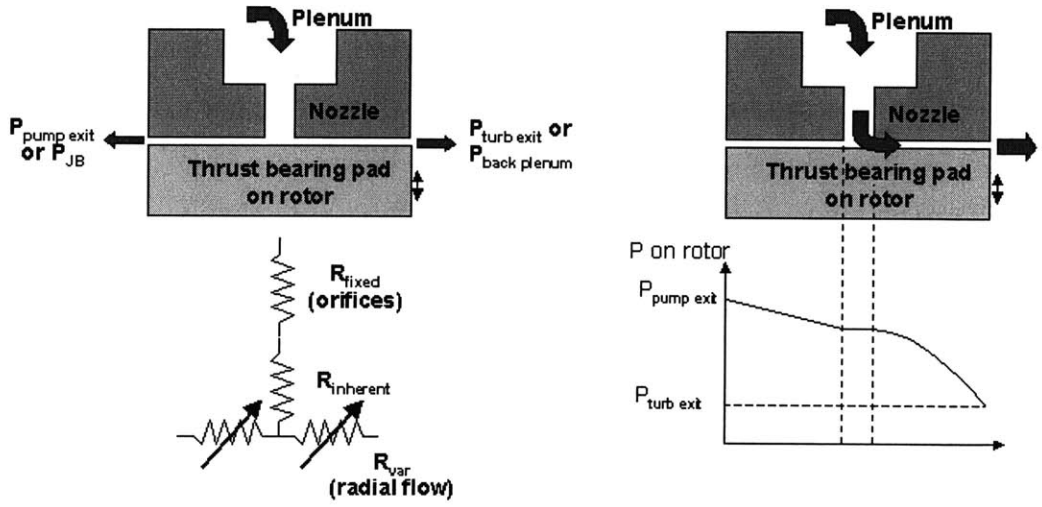

Figure 5-9: Thrust bearing flow and resistances model. Simplified configuration and associated pressure distribution for the forward thrust bearing.

Parametric design

The pressure distribution on the thrust bearing pad described above was analytically integrated to compute the force, and the thrust bearing model was run to compute the stiffness

and the load over a range of eccentricity, nozzle diameter, nozzle length, gap, pressure, number of nozzles. These parametric design calculations were performed for the design speed pressures, and for the lower speed 190,000 rpm. Results are presented in Appendix E. As will be seen, the stiffness and the load do not follow the same trends with speed. The nozzle diameter and length, the gap and the number of orifices were chosen to maximize the stiffness for $\epsilon = 0$ and the load for $\epsilon = 0.4$. Trade-offs between the two operating speeds have to be realized.

Results

Each bearing is formed by a 2.5 μm tall gap pressurized by sixty 12 μm diameter, 100 μm deep restrictor nozzles located at a radius of 1.7 mm. The model shows that for a thrust bearing pressure (in the plenum feeding the restrictors) of 40 atm, a stiffness of 3.6 N/μm is achieved for zero eccentricity (rotor centered vertically, full speed parameters). This stiffness should be sufficient if the back plenum pressurization is accurate and reliable, considering the pressure load on the rotor (38N) [20].

The forward thrust bearing acts as a seal between the pump exit and the turbine exit because of its small gap (2.5 μm) and the high pressure imposed in this gap. An efficient seal is required because of the large pressure difference (30 atm on the pump side, 9atm on the turbine side). The aft thrust bearing acts as a seal between the back plenum and the journal bearing plenum.

5.4.4 Journal bearing

An annular journal bearing supports the rotor in the radial direction. It is 300 μm deep, and 12 μm wide. The gap is pressurized by a plenum that sits below both the rotor and the stator. Rotational speeds up to 6 times the natural frequency of the bearing have been demonstrated with this arrangement. For this geometry, the natural frequency is predicted to be about 2,500 Hz for a dP of 10 psi[2], assuming a discharge coefficient of 0.4 to 0.7. The natural frequency vs. dP is shown in Figure 5-10. This result was obtained with a compressible model developed by Breuer, and based on boundary layer growth. It should allow rotational speeds of 750,000 rpm.

[2]dp is the axial pressure differential across the journal bearing gap

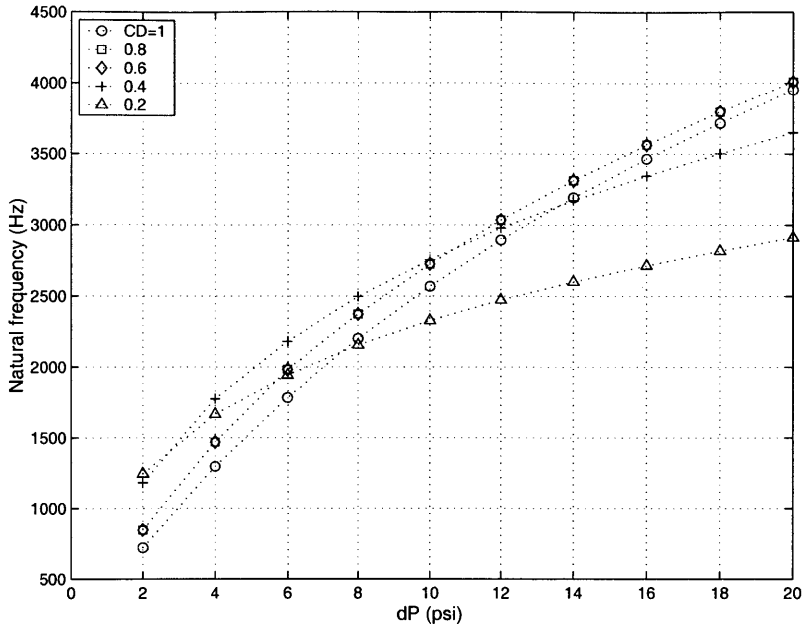

Figure 5-10: Turbopump gas journal bearing natural frequency

5.4.5 Drag

The combination of small gaps and high rotating speeds result in highly sheared flows, and large viscous dissipation. In the turbopump, drag comes from the tangential flow in the journal bearing gap, in the thrust bearing gaps, and in the back plenum. In these areas, the flow is dominated by viscous effects, and can be represented by Couette flow. The calculation of the power dissipated is similar to the calculation performed for the liquid micro-bearing in Section 2.4.3 and is not repeated here. The results are presented in Figure 5-11. The back plenum depth is designed so that the dissipation in this plenum is only a small fraction of the total dissipation. This depth is chosen to be 50 μm.

As can be seen, the total power dissipated is 1.13W at full speed. It represents 2.3% of the turbine power and is thus acceptable.

If the thrust and journal bearings were *liquid bearings* and the back plenum was liquid as well, then without any geometric change, the dissipation power was calculated. It is found that at full speed, this power is larger than 115W, i.e. 2.3 times larger than the power delivered to the system by the turbine. This result shows that if liquid bearings were to be implemented in a future MEMS turbopump, a different bearing configuration would be needed, with emphasis given on drag reduction.

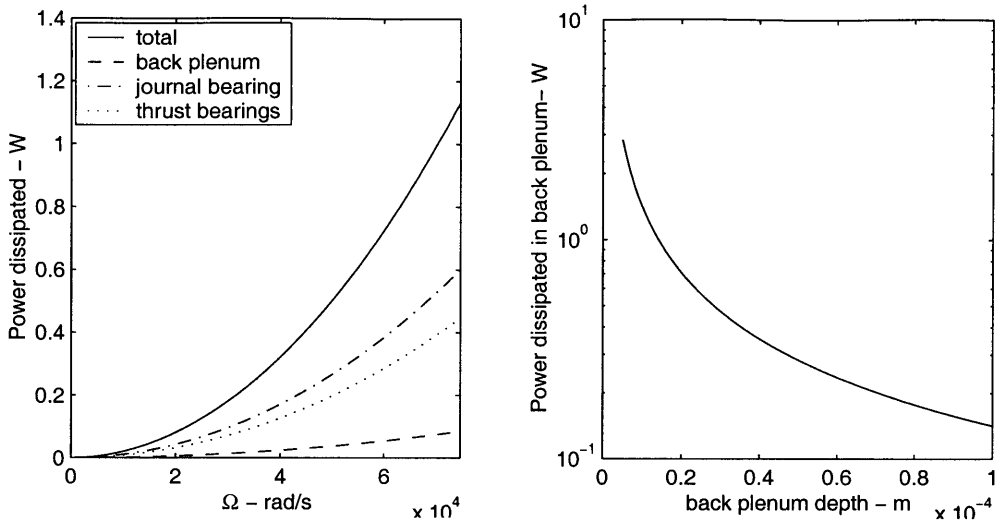

Figure 5-11: Turbopump drag versus speed. Drag occuring in the back plenum for design speed versus depth of the plenum

5.5 Experimental requirements

5.5.1 Fluidic connections

The design is constrained by the need to package and instrument the device for testing. Fluid connections are made with o-rings. All connections are on the aft side. There are seven 2mm diameter interconnects and nine 0.9 mm diameter interconnects. All interconnects are spaced 4 mm apart on a 16 mm square. Sealed connections are ensured with Buna-Nitrile o-rings (0.078 in. dia x 0.016 in. width and 0.035 in. dia x 0.016 in. width) from Apple Rubber. Calculations performed by Jamonet showed that compression stemming from a central inlet o-ring would deflect the silicon plates so as to close the thrust bearing gap, constraining rotor dynamics [21]. A design with o-rings only on the periphery was therefore required. A brass/aluminum package will be built.

5.5.2 Performance measurements

Performance measurements are required during testing. Thus, speed bumps were placed on the rotor to measure the rotating speed. An optic fiber coupled through a lens (to increase the stand-off distance), pointing at these four bumps through the pump exit (and through the glass wafer) allows measurement of the rotor rotation and whirl [10]. This system is described in Section 3.3.

Pressure taps allow precise static pressure measurements, without the need to estimate the losses that occur in the die and in the packaging. These taps are available for the pump exit, the turbine inlet and exit, the turbine inter-row pressure, and the journal bearing pressure.

Finally, the top glass wafer allows viewing of the pump exit and the blade trailing edges to observe the any cavitation occurring. A 'window' was also etched though the wafers 1 and 2 in order to observe the turbine inlet to estimate the water leak through the thrust bearings.

5.5.3 Structural integrity

The pyrex plate must withstand the pressure at the pump exit plenum that sits on top of wafer 1. Calculation performed by Jamonet shows that the minimum thickness of the pyrex plate must be 430 μm to ensure structural integrity [21]. A thickness of 500 μm was chosen.

Several layers contain concentric plenum that have to be close to each other. The most stringent case is wafer 2 where the pump inlet plenum, the pump exit plenum, the forward thrust bearing plenum and the turbine exit plenum are concentric. The minimal wall section needed to ensure integrity at the design pressure is 100 μm [30]. A conservative value of 200 μm as the smallest wall section was adopted.

5.6 Fabrication requirements

As stated earlier, MEMS fabrication technology is a strong constraint on the design. Three-dimensional features are formed by assembling two-dimensional shapes. Nested masks allow a limited number of steps on a single wafer. The smallest feature size is constrained to an aspect ratio of 30:1, and the mask fabrication technology sets the ratio of die size to minimum feature size.

The fabrication process was designed by Peles, based on the micro bearing rig process. This process in not detailed here. A set of masks was created. A mask is a glass plate on which the desired features are defined by a chrome pattern. The wafers are coated with a layer of photoresist. Exposure of the wafer with UV light weakens the photoresist, which is developed chemically to transfer the pattern of the mask to the wafer. The specific process to do the etching for this work is deep reactive ion etching (DRIE). Finally, nested masks

are used to allow two different etch depths on a given side os a wafer (see London [26] and Ayon [2] for details).

The anodic bonding of the pyrex wafer is performed at the die level. It is necessary to set the top wafer to a specified potential when bonding to the pyrex wafer. Thus, a 2mm diameter hole is etched in wafers 2 to 5 to provide electrical access to the top wafer.

5.6.1 Masks creation

14 masks are necessary for the turbopump fabrication. They are presented in Appendix F. The etching quality and uniformity is dependent on the amount of silicon that is etched. Features such as the journal bearing gap and the thrust bearing nozzles are critical to the system functionality, and are etched during the same step as larger size features. In this case, haloes are used. The large-size features are removed after etching a ring around them, which considerably reduces the amount of silicon etched, and enhances the etch quality of critical features. This approach is feasible only for through etches (i.e, when a feature is etched on both sides of a wafer). Thus, it was not possible to implement haloes etch in the wafer 4, where the large-scale turbine inlet plenum (that are not etched through) might interfere with the aft thrust bearing nozzles. Haloes are used for the aft sides of wafers 2 and 3. The haloes were dimensioned by Peles depending on the size of the critical features, their proximity to larger scale features, and the impact on the process of non-uniform features break through. Thus, the journal bearing etch at the back of wafer 3 is done while wafer 2 and 3 are bonded together. A number of holes connect the turbine inlet plenum to the turbine inlet area. The non-uniform break through of these holes allows the plasma to etch the thin membrane of wafer 2. These holes have then mixed haloes of 4 and 12 μm so that the parts of them that face the thin membrane etch through last.

5.6.2 Wafer layout

The die is a 21 mm square. Nine dies could fit on one stack of four inch wafers. However, it was observed on microengine related devices that the etch uniformity decrease with the number of dies on a wafer. A non uniform DRIE blade etch can shift the center of mass from the geometric center, imbalancing the rotor. For proper turbopump operation, the maximum non-uniformity across the rotor should not exceed 1 μm. Non-uniformity is defined as the maximum vertical distance between two points across a die. A series of blade

die spacing etch tests was performed by Peles [30]. He showed that wafers with four and five dies met the requirement (the non-uniformity is 0.9 μm for the 4-dies wafer, and 1.1 and 1.3 μm for the center die and outer dies respectively on the 5-dies wafer).

Based on these results, the wafer layout presented in Figure 5-12 was chosen. This configuration allows a maximum separation between the five dies on the wafer.

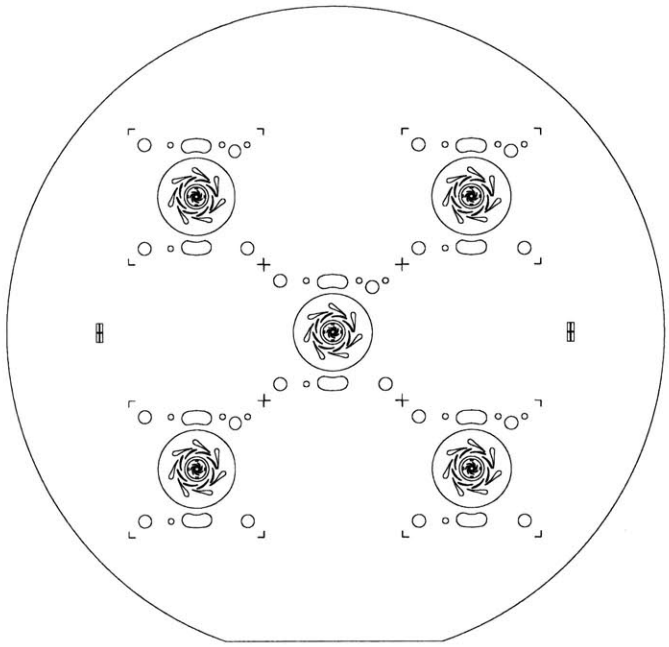

Figure 5-12: Layout of the wafer. The mask illustrated corresponds to the front of wafer 3 (rotor). The boundaries are defined but the polarity is not shown.

5.7 Layout

The device consists of five silicon wafers, and one pyrex wafer, which is anodically bonded to the silicon stack. This section presents the arrangement of the non-trivial wafers.

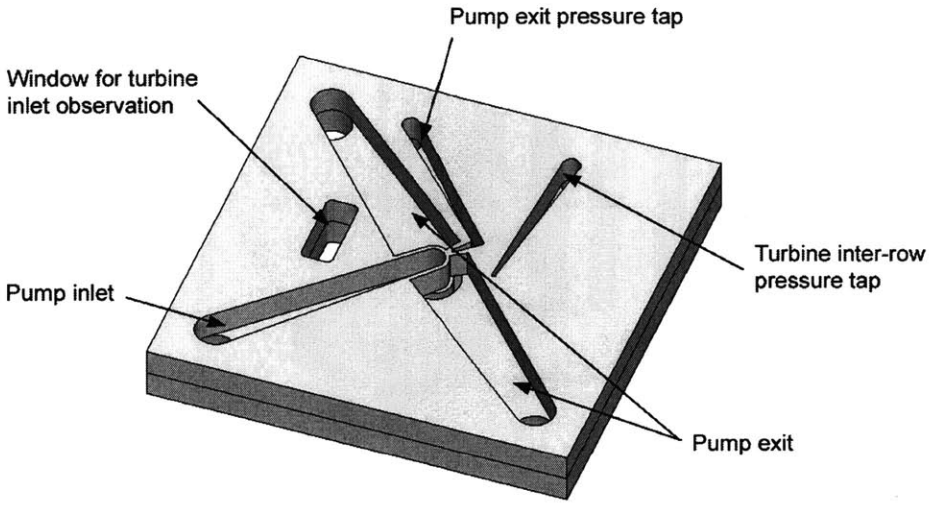

Figure 5-13: Layout of turbopump wafer 1

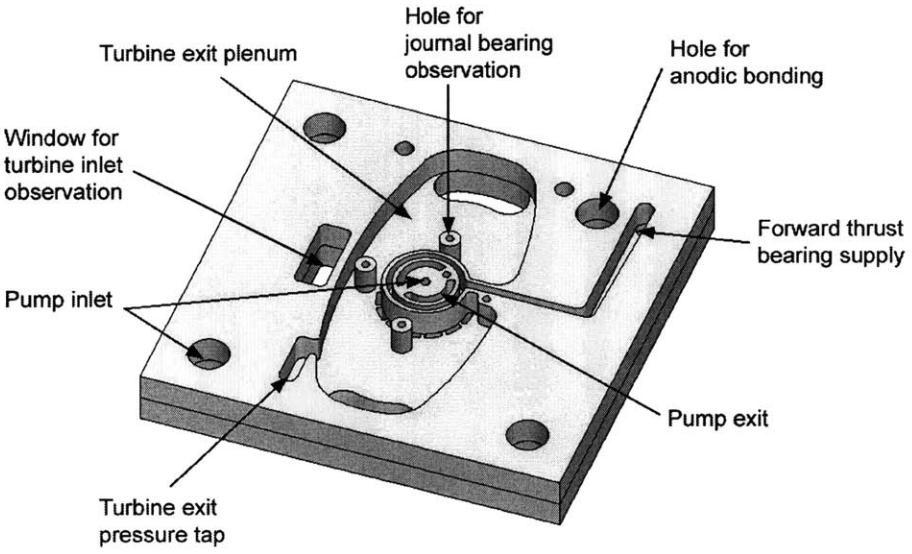

Figure 5-14: Layout of turbopump wafer 2

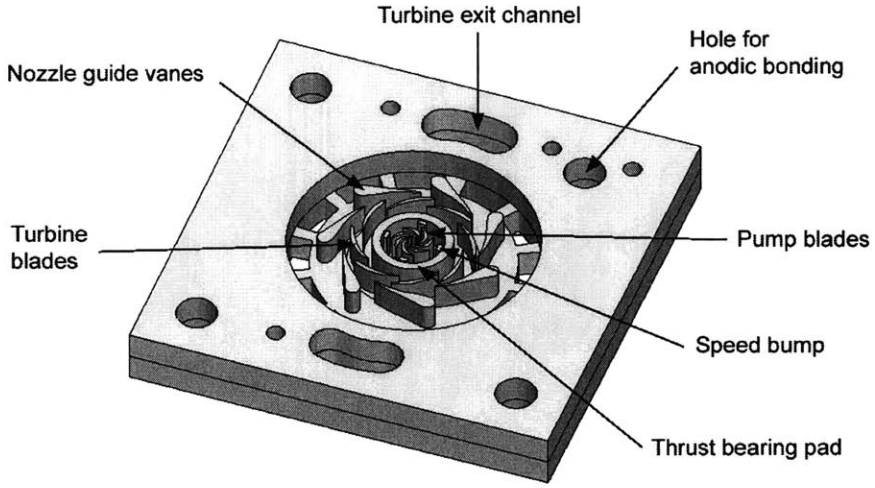

Figure 5-15: Layout of turbopump wafer 3

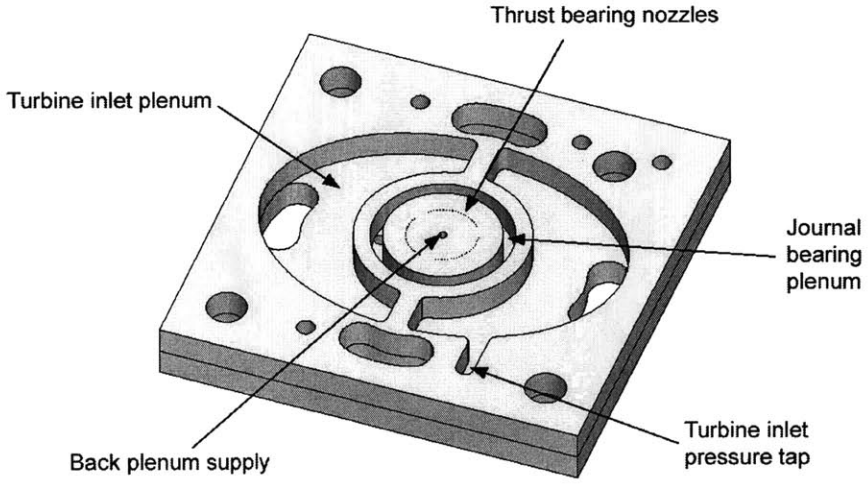

Figure 5-16: Layout of turbopump wafer 4

5.8 Fabrication results and cross-sections

The first built of the demo turbopump was fabricated by Peles. This section presents some pictures of the wafers before the bonding process, a cross section from a completed and die-sawed die, and a picture of the completed device after anodic bonding.

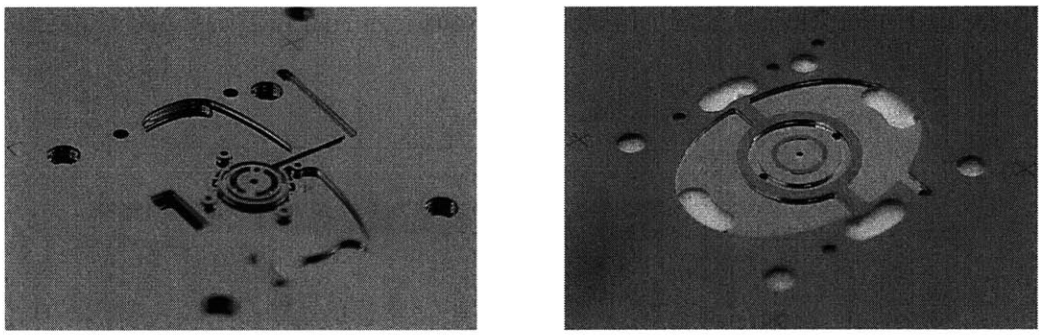

Figure 5-17: Die-level images of turbopump wafers 2 (left - turbine exit plenum) and 4 (right - turbine inlet plenum). Images courtesy of Yoav Peles.

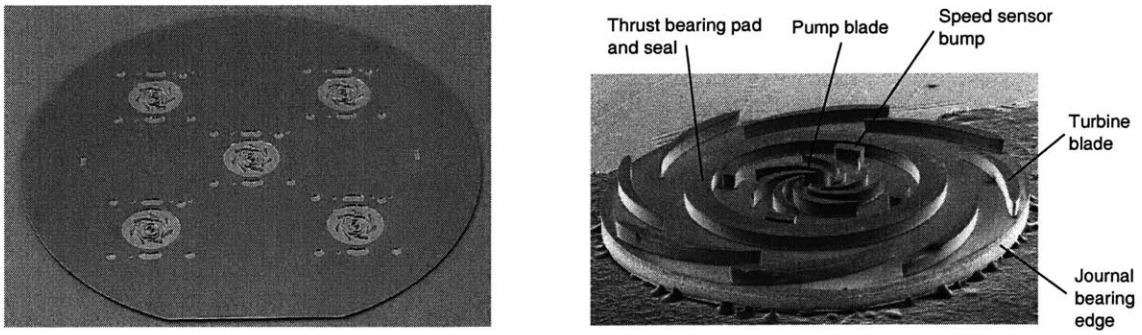

Figure 5-18: Left : wafer-level image of turbopump rotor wafer. Image courtesy of Yoav Peles. Right : SEM picture of turbopump rotor.

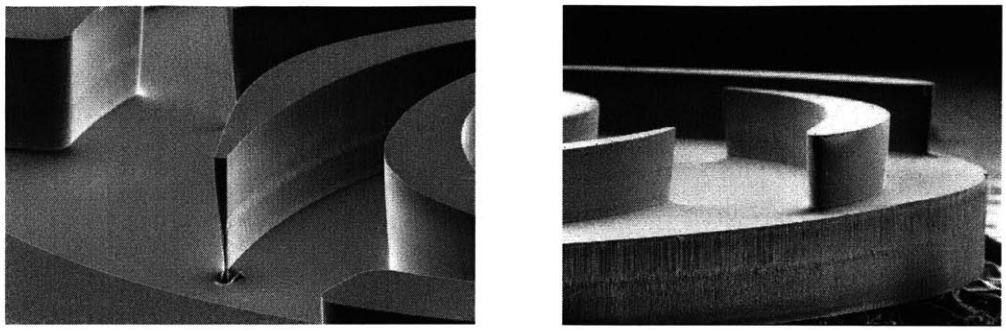

Figure 5-19: Close-up images of the turbopump rotor showing the pump blades trailing edge (left) and the turbine blade leading edge and the journal bearing edge (right).

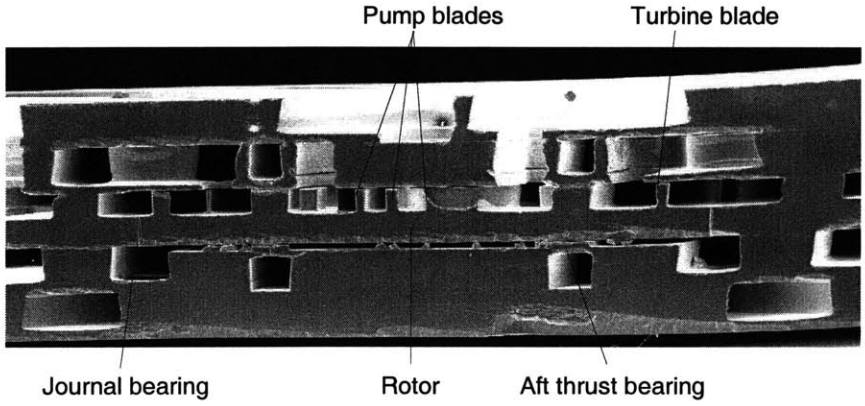

Figure 5-20: Cross-sectioned die

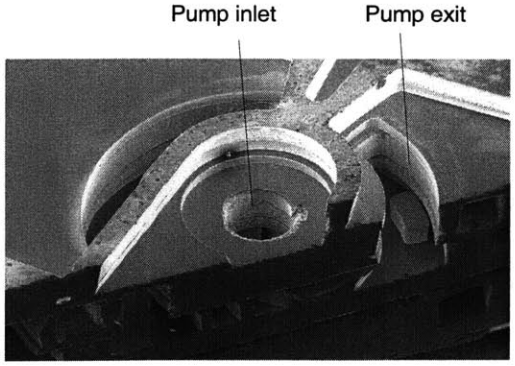

Figure 5-21: Top view of a cross-sectioned die, showing the water flow paths.

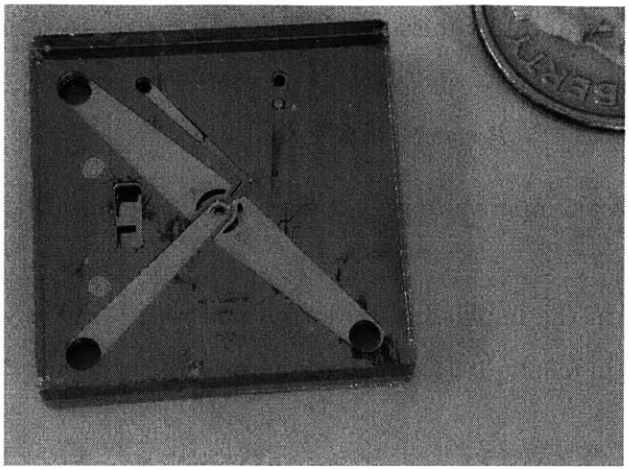

Figure 5-22: Bonded, die-sawed and pyrex anodically bonded turbopump die.

5.9 Alternative pump design

The pump designed in Section 5.3 has a large exit swirl flow angle, resulting in significant backsweep. This is to control the effective passage area to avoid flow separation [44]. This conservative design (in terms of separation and cavitation) requires high rotor speed. At the same time, the turbine stage has a large degree of reaction R=0.69, implying it is very lightly loaded, i.e. is asked to deliver relatively little power for its speed; reducing the turbine reaction would yield larger power.

An alternative pump with reduced backsweep was designed, which requires lower rotor mechanical speed. This is a risk reduction strategy should rotor dynamics prove troublesome.

5.10 Baseline design of the main rocket engine turbopump

A baseline design of the main rocket engine turbopump system is proposed in this section. The pump and turbine are investigated using simple 1D models. The fluid considered is hydrogen peroxide, since it could be the oxidizer in the rocket engine.

5.10.1 Pump design

The main pump of the rocket engine must deliver propellant at a pressure of 300atm. The demo turbopump assumes room temperature fluid at the turbine inlet. The main pump uses cooling jacket exit fluid which is at an elevated temperature. The power delivered by

a turbine where the inlet total temperature is T_{Tin} and the pressure ratio is π, assuming an isentropic passage, is

$$Power = \dot{m} C_p T_{Tin} \eta \left(1 - \pi^{\frac{\gamma-1}{\gamma}}\right) \tag{5.6}$$

As a result, as the inlet temperature rises, the pressure ratio drops at constant power.

The pressure rise in the impeller of radius r_P and rotating at a velocity ω is, with the same assumptions as in 5.3.3,

$$\Delta P = \frac{\rho}{2}(r_P \omega)^2 \tag{5.7}$$

We assume a configuration where a boost pump similar to the demonstration pump is in series with the main pump, pressurizing the inlet to inhibit cavitation. The fluid thus enters the main pump at 30atm and room temperature. The density of hydrogen peroxide under these conditions is 1431 kg/m^3 [23]. The required ΔP is 270 atm, which means that $r \times \omega \sim 1.867.10^6 mm.rpm$ is needed.

The following radius and angular velocity are valid solutions, depending on internal (cavitation, blade design feasibility) or external (system integration, bearing design) requirements :

$$\begin{cases} r_P = 1mm & and \quad \omega = 1.87 \times 10^6 rpm \\ r_P = 2mm & and \quad \omega = 933,630 rpm \\ r_P = 3mm & and \quad \omega = 622,420 rpm \end{cases}$$

The design mass flow for the rocket is $\dot{m} = 2.5$ g/s. Assuming an efficiency of 30%, the power required to drive this pump is

$$P_{pump} = \frac{1}{\eta_{pump}} \dot{m} \frac{\Delta P}{\rho} = 160W \tag{5.8}$$

5.10.2 Turbine design

A turbine delivering 200 W of power was designed[3]. It is consistent with the rocket engine system in which the turbine is driven by fluid exiting the cooling jacket at a pressure P_{turb_in} of 250 atm and at a temperature of approximately 1000 K. After exiting the turbine, the fluid enters the combustion chamber injectors. The pressure at the turbine exit should be

[3]Besides driving the pump, the turbine must also overcome the viscous losses in the bearings and in the plenum in contact with the rotor.

130 atm or larger for combustion stability [33].

The hydrogen peroxide is considered in a gaseous phase. Heat capacity data are available from [23]. At a temperature of 1000 K, we have $C_p \simeq 1200 J/Kg.K$. No density, gamma, or heat capacity at constant volume data are available in the literature at these conditions. Density is approximated by the perfect gas equations, and the ratio of specific heats is approximated as $\gamma = C_p/(C_p - R)$, which is correct only for perfect gases.

A baseline turbine design is obtained with a spreadsheet by matching the temperature ratios across the turbine τ_t.

On the one hand, the power delivered by the turbine is

$$Power = \dot{m} C_p T_{Tin} \eta \left(1 - \pi^{\frac{\gamma-1}{\gamma}}\right) \tag{5.9}$$

The stage efficiency η is assumed to be 0.5 [32].

On the other, considering the turbine geometry and degree of reaction yields, from [24],

$$1 - \tau_t = \frac{(\gamma - 1) M_T^2}{1 + \frac{1}{2}(\gamma - 1) M_b^2} 2(1 - R) \tag{5.10}$$

The tangential Mach number M_T is calculated from the geometry and angular velocity v_t

$$M_T = \frac{v_t}{c} = \frac{r\omega}{\sqrt{\gamma r T}} \tag{5.11}$$

The total Mach number leaving the nozzles vanes M_b is calculated from the degree of reaction R and the inlet absolute swirl angle β_b [24]

$$M_b = \frac{2 M_T (1 - R)}{\sin \beta_b} \tag{5.12}$$

The resulting configuration yields a larger mass flow than imposed by the system. Thus, it is necessary to increase the blockage in the guide vanes. A solution compatible with the manufacturing technology is a partial admission turbine. Indeed, the radial velocity at the turbine inlet is $v_r = M_b c \cos \beta_b$, and gives a mass flow rate $\dot{m} = 16.3 g/s$ for a blade height of 225 μm. A 85% blockage in the guide vanes is necessary to obtain the desired mass flow rate 2.5 g/s.

The turbine design results are summarized in Table 5.5. They are consistent with a configuration identical to the demo turbopump, with co-planar and annular pump and turbine. The pump radius is 2 mm and the rotating speed is 933,630 rpm.

Table 5.5: Main turbine baseline design results

Turbine geometry		**Flow characteristics**	
NGV inlet radius	5.5 mm	Fluid	H_2O_2
NGV outlet radius	4.3 mm	Mass flow	2.5 g/s
NGV trailing edge angle	80 deg	Inlet pressure	250 atm
Rotor rotational speed	933,630 rpm	Stage exit pressure	134 atm
Rotor leading edge radius	4.2 mm	Total inlet temperature	1000 K
Total work extraction	200 W	Turbine temperature ratio τ_t	0.93
Stage efficiency	50%	Heat capacity C_p	1200 J/kg.K
Stage reaction	0.75	Inlet density	77.7 kg/m^3
NGV blockage	85%	Heat capacities ratio γ	1.3

5.10.3 Conclusion

A baseline design for the rocket main turbopump was performed. A partial admission turbine producing 200 W of power drives a pump that produces a 270 atm pressure rise. The turbopump layout is identical to the demo turbopump. Blades design must be performed. This design must be investigated with CFD tools to predict the performance of the non-conventional, partial admission. Finally, bearings design and rotor dynamics analysis must be performed.

The turbine was designed considering the fluid is gas. However, at the pressure and temperature involved, the hydrogen peroxide is supercritical. Indeed, the critical conditions are a pressure of 214 atm and a temperature of 457 degrees Celsius. The fluid behavior is then likely to be different. However, no data exist in the literature on supercritical hydrogen peroxide. One would expect a higher heat capacity, and lower density and viscosity [23].

Chapter 6

Summary and Conclusions

This thesis describes the design of a MEMS water turbopump, and analysis of and experiments with liquid micro bearings. This chapter presents a summary of the research discussed in this thesis, describes the contributions of this research, and makes recommendations for future work in this area.

6.1 Summary

The concept of power MEMS, and more specifically the microfabricated rocket engine in development at MIT, has been reviewed. This device, made from silicon, will integrate a thrust chamber, valves, and turbopumps into a single chip.

Liquid bearing are one attractive choice for the rocket turbopumps. The performance of these bearings has been modelled. Both thrust and journal bearings have been addressed. Performance prediction of an existing device, the micro-bearing rig, in a liquid environment, has been performed.

A test apparatus has been constructed to test liquid micro-bearings. Packaging, a test rig, and a data acquisition system were setup.

As an initial validation of the liquid micro bearings concept, the micro bearing rig designed for gas was run using water bearings and a water turbine. Bearings performance was analyzed, and spin tests were performed up to a speed of 21,000 rpm. This performance matched the analytical predictions.

A micro-scale turbopump producing a pressure rise of 30 atm for water was designed, as a demonstration of this concept for fluid pressurization in the rocket system. The functional

requirements and design constraints were defined. The design of the rotating turbomachinery and the hydrostatic gas-bearing system was performed. Innovative layout led to a single-wafer rotor designed for a speed of 750,000 RPM.

6.2 Contributions

The contributions of this work may be summarized as follows:

1. *The design of a demonstration MEMS turbopump* - Specifically, an innovative scheme with concentric, planar pump and turbine was proposed. Simplicity and ease of fabrication and testing were privileged over performance. Detailed design of hydrostatic gas bearings and turbomachinery was performed.

2. *The experimental demonstration of a non-intrusive speed sensor* - A optic method was designed to increase the standoff of the optic fiber used as a speed sensor. The whole system is exterior to the packaging. This method was successfully implemented for the liquid bearings experiment.

3. *The development of a methodology for liquid bearings design* - Models have been developed to predict the performance of liquid bearings.

4. *The experimental demonstration of liquid bearings at micro-scale* - The micro-bearing rig was successfully operated in a water environment, proving the effectiveness of water micro-scale bearings.

6.3 Future work

The recommendations for future work in this area are as follows:

1. *Turbopump experiments* - Preliminary static experiments should be used as an assessment of the fabrication process. By comparison with the flow predictions, one can deduce the critical nozzles and gaps dimensions. Thrust bearing stiffness can be verified by axial position tests. Gas spin tests should establish the journal bearing performance. Then, pumping experiments on a gas/liquid high pressure rig should be performed to deduce the overall pressure rise and turbomachinery efficiency, the

cavitation limits, the leak rate through the thrust bearing pad. These data should be compared to models and CFD predictions.

2. *Main pump design* - The main rocket engine turbopumps should be designed, for the fuel and the oxidizer, based on an assessment of the demonstration turbopump layout and efficiency. At the same time, the cycle must be defined, since several configurations are possible with a boost pump and a main pump for each fluid. Data on the fluids in their supercritical conditions are necessary.

3. *Liquid bearings* - Further experiments on the liquid bearings should be performed. The rig should be transformed to accommodate higher pressures that are necessary for higher speed operation of the existing bearing rig. A new micro bearing rig should be designed specifically for water with the tools developed in this work.

Appendix A

Description of the thrust bearing model

This appendix describes in details the compressible thrust bearing model. Then, the differences between the fully compressible and incompressible model are presented. Finally, the code architecture and the script of the incompressible model are given.

The pseudo-compressible model was initially developed by Jacobson [20] and investigated in the focus of this work. It was transformed to a incompressible model, and developed into a fully compressible model.

A.1 Incompressible thrust bearing model

As explained in Section 2.2, the thrust bearing consists in three resistances in parallel. They are a capillary resistance, an inherent resistance, and a radial outflow resistance. The pressure drop through each resistance is the product of the flow rate and the resistance.

ρ and μ are the density and viscosity of the liquid. From Wagner and Kruse [41], the values for water are $\rho = 998.2 kg/m^3$ and $\mu = 8.92 * 10^{-4} kg/(m.s)$. The viscosity is considered to be independent of the pressure.

A.1.1 Pressure and mass flow calculation

The mass flow rate is the same for the three resistances. From a guessed mass flow rate, we compute the pressure drop through each resistance from [19], and the total and static

pressure after each resistance. The flow rate is adjusted according to the calculated total pressure drop. A loop on the mass flow rate allows iterating this process, up to convergence of the exit static pressure to the desired pressure.

Capillary resistance

The orifice area $A_{orif} = \pi D_{cap}^2/4N_{cap}$ is the cross section of the flow passage, where D_{cap} and N_{cap} are the diameter and the number of capillaries in the thrust bearing considered. The average flow velocity in a capillary is $V_{orif} = \dot{m}A_{orif}\rho$. Finally, $\bar{l}$ is the ratio of the capillary length to its diameter. From [19], we define ϕ as

$$\phi = 0.25 + \frac{0.535\bar{l}^8}{0.05 + \bar{l}^7} \tag{A.1}$$

and τ as

$$\tau = \begin{cases} (2.4 - \bar{l}).10^{-\phi} & \text{if } \bar{l} < 2.4 \\ 0 & \text{if } \bar{l} \geq 2.4 \end{cases}$$

The Reynolds number based on the diameter is $Re = \rho.D.V_{orif}/\mu$. The friction coefficient is defined as

$$f = \begin{cases} 64/Re & \text{if } Re < 2300 \\ 1.02 * log_{10}(Re)^{-2.5} & \text{if } Re \geq 2300 \end{cases}$$

We define

$$\xi_\phi = -1.62log_{10}(Re) + 0.221log_{10}(Re)^2 + 3.29 \tag{A.2}$$

and

$$\epsilon = 0.461 - 0.265log_{10}(Re) + 0.203log_{10}(Re)^2 - 0.066log_{10}(Re)^3 + 0.013log_{10}(Re)^4 - 0.001log_{10}(Re)^5 \tag{A.3}$$

and

$$\xi = \begin{cases} \xi_\phi + \epsilon(1.5 + \tau) + f\bar{l} & \text{if } Re < 2300 \\ 1.5 + \tau + f\bar{l} & \text{if } Re \geq 2300 \end{cases}$$

The total pressure at the inlet of the capillaries is known, this is the supply pressure in the plenum. Both at the capillaries inlet and exit, the total to static pressure difference is the dynamic pressure $dynP = 0.5\rho V_{orif}^2$. The loss in static pressure from the capillary inlet to exit is

$$dp_{orif} = dynP * \xi = 0.5 * rho * V_{orif}^2 * \xi \tag{A.4}$$

Inherent resistance

The flow encounters an inherent restrictor effect when it enters a smaller dimension region, the radial outflow region. The restrictor characteristics are the cross-sectional area $A_{inherent} = \pi DgapN$, the average velocity in this region $V_{inherent} = \dot{m}/(\rho * A_{inherent})$ and the Reynolds number based on the hydraulic diameter $D_h = 2gap$, $Re_{rest} = \rho * V_{inh} * D_h/\mu$.

The model that is used for calculating the inherent restrictors is based on experimental results by Mechanical Technology Incorporated [1].

The proportion of dynamic pressure lost in this passage is called the MTI factor,

$$K_{MTI} = Re_{rest}/2000 * 0.31 - 0.122 * (Re_{rest}/2000)^2 + 0.282 * (Re_{rest}/2000)^3 + 0.179 \quad \text{(A.5)}$$

The constant K_{MTI} is an empirical loss coefficient based on experimental results from Carfagno and McCabe [7] and Vohr [40].

The total pressure at the inlet of the inherent restrictor equals the total pressure at the exit of the capillaries. Both at the inlet and exit of the region considered, the difference between the total and static pressure is the dynamic pressure $dynP_{inh} = 0.5 * \rho * V_{inh}^2$. The loss in static pressure in the inherent restrictor is

$$dp_{inh} = dynP_{inh} * K_{MTI} = 0.5 * rho * V_{inh}^2 * K_{MTI} \quad \text{(A.6)}$$

Radial outflow resistance

The third resistance occurs when the flow travels in the radial area between the stator and the rotor. This area is comprised between the capillaries located on a radius r_{orif} and the pad radius r_{exit}. We define the inlet and exit average velocities, the inlet Reynolds number, and an entry length

Assuming that the flow is fully developed in this area (which is verified with the Reynolds number), the pipe flow model is valid. For a pipe of diameter d and length L, the pressure drop is

$$-\Delta P = fL/d * 0.5\rho V^2 \quad \text{(A.7)}$$

where $f = 96/Re$ is the friction coefficient, $V = \dot{m}/(\rho A)$ the average velocity in the cross section $A = 2\pi rg$ (in our radial geometry), and $Re = \rho V 2g/\mu$ the local Reynolds number. Using finite differences, the pressure drop occurring between the radius r and $r + dr$ is

$$dP = -\frac{12\mu\dot{m}}{g^2\rho A}dr \quad \text{(A.8)}$$

The total pressure at the inlet of the inlet of the radial area equals the total pressure at the exit of the inherent restrictor. The static pressure at the inlet of the radial area is the total pressure minus the dynamic pressure $dynPrad_{inlet} = 0.5\rho Vrad^2_{inlet}$ where $Vrad_{inlet} = \dot{m}/(\rho r_{orif}.gap.2\pi)$ is the average velocity at the inlet of this region.

Integration of Equation A.8 yields the exit static pressure

$$Psrad_{out} = Psrad_{in} - \frac{6\mu\dot{m}}{g^3\rho\pi}.ln\Big(\frac{r_{orif}}{r_{exit}}\Big) \tag{A.9}$$

This pressure, after iteration on the mass flow rate, is converged to the desired exit pressure. A relaxation parameter is set to compute the step in mass flow versus the error in exit pressure.

A.1.2 Force and stiffness calculation

The pressure force on the rotor is calculated by integration of the pressure distribution.

If $Psrad_{in}$ is the static pressure after the inherent resistance, the pressure distribution on the bearing pad is

$$P = \begin{cases} Psrad_{in} & \text{if } r < r_{orif} \\ Psrad_{in} - \frac{6\mu\dot{m}}{g^3\rho\pi}.ln\Big(\frac{r}{r_{exit}}\Big) & \text{if } r_{orif} \leq r \geq r_{exit} \end{cases}$$

The corresponding pressure force $F = \int_0^{r_{exit}} 2\pi Prdr$ is

$$F = \pi r^2_{orif} Psrad_{in} + \frac{1}{2}\pi s(r^2_{orif} - r^2_{exit}) - \pi s r^2_{orif} ln\frac{r_{orif}}{r_{exit}} \tag{A.10}$$

where $s = \frac{6\mu\dot{m}}{g^3\rho\pi}$.

The thrust bearing stiffness is determined by calculating the pressure force exerted on the rotor by the forward thrust bearing and the aft thrust bearing, in two positions that vary by an axial eccentricity perturbation. The stiffness is the ratio of force variation and displacement.

A.2 Compressible thrust bearing model

The compressible thrust bearing simulation adopts the same architecture and resistance modelling than the incompressible code. This section describes the differences between the two.

A.2.1 Pressure and mass flow calculation

Capillary resistance

The capillary flow uses the same model. The density is calculated from the average static pressure in the capillary

$$\rho = \frac{(Pstat_{capinlet} + Pstat_{capexit})/2}{RT} \tag{A.11}$$

where $R = 287$ is the perfect gas constant, and T the temperature. The viscosity is given by

$$\mu = \left(\frac{T}{373}\right)^{0.67} * 2.2.10^{-}5 \tag{A.12}$$

The simulation includes the proper definition of compressible total pressure,

$$P_T = P_s \times \left(1 + \frac{\gamma - 1}{2} \times M^2\right)^{\frac{\gamma}{\gamma - 1}}, \tag{A.13}$$

instead of the sum of static pressure plus dynamic pressure, which is only valid at low Mach number.

The static pressure loss in the capillaries is

$$dP_{orif} = (Pt_{capinlet} - Ps_{capinlet}) * \xi \tag{A.14}$$

where $Pt_{capinlet}$ and $Ps_{capinlet}$ are the total and static pressures at the inlet of the capillary.

Inherent resistance

The gas density in the inherent restrictor is calculated from the average static pressure. The MTI model is used to describe the static pressure loss

$$dP_{inherent} = (Pt_{inhinlet} - Ps_{inhinlet}) * K_{MTI} \tag{A.15}$$

A coefficient $\dot{m}_{choke}$ is defined

$$\dot{m}_{choke} = \frac{Pt_{inhinlet}\left[\left(\frac{2}{1+\gamma}\right)^{\frac{\gamma+1}{\gamma-1}} \frac{\gamma}{R}\right]^{1/2}}{T^{1/2}}.A_{inherent} \tag{A.16}$$

The mass flow ratio $\overline{m} = \dot{m}/\dot{m}_{choke}$ is calculated. If $\overline{m}$ is greater than 0.975, the we consider the flow choked, and we fix $\dot{m} = 0.975 * \dot{m}_{choke}$. Then, we set the total pressure at the exit of the inherent region

$$P_T = P_s \times \left(1 + \frac{\gamma - 1}{2} \times M^2\right)^{\frac{\gamma}{\gamma - 1}} - P_{exp} \tag{A.17}$$

where P_{ext} takes into account the non-isentropy of the flow. It is such that the pressure loss for the radial outflow results in $Pstat_{radexit} = P_{atm}$ when the mass flow rate is $\dot{m} = 0.975 * \dot{m}_{choke}$. In other terms, the expansion loss at the exit of the inherent orifice is set up so that the total pressure adjusts itself, so that the radial outflow gives the proper exit static pressure.

Radial outflow resistance

The same method as presented earlier is used. The flow is considered to be fully developed. Because of the dependence of the density with pressure, Equation A.8 giving the pressure loss from r to r+dr is now

$$dP = -\frac{12\mu\dot{m}RT}{g^3 2\pi}\frac{dr}{Pr} \tag{A.18}$$

The static pressure at the inlet of the radial area is

$$Ps_{radinlet} = Pt_{radinlet} \times \left(1 + \frac{\gamma - 1}{2} \times M^2_{radinlet}\right)^{\frac{-\gamma}{\gamma-1}} \tag{A.19}$$

where $M_{radinlet} = V_{radinlet}/\sqrt{\gamma * R * T}$ is the Mach number at the inlet of the radial area. The flow velocity is calculated from the density, obtained from the static pressure $Ps_{radinlet}$. As can be seen, initialization and iterations are necessary to solve this closed problem.

Integration of Equation A.18 yields the exit static pressure

$$Psrad_{out} = \left[Psrad^2_{in} - \frac{12\mu RT\dot{m}}{g^3\pi ln\left(\frac{r_{orif}}{r_{exit}}\right)}\right]^{1/2} \tag{A.20}$$

This pressure, after iteration on the mass flow rate, is converged to the desired exit pressure.

A.2.2 Force and stiffness calculation

The force is calculated by pressure integration, as in the incompressible case. The stiffness is also obtained by computing the forces for the two thrust bearings, in two configurations.

The pressure force is, with $s = \frac{6\mu\dot{m}}{g^3\rho\pi}$,

$$\begin{aligned} F = {} & \pi r^2_{orif} Psrad_{in} + 2\pi\left[\frac{1}{2}r^2_{orif}e^{2Psrad^2_{in}/s} \times \left(\left[Psrad^2_{in} - sln\left(\frac{r_{orif}}{r_{exit}}\right)\right]^{1/2} \times \right.\right. \\ & \times e^{-2\left(Psrad^2_{in} - sln\left(\frac{r_{orif}}{r_{exit}}\right)\right)/s} - Psrad_{in}e^{-2Psrad^2_{in}/s}\Big) - \\ & - \frac{1}{8}r^2_{orif}e^{2Psrad^2_{in}/s}\sqrt{2\pi s}\Big[erf\left(\left[2(Psrad^2_{in} - sln(\frac{r_{orif}}{r_{exit}}))/s\right]^{1/2}\right) - \\ & \left.\left. - erf\left(\left[2Psrad^2_{in}/s\right]^{1/2}\right)\right]\right] \end{aligned} \tag{A.21}$$

A.3 Incompressible thrust bearing code

A.3.1 Hierarchy of the scripts

The hierarchy of the Matlab scripts, and their function, for the incompressible code is shown in Figure A-1. Each arrow represents information passing into the subroutine and information passing back into the parent subroutine.

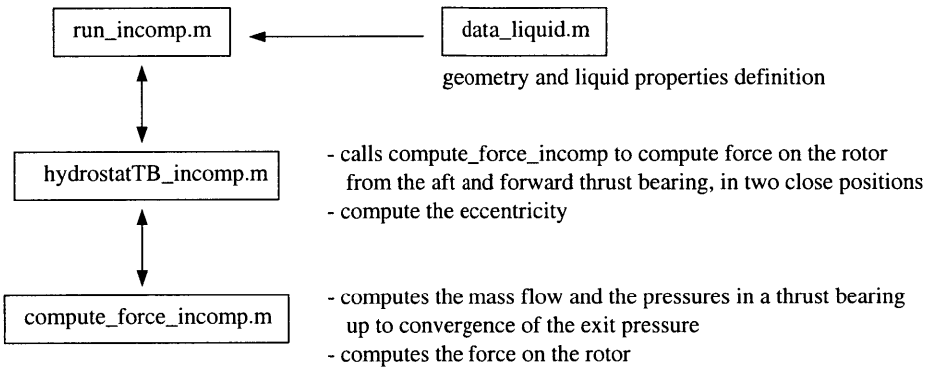

Figure A-1: Hierarchy and function of routines in the incompressible thrust bearing simulation

The hierarchy adopted allows a great modularity of the simulation. The main file can be transformed for automatic parameter analysis. Stiffness, mass flow, pressures and load can be computed automatically over a range of pressure, nozzle diameter, or eccentricity for example.

A.3.2 run_incomp.m

```
% This is the main file
% It calls hydrostatTB_incomp and writes the output
% Some modified versions of this file exist.
% They allow automatic parametric analysis (e.g., calls
% hydrostatTB_incomp over a vector of pressure)

% Antoine Deux - 03/14/00 - deux@mit.edu

[Psf, Psa, mdot_leftside, mdot_total, axial_force, net_ax_force,
stiffness] = hydrostatTB_incomp('data_liquid');
```

```
mdot_leftside

mdot_total

axial_force

net_ax_force

stiffness
```

A.3.3 data_liquid.m

```
% This is the file for the definition of the geometry
% and the liquid properties

% Antoine Deux - 03/14/00 - deux@mit.edu

% definitions for Micro Bearing Rig Thrust Bearings
disp('Running MICRO BEARING RIG geometry')

% FORWARD THRUST BEARING
l_f = 100;                          % length of orifice (microns)
D_f = 12;                           % diameter of orifice (microns)
N_f = 14;                           % number of orifices
r_orif_f = 0.55;                    % radius of the axis of the orifice (mm)
r_exit_f = 0.7;                     % radius of the thrust pad (mm)
Pin_f = 2;                         % Pressure inlet orifice (atm)

% AFT THRUST BEARING
l_a = 100;                          % length of orifice (microns)
D_a = 12;                           % diameter of orifice (microns)
```

```
N_a = 18;                          % number of orifices
r_orif_a = 0.75;                   % radius of the axis of the orifice (mm)
r_exit_a = 0.9;                    % radius of the thrust pad (mm)
Pin_a = 2;                        % Pressure inlet orifice (atm)

total_gap = 3.5;                   % total gap (microns)
eccent = 0;                        % eccentricity ratio


% definitions for the liquid properties

Tin = 300;                         % temperature, K
viscosity = 8.92*10^-4;            % liquid viscosity (xxxx)
rho = 1000;                        % volumic mass, kg/m3

% definitions for code

relax = 10^-11;                    % relaxation parameter for loop
pert = 0.0001;                     % eccentricity perturbation for stiffness calc
guess_m_dot = 5*10^-3;             %mass flow in g/s to begin loop; change value...
... if diverges

save geometry
```

A.3.4 hydrostatTB_incomp.m

```
% Script to simulate fully incompressible thrust bearings
% the filename in the argument has all the necessary parameters defining the
% geometry and operation
%
% The theory  is based on an electrical analogy with 3 resistors in series :
% orifice, inherent restrictor, radial flow
% cf. Stuart Jacobson pseudo compressible spreadsheet
```

```
%
% The code is called : [ML, MT, AF, NAF, ST] = hydrostatTB_incomp('data_liquid')
%
% where "data_liquid.m" is a file with all the geometric and operation
% description of the forward and aft TB
%
% Antoine Deux
% 03/14/00
% deux@mit.edu

function [Psf, Psa, mdot_leftside, mdot_total, axial_force,
net_ax_force, stiffness] = hydrostatTB_incomp(filename)


% Load geometry and running parameters
eval([filename]) load geometry


% forward TB, no ecc perturbation
disp('Running Fwd Thrust Bearing, No Eccentricity Perturbation');
[Psrad_in1,Psout1,Ax_force1,dP_orif1,dP_inh1,dP_rad1,m_dot1] =
compute_force_incomp(l_f,D_f,N_f,r_orif_f,r_exit_f,Pin_f,eccent,guess_m_dot);

% forward TB, ecc perturbation
disp('Running Forward Thrust Bearing, Eccentricity Perturbation');
[Psrad_in2,Psout2,Ax_force2,dP_orif2,dP_inh2,dP_rad2,m_dot2] =
compute_force_incomp(l_f,D_f,N_f,r_orif_f,r_exit_f,Pin_f,eccent+pert,m_dot1);

% aft TB, no ecc perturbation
disp('Running Aft Thrust Bearing, No Eccentricity Perturbation');
[Psrad_in3,Psout3,Ax_force3,dP_orif3,dP_inh3,dP_rad3,m_dot3] =
compute_force_incomp(l_a,D_a,N_a,r_orif_a,r_exit_a,Pin_a,-eccent,guess_m_dot);
```

```
% aft TB, no ecc perturbation
disp('Running Aft Thrust Bearing, Eccentricity Perturbation');
[Psrad_in4,Psout4,Ax_force4,dP_orif4,dP_inh4,dP_rad4,m_dot4] =
compute_force_incomp(l_a,D_a,N_a,r_orif_a,r_exit_a,Pin_a,-eccent-pert,m_dot3);

Psf = Psrad_in1;
Psa = Psrad_in3;
mdot_leftside = m_dot1;
mdot_total = m_dot1+m_dot3;
axial_force = Ax_force1;
net_ax_force = Ax_force1-Ax_force3;
net_ax_force_pert = Ax_force2-Ax_force4;

stiffness=(net_ax_force_pert-net_ax_force)/(total_gap/2*pert)*1000000;
```

A.3.5 compute_force_incomp.m

```
% Model for fully incompressible thrust bearing ( liquid )
% This function is a loop that entails to compute the mass flow and the force
% for one Thrust Bearing in one position.
%
% "while" loop with change in mass flow to converge P3 (exit)
% to ambient pressure (atmospheric)
%
% this function is used four times (aft and forward, and for each :
% two different eccentricities to obtain the stiffness)

%
% Antoine Deux  -  03/14/00  -  deux@mit.edu
%

function [Psrad_in,Psout,Ax_Force,dP_orif,dP_inh,dP_rad,m_dot] =
```

```
compute_force_incomp(L,D,N,r_orif,r_exit,Pin,eccentricity,guess_m_dot)


load geometry


Pin_gage = Pin - 1;
Psout = 0;              % do not change to atm pressure otherwise loop not initiated
Patm = 101325;          % Pa

gap = total_gap/2*(1-eccentricity)/10^6;    % meters
ratio = D/L;


m_dot = guess_m_dot;

% 0.1 for accuracy
% 1000 for speed

while abs(Psout - Patm) > 100       % loop


% ORIFICE FLOW

A_orif = pi*(D/10^6)^2/4*N;
V_orif = m_dot/1000/A_orif/rho;
lbar=1/ratio;
phi = 0.25+0.535*lbar^8/(0.05+lbar^7);
if lbar<2.4
    tau = (2.4-lbar)*10^(-phi);
    else
    tau = 0;
```

```
end;
Re = rho*D/10^6*V_orif/viscosity;
lR = log10(Re);
if Re<2300
    f = 64/Re;
    else
    f = 1.02*lR^-2.5;
end;
ksi_phi = -1.62*lR+0.221*lR^2+3.29;
epsilon =
0.461465-0.2648592*lR+0.2030479*lR^2-0.06602521*lR^3+0.01325519*lR^4-0.001058041*lR^5;
if Re<2300
    ksi = ksi_phi+epsilon*(1.5+tau)+f*lbar;
    else
    ksi = 1.5+tau+f*lbar;
end

dynP = 0.5*rho*V_orif^2;
Ptin = Pin*101325;                  % total pressure in, Pa
Psin = Ptin-dynP;                   % static pressure in, Pa
dP_orif = dynP*ksi;
Psorif_out = Psin-dP_orif;          % static pressure out, Pa
Ptorif_out = Psorif_out+dynP;           % total pressure out, Pa


% INHERENT RESTRICTOR

Dh = 2*gap;
A_inherent = pi*D/10^6*gap*N;

V_inh = m_dot/1000/(rho*A_inherent);
Re_rest = rho*V_inh*Dh/viscosity;   % it is Re(2g)
```

```
ksi_in = 0.5*(0.85+400*1/Re); ksi_out = 0.5*(0.85+400*1/Re_rest);

Kmti =
Re_rest/2000*0.31-0.122*(Re_rest/2000)^2+0.282*(Re_rest/2000)^3+0.179;

% lR_rest = log10(Re_rest);
% A = -25.12458+118.5076*lR_rest-170.4147*lR_rest^2+118.1949*lR_rest^3-...
% 44.42414*lR_rest^4+9.09524*lR_rest^5-0.9244027*lR_rest^6+0.03408265*lR_rest^7;
% B = 1.07+0.05*A;
% ksi_l = A*B;

dynP_inh = 0.5*rho*V_inh^2;
dP_inh = dynP_inh*Kmti;              % MTI model  -
                                     % for SAJ model (using ksi_l) cf stu's paper

Psinh_in = Ptorif_out-dynP_inh;      % static pressure in
Psinh_out = Psinh_in-dP_inh;         % static pressure out
Ptinh_out = Psinh_out+dynP_inh;      % total pressure out


% RADIAL FLOW

Vrad_in = m_dot/1000/rho/(r_orif/1000*2*pi*gap);
Vrad_out=m_dot/1000/rho/(r_exit/1000*2*pi*gap);
Re_in=rho*Vrad_in*2*gap/viscosity;
Le = 0.06*Re_in*2*gap;
ratio_dr_Le = (r_exit-r_orif)/1000/Le;     % must be >>1 for analysis to be valid

dynPrad_in = 0.5*rho*Vrad_in^2;
dynPrad_out = 0.5*rho*Vrad_out^2;
Psrad_in = Ptinh_out-dynPrad_in;
```

```
Psrad_out =
Psrad_in-6*viscosity*m_dot/1000/(gap^3*rho*pi)*log(r_exit/r_orif);

dP_rad = Psrad_in-Psrad_out;
Ptrad_out = Psrad_out+dynPrad_out;


% INTEGRATED FORCE

s = 6*viscosity*m_dot/1000/(gap^3*rho*pi);
Fint = pi*(r_orif/1000)^2*Psrad_in;             % Force for r<r_orif
Fext = pi*((Psrad_in+s/2)*(r_exit^2-r_orif^2)/1000^2-s*r_exit^2/1000^2*...
log(r_exit/r_orif));    % Force for r_orif<r<r_exit
Ftotal = Fint + Fext;


% ADJUST MDOT UNTIL Psrad_out = 101325Pa

if Psrad_out > 0
    m_dot = m_dot-(101325-Psrad_out)*relax;
    else
    m_dot = m_dot/2;
end; Psout = Psrad_out;

Ax_Force = Ftotal;


end;
```

Appendix B

Micro bearing experiment package drawings

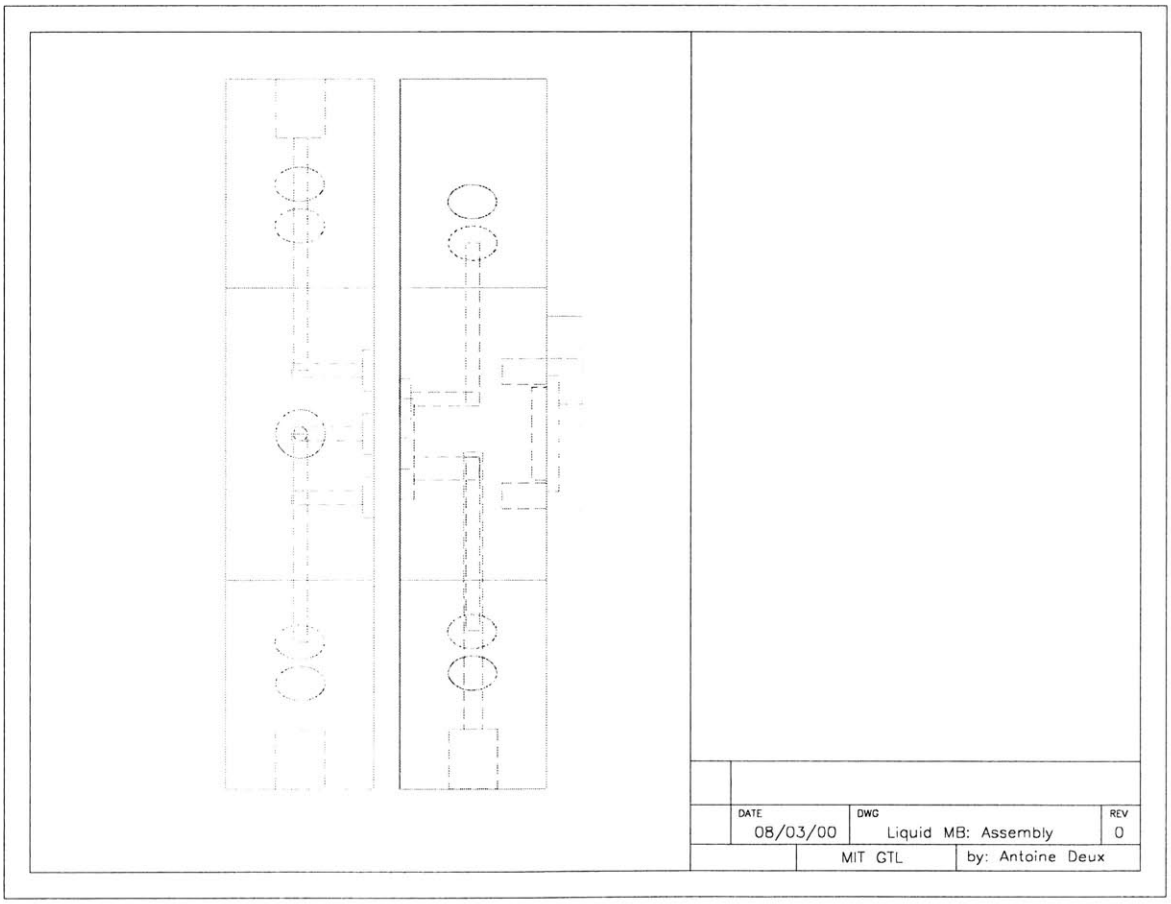

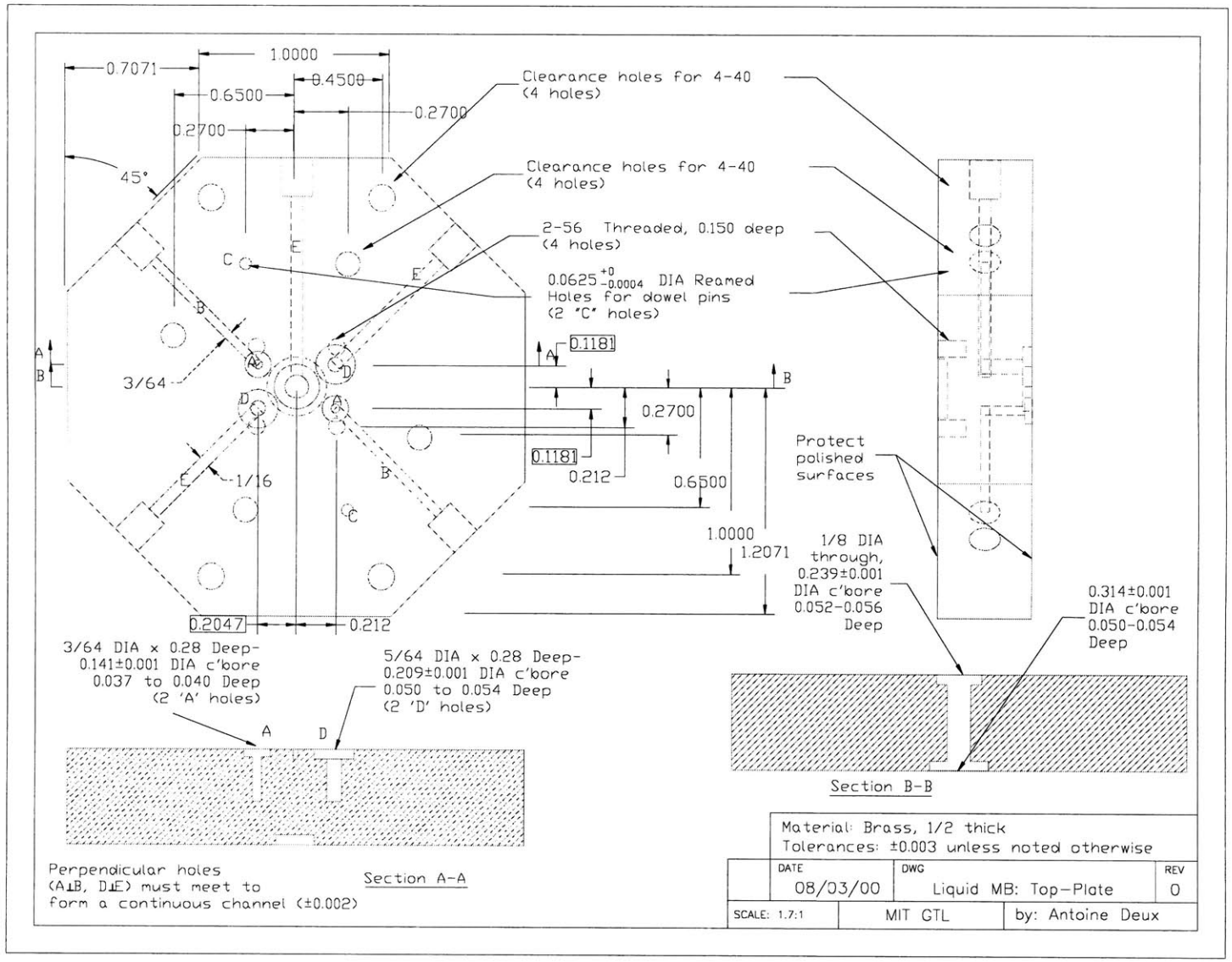
1.0000
0.7071
0.4500
0.6500
0.2700
0.2700
45°
Clearance holes for 4-40
(4 holes)
Clearance holes for 4-40
(4 holes)
2-56 Threaded, 0.150 deep
(4 holes)
0.0625 +0 -0.0004 DIA Reamed
Holes for dowel pins
(2 'C' holes)
0.1181
3/64
0.2700
0.1181
0.212
0.6500
1.0000
1.2071
1/16
0.2047
0.212
Protect
polished
surfaces
1/8 DIA
through,
0.239±0.001
DIA c'bore
0.052-0.056
Deep
0.314±0.001
DIA c'bore
0.050-0.054
Deep
3/64 DIA x 0.28 Deep-
0.141±0.001 DIA c'bore
0.037 to 0.040 Deep
(2 'A' holes)
5/64 DIA x 0.28 Deep-
0.209±0.001 DIA c'bore
0.050 to 0.054 Deep
(2 'D' holes)
Section A-A
Section B-B
Perpendicular holes
(A⊥B, D⊥E) must meet to
form a continuous channel (±0.002)
Material: Brass, 1/2 thick
Tolerances: ±0.003 unless noted otherwise
DATE
08/03/00
DWG
Liquid MB: Top-Plate
REV
0
SCALE: 1.7:1
MIT GTL
by: Antoine Deux

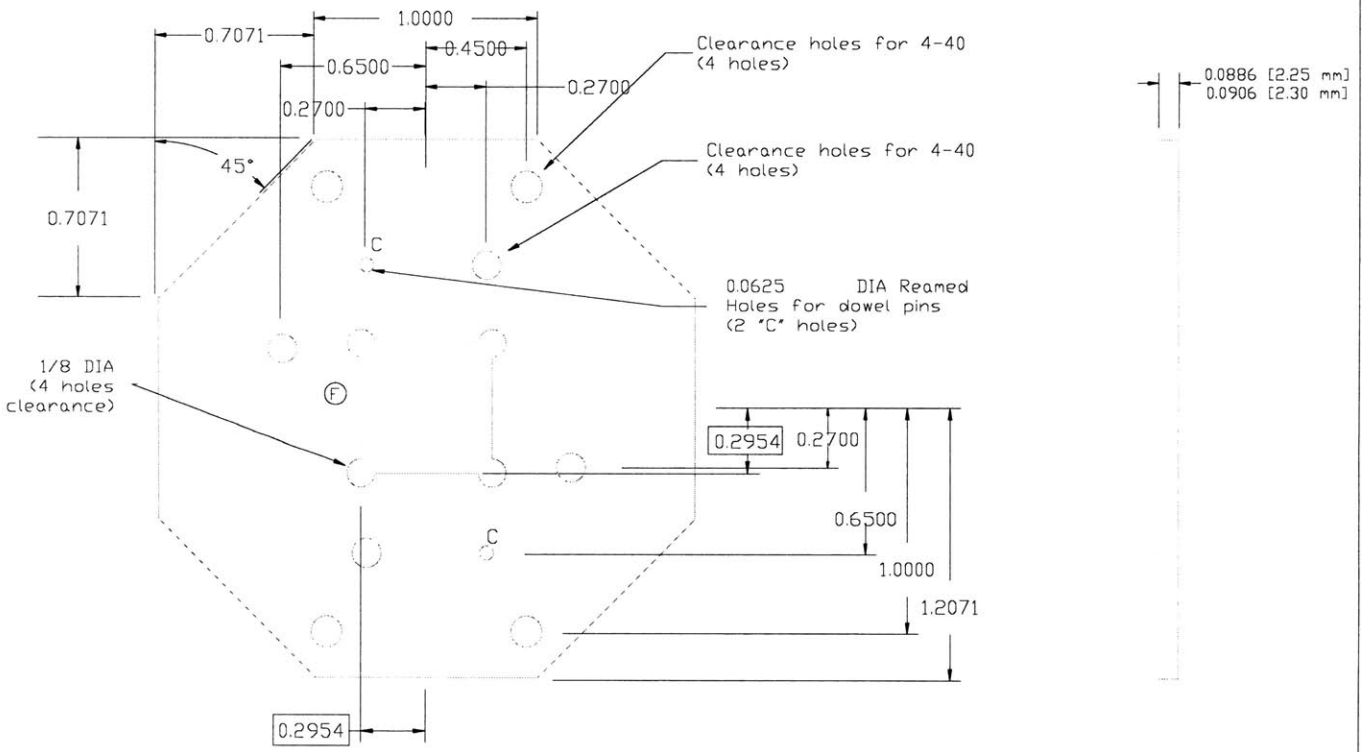

NOTES:

Perpendicularity of center square ('F'), and alignment to the dowel pins ('C' holes) is critical (±0.001)

Material: aluminum Tolerances: ±0.003 unless noted otherwise		
DATE 08/03/00	DWG Liquid MB: Spacer–Plate	REV 0
SCALE: 1.7:1	MIT GTL	by: Antoine Deux

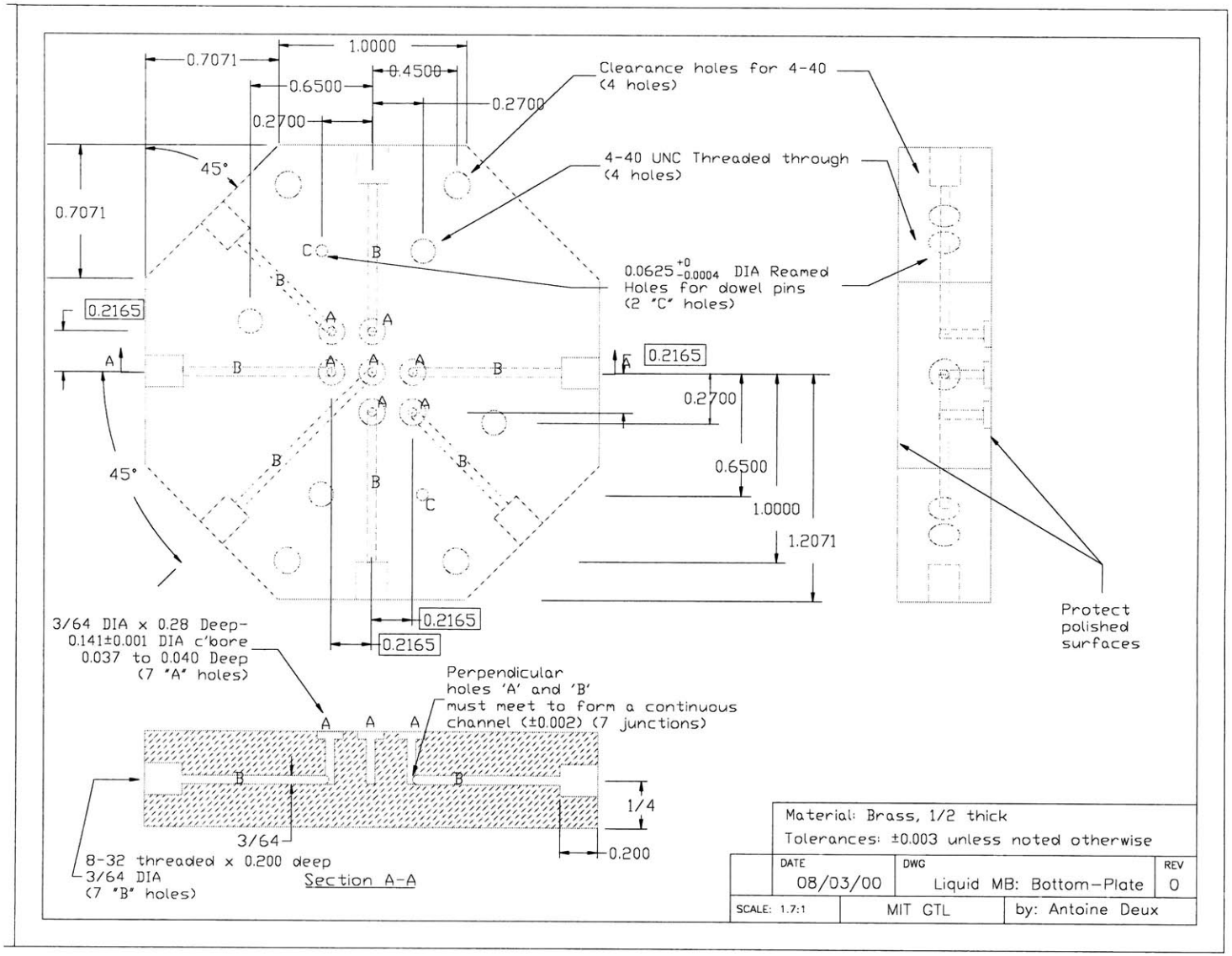
1.0000
0.7071
0.4500
0.6500
0.2700
0.2700
45°
0.7071
Clearance holes for 4-40
(4 holes)
4-40 UNC Threaded through
(4 holes)
0.0625 +0 −0.0004 DIA Reamed
Holes for dowel pins
(2 "C" holes)
0.2165
0.2165
0.2700
0.6500
1.0000
1.2071
45°
0.2165
0.2165
Protect
polished
surfaces
3/64 DIA x 0.28 Deep-
0.141±0.001 DIA c'bore
0.037 to 0.040 Deep
(7 "A" holes)
Perpendicular
holes 'A' and 'B'
must meet to form a continuous
channel (±0.002) (7 junctions)
1/4
3/64
0.200
8-32 threaded x 0.200 deep
3/64 DIA
(7 "B" holes)
Section A-A
Material: Brass, 1/2 thick
Tolerances: ±0.003 unless noted otherwise
DATE
08/03/00
DWG
Liquid MB: Bottom-Plate
REV
0
SCALE: 1.7:1
MIT GTL
by: Antoine Deux

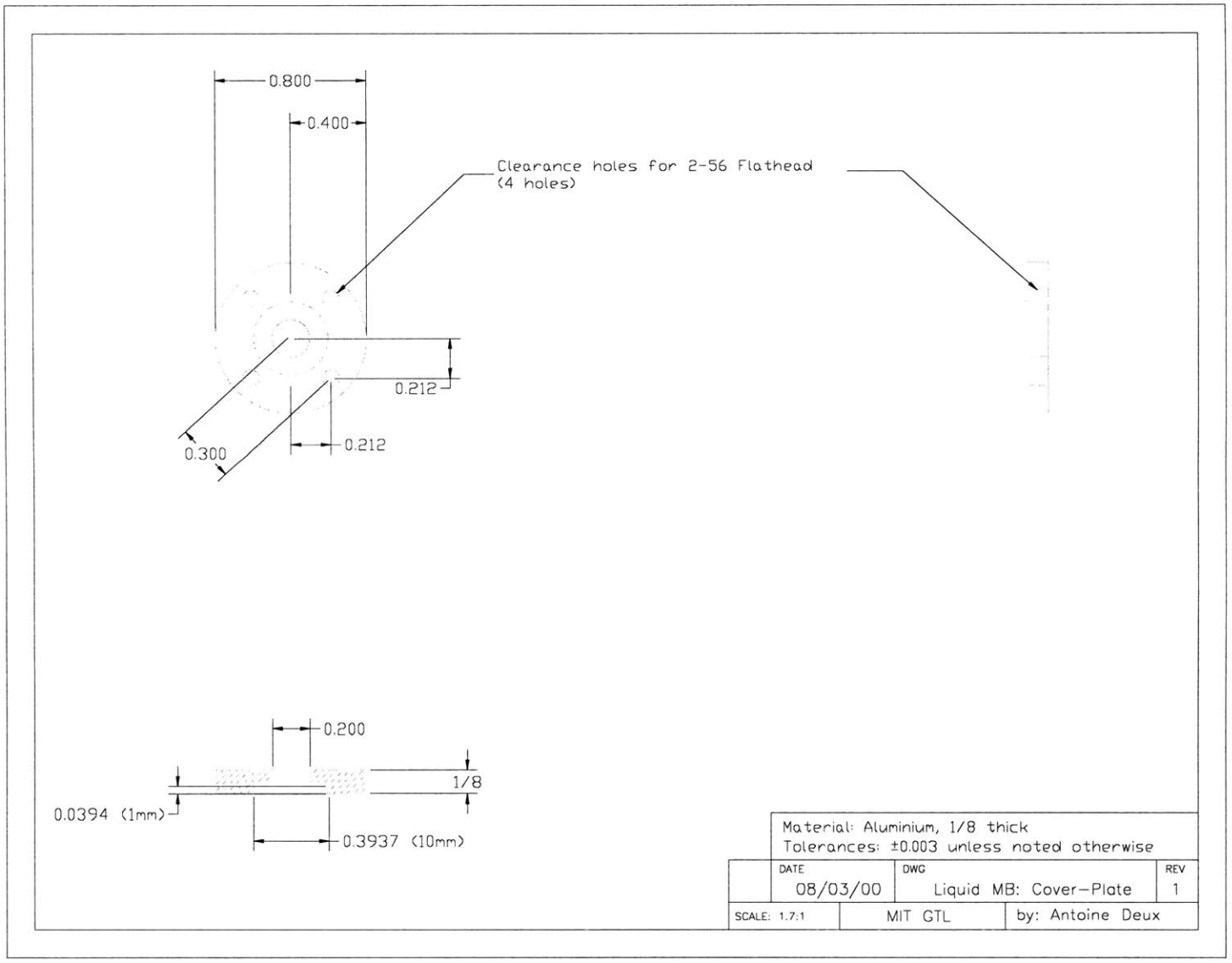
0.800
0.400
Clearance holes for 2-56 Flathead
(4 holes)
0.212
0.300
0.212
0.200
1/8
0.0394 (1mm)
0.3937 (10mm)
Material: Aluminium, 1/8 thick
Tolerances: ±0.003 unless noted otherwise
DATE
08/03/00
DWG
Liquid MB: Cover-Plate
REV
1
SCALE: 1.7:1
MIT GTL
by: Antoine Deux

Appendix C

Description and analysis of the contamination issue

The early water bearings tests were unsuccessful since water was not flowing in the thrust bearings. The blockage was in a large part due to the plastic tubing in the rig. This appendix summarizes the contamination issue, presents the likely sources of the contamination and the cleaning procedures that were used, and explains how it was fixed.

C.1 Contamination summary

In this section, some flow tests are realized with gas. This is not in contradiction with the fact that liquid flow in thrust bearings is investigated. Indeed, as will be explained, liquid flow was not measurable in the first tests. The corresponding blockage was remaining in the die, and thus could be quantified with gas flow tests.

C.1.1 First series of tests

The first water flow tests were unsuccessful. It could be visually observed that water was going through the forward thrust bearing (since it exits in the main exhaust that we can look at), and was then stopping. No steady mass flow was observed for inlet pressures up to 200 psi.

Surface tension was believed to be the blocking issue because of the gas/liquid interface and the small dimensions. However, the smallest dimension is the radial gap, which is between 1.5 and 2 μm. This does not explain a blockage for such high pressures. A water/air

interface of 1.5 μm can sustain 28 psi. However, tests were conducted with vacuuming the exhaust down to 30 mTorr and heating the packaging with a heat gun. This did not improve the results.

After being contaminated with water, dies would be dried, then tested on the gas rig, and their pressure/flow characteristics would be compared to before the contamination. It was observed that a large blockage to the flow was present. This proves that the blockage is not due to surface tension, but a form of particles or film deposition, despite the 0.5 μm filter in the rig.

Tests were conducted on dies without rotor. The thrust bearing consists in a set of capillaries that are 10 μm in diameter. Water tests were possible with this larger dimension. Figure C-1 presents the results of these tests. Gas experiments were conducted before and after water contamination, and after a cleaning procedure with acetone, which is described in Section C.3. Three water experiments were performed, the last one after cleaning.

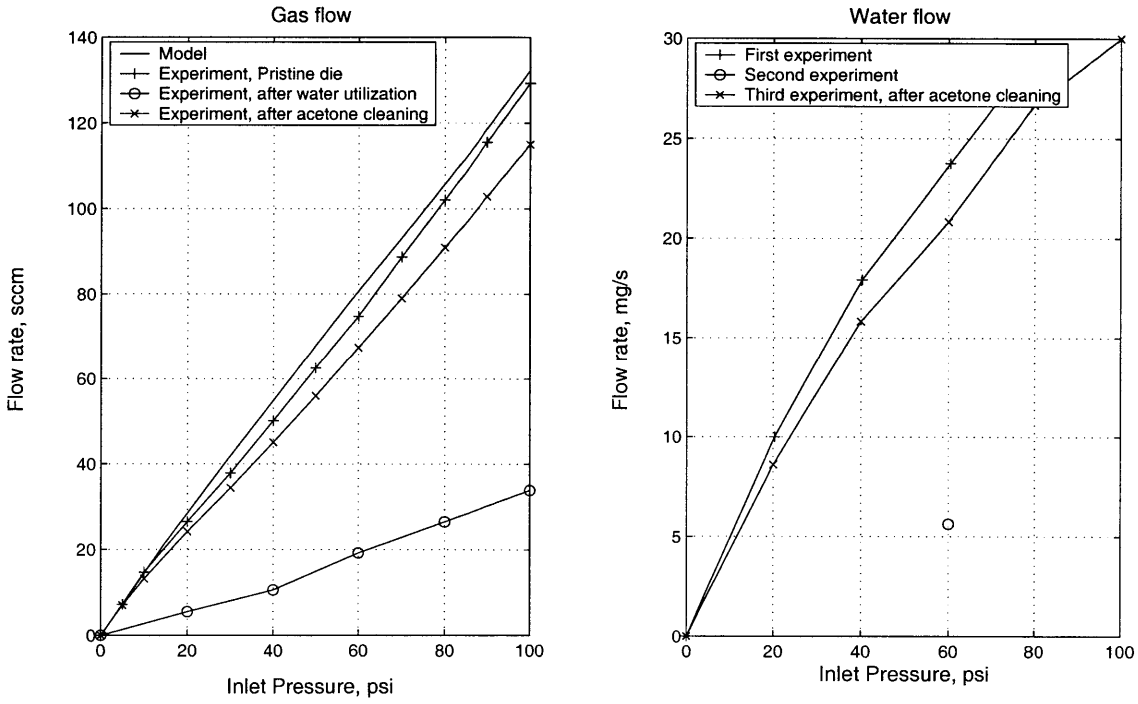

Figure C-1: Capillaries flow experiments with the original setup.

As can be seen from both gas and liquid experiments, the water contamination caused a large flow blockage, since after a first water use, the flow was reduced by 75 to 80%. However, the cleaning procedure was efficient and allowed recovering 90% of the flow.

Lots of water and gas experiments were conducted with various conditions on the actual thrust bearing geometry. Dies were recovered with cleaning procedures as described in C.3. Gas flow was then possible, but not liquid flow.

C.1.2 Second series of tests - filters added

Some new 0.3 μm filters from Cole Parmer were added on the thrust bearing lines, at the inlet of the mass flow meters. This improved slightly the results since we could observe flow in the thrust bearings. However, these flows were consistently blocking after 1 to 2 minutes, preventing any data measurement. This suggests that the blockage is less important, due to these new filters.

In order to quantify this reduced blockage, gas and water flow tests on capillaries are performed. Results are shown in Figure C-2. As can be seen, a water contamination brings a blockage of approximately 5 to 10% both for gas and water. Compared to the gas model, this corresponds to a reduction in diameter of 0.2 μm.

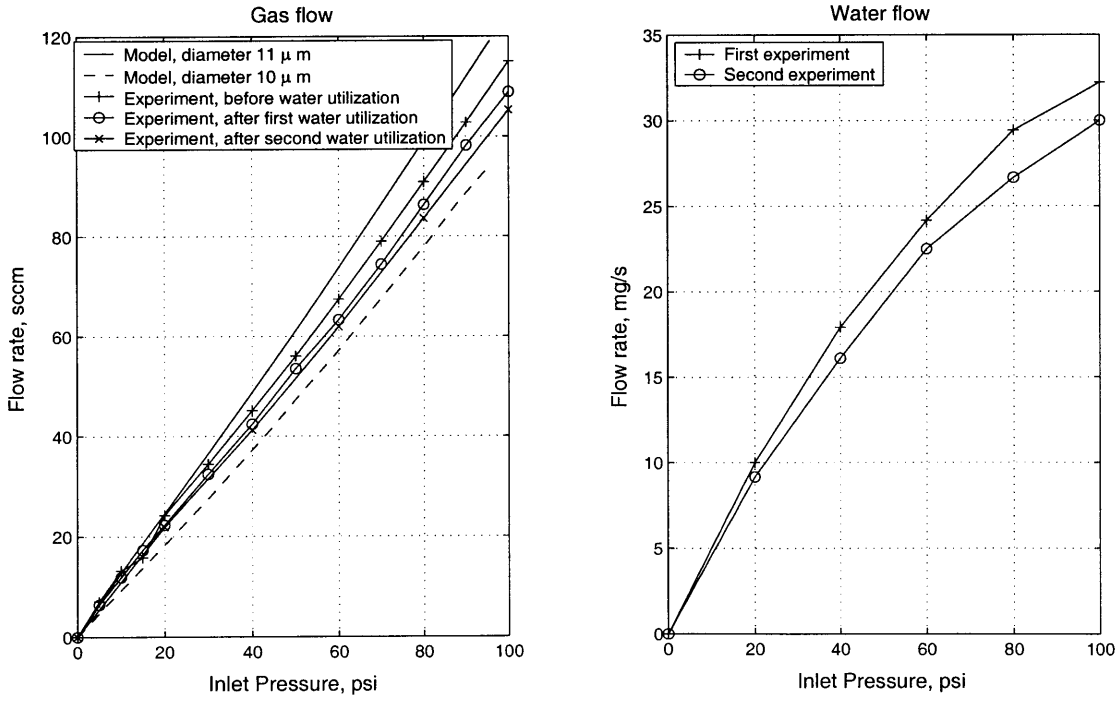

Figure C-2: Capillaries flow experiments with the second setup.

Gas flow tests were conducted on the actual thrust bearing geometry before and after

some flow tests. Results are presented in Figures C-3 and C-4. As is seen, the flow is reduced from 30 to 70% after each water contamination. Features are not perfectly identical for both thrust bearings. However, the rotor is still free to move axially as suggested by the axial position tests presented in Figure C-4.

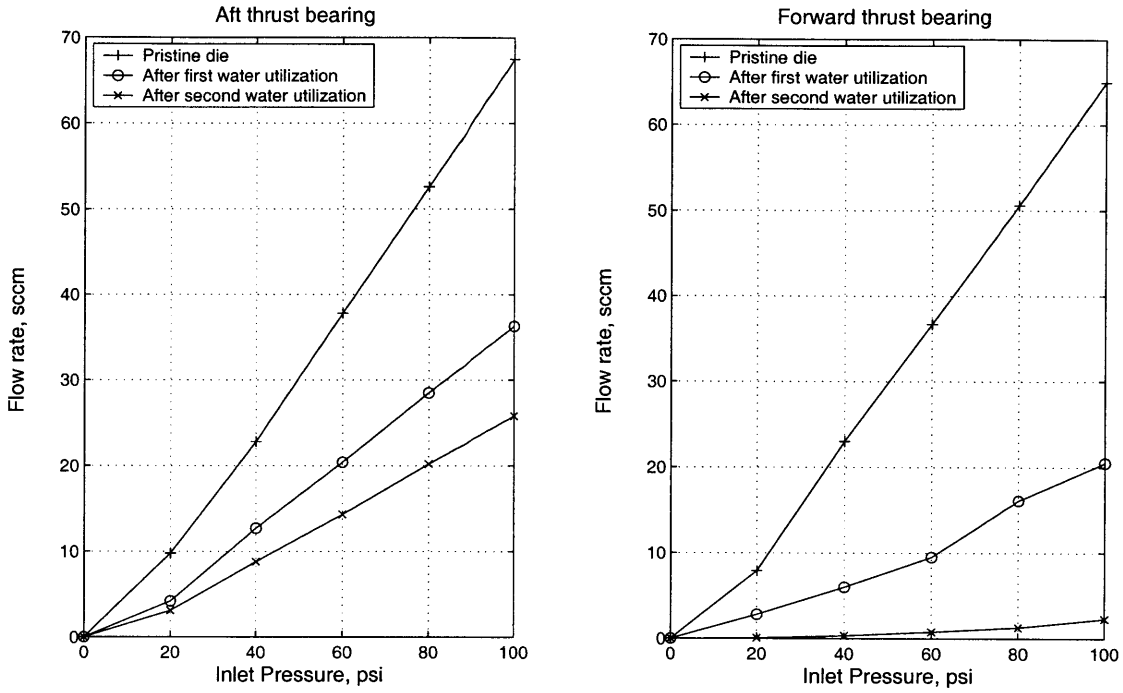

Figure C-3: Thrust bearings gas flow experiments at maximum gap before and after water contamination. Die 2-12.

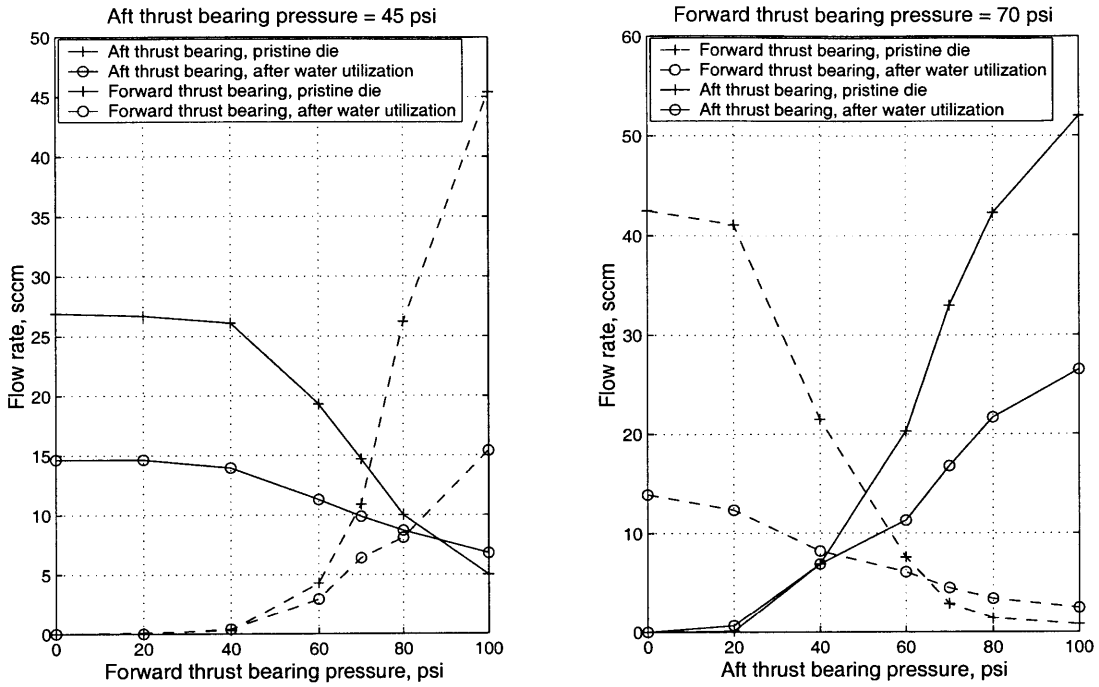

Figure C-4: Thrust bearings gas flow experiments before and after water contamination. Rotor axial position tests. Die 2-12.

C.1.3 Third series of tests - plastic tubing removed

It was suggested by Broderick [6] that vinyl and nylon tubing leak more plasticisers, are generally less pure (but stronger), than teflon tubing, which is broken down into sub-types, for further optimization on inertness, acid, abrasion, or temperature resistance, into PFA, PFE, or some other variation. Since purity and contamination were our concerns, the 1/16" nylon and vinyl tubes that feed the packaging were changed to teflon tubing.

With this setup, water flow was observed and measured in the thrust bearings. Results are shown in Figure C-5. It is observed that the simple change of plastic tubing decreases considerably the blockage. However, the flow is decreasing over time. The blockage is approximately linear with time, this suggests a slow film deposition. The flow is reduced by 50% after 15 to 20 minutes.

Following these observations, all the plastic lines in the rig were changed to copper tubing. As can be seen from Figure C-6, a same die presented the same flow blockage over time with both copper and Teflon. However, it was decided to remove all plastic from the rig to avoid further plasticisers leakage.

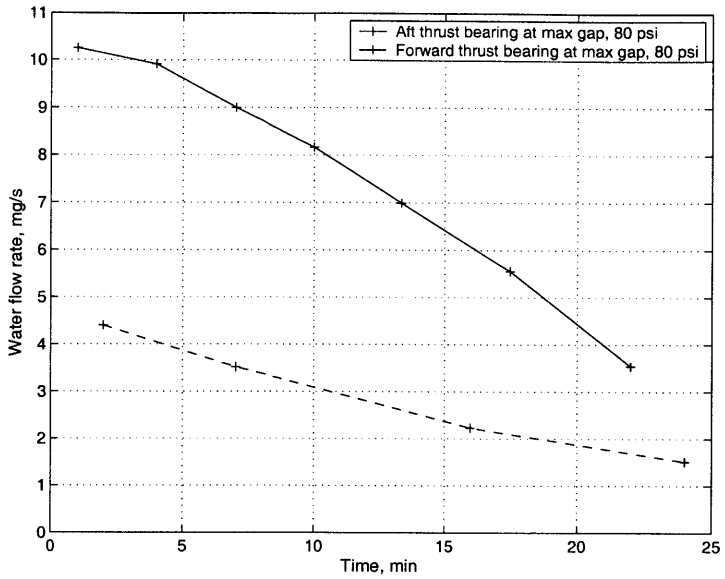

Figure C-5: Thrust bearings water flow experiments at maximum gap after changing tubing with teflon. Die 3-12.

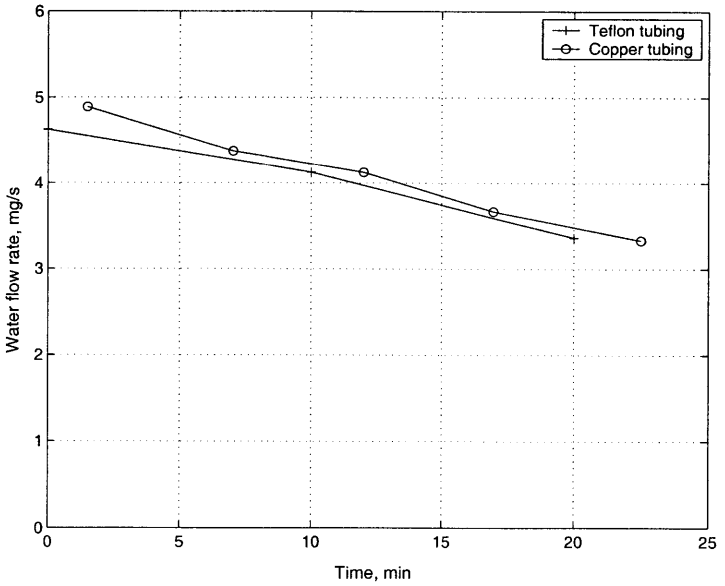

Figure C-6: Die 5-4 aft thrust bearing water flow experiments with Teflon and copper feeding lines.

At the same time, the water source was modified. Water from the MTL cleanroom was used. This water come from a DI plant, with a continuous recirculation path through filters, and the maximum size of trapped particles is smaller than 10 nm. The water was no more recycled.

Moreover, a new in-line 0.1 μm filter was added. The new rig was cleaned by flowing acetone, then ethanol, then extensive rinsing with water.

As can be seen, the blockage issue was not totally solved at this point. It is believed that the remaining blockage was due to residues from the cleaning procedure as explained in Section C.3. Indeed, after the dies were cleaned with Piranha or a HF dip, and after extensive testing with these new better procedures, a lot of water was flown through the rig and the packaging, no more blockage was observed.

C.2 Causes of flow blockage

A lot of assumptions have been made to explain the water flow blockage. As was seen, the surface tension is observed in these experiments, but it does not explain this large blockage, since the same amount of blockage was observed with gas flow after the die was dried and heated.

The first two points hereafter are major issues for MEMS testing in a liquid environment, since they were observed to be the sources of contamination. The third point is an assumption that we have neither validated nor invalidated, but that needs to be considered.

- *Plasticisers leakage from plastic tubing* - As was detailed in the previous section, vinyl and nylon tubing should not be used in liquid experiments involving micron-scale passages. Though inert with gas, these plastic depolymerize and leak plasticisers when water is flown though. The same phenomena was observed with ethanol.
- *Residues from cleaning procedures* - It appears that cleaning the die with acetone or ultrasonic cleaning leaves some residues. This residues do not interact with gas flow, but they do with water flow. It might be due to the larger momentum of water, and then water is convecting these residues in the critical places where they block the flow; or maybe they are dissolved by water, and they deposit in the critical places.

- *Chemical reaction* - It was suggested by Senturia [38] that the fact that Piranha cleaning gives the best results might suggest that slow silicate chemistry is happening. Strong acids will leave the residual oxide on the surface more in a protonated state than a hydroxylated state. Conversion to the hydroxylated state, which is what leads to complex silicate formation would be slower after strong piranha immersion. And silicates can be gummy gel-like things that might swell and partially block the channels when wet, something that might not happen when dry.

C.3 Cleaning procedures

Different cleaning procedures have been used to recover the dies after the thrust bearings were blocked.

- *Acetone in ultrasonic bath, and water rinsing* - This solution is believed to leave a residue.

- *Oxalic acid in ultrasonic bath, and water rinsing* - This solution was not often effective.

- *Ultrasonic solution in ultrasonic bath* - This solution is believed to leave a residue. Figure C-7 compares the flow in a same die after this cleaning, or piranha cleaning. It is seen that the flow decreases much faster over time after an ultrasonic solution cleaning.

- *Standard fabrication procedure : acetone, then isopropanol, then methanol, successively in ultrasonic bath, and water rinsing* - This solution was not better that ultrasonic solution cleaning in terms of flow decrease over time.

- *1110A cleaning solution in ultrasonic bath, then rinsing* - This solution was not better that ultrasonic solution cleaning in terms of flow decrease over time.

- *Piranha bath, then rinsing* - As is seen in Figure C-7, this solution is much better than ultrasonic solution cleaning. The fact that in Figure C-7, the flow still decreases over time, is thought to be due to contamination of the packaging. Indeed, after extensive tests, the flow over time was steady. During spin tests, some dies were tested more than 10 hours without significant flow decrease in the thrust bearings.

- *HF dip, then rinsing* - This solution was tested, and brings the same results than a Piranha cleaning, as can be seen from Figure C-7.

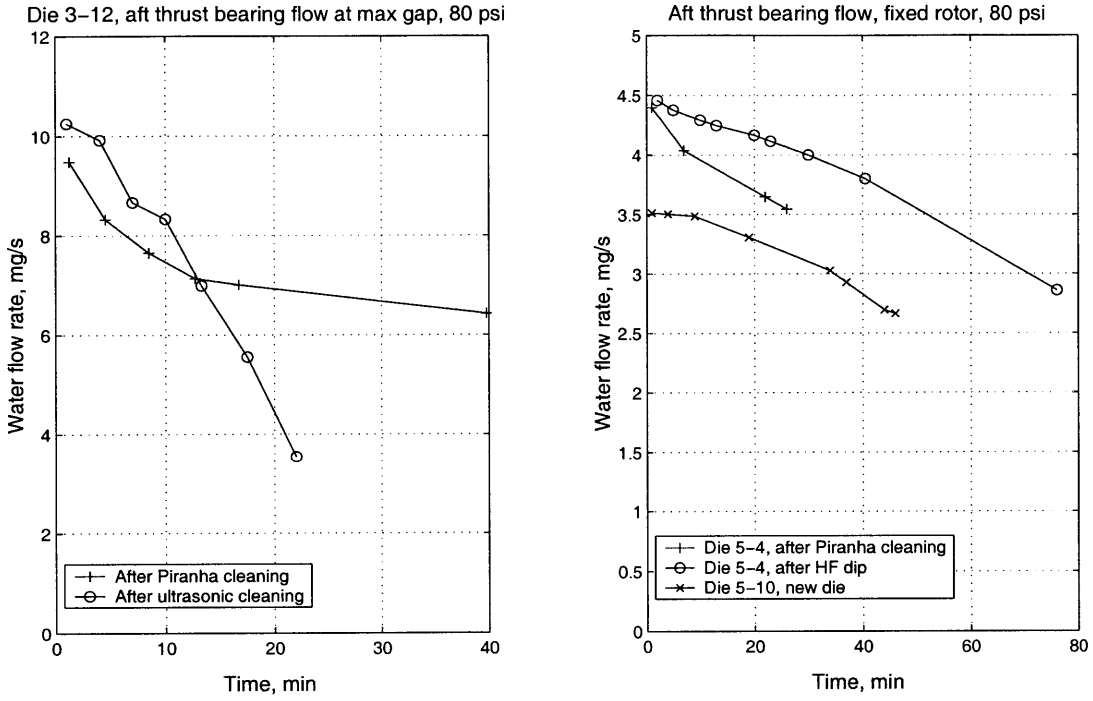

Figure C-7: Thrust bearings water flow tests for cleaning procedures comparison.

Appendix D

Turbopump list of requirements, specifications and realizations

DESIGN/FUNCTIONAL REQUIREMENT	SPECIFICATION	REALIZATION
A - FUNCTIONAL DESIGN		
A1 - Performance		
Pump: pressure rise = 30atm for a mass flow rate = 2.5g/s and Pin$\leq$ 3 atm	Fluid: water, room temperature. Pin = 2atm. Pexit = 32atm	R=1mm, Ω=750,000 rpm, Blade height=225mm
Turbine: same Ω as pump, same mass flow as pump, same blade height	Power required 50W, fluid: air	R=3mm, Pin = 24atm, Pout = 9atm
Account for 3D effects in the 2D design of the pump and turbine	Increase pump mass flow rate in the required pump power calculation. Impose losses in the turbine design	Pump designed for 3.5 g/s (we expect a 30% loss in mass flow between 2D calc and expe). Turbine design was imposed a 3D losses profile coming from 3D calculations

A2 - Bearings and Rotor Dynamics		
Ability to pressure balance the rotor axially without thrust bearings	Back plenum with controllable pressure (pressurization or ventilation)	Circular back plenum of radius 1.5mm (inside aft thrust bearings) and depth 60mm, with independent piping in its center
Axial stiffness	Use demonstrated symmetric hydrostatic thrust bearings. Stiffness $\geq$ 4N/μm (for zero eccentricity)	60 injectors, dia 12mm, length 100μm, P 40atm, total gap 5μm
Radial stiffness	Use demonstrated hydrostatic journal bearings. Stay below 6 times the natural frequency i.e. natural frequency $\geq$ 2100Hz	Hydrostatic journal bearing - clearance 10μm. $\Delta p = 10psi$ for design speed give natural frequency = 2500Hz
A3 - Simplicity		
Maximize simplicity of design	Single wafer rotor	Pump and turbine on same side
A4 -Internal Pressure Drops		
Minimize internal pressure drops	Piping pressure loss $\leq$ 20% of total pressure	Double connections when high mass flow to reduce Mach (if possible). Large flow area when high mass flow (inlet & exit of pump & turbine). Short flow tubes. Injectors for turbine in & out sized for small P drop

A5 - Structural Integrity Pyrex wafer must withstand high P from pump plenum	Thickness $\geq 430\mu$m	Wafer thickness = 500μm
Walls between plenum or tubes thick able to sustain high P	Wall section $\geq 100\mu$m	Smallest wall section: 200μm
A6 - Low Drag		
Dissipated power by viscous drag must be a small fraction of the delivered turbine power	Power dissipated $\leq$ 2.5W(5% of turbine power)	Back plenum depth = 60μm. Power dissipated = 1.7W
A7 - Leakage		
Minimize leakage from pump exit to turbine inlet	Seal ensured by forward thrust bearing	
A8 - Start-up		
Ability to start rotation of turbo machinery	Net power $\geq$ 0 for speed=0	

B - FABRICATION		
B1 - Technology		
Use of proven technology when possible	Process similar to MCBR: single wafer rotor, gas bearings, 300μm journal bearing, 5 stack bonding. Oxide release proven from turbocharger fab.	
B2 - Simplicity		
Maximize fab simplicity	Single wafer rotor	
B3 - Unbalance		
Minimize unbalance	Unbalance $\leq$ 5% or 0.6μm. Rotor etch uniformity $\leq 1\mu$m over 6μm	Single wafer rotor. Haloes etch when critical features. Spacing of the dies on the wafer

C - EXPERIMENT		
C1 - Measurements		
Ability to measure P during experiment	Static pressure taps	5 most important pressure taps: turbine inlet, turbine exit, turbine inter-row, pump exit, journal bearing
Ability to measure speed and rotor motion (whirl) during experiment	Use demonstrated frequency measure via fiber optic + lens	4 speed bumps
C2 - Cavitation		
Ability to observe pump blade exit	Observation of blade TE is possible via pump exit with long range microscope	Wafer 0 is glass, geometric arrangement in wafers 1&2
C3 - O-Rings		
Minimize leakage risk at interface die/packaging	All O-rings same thickness	O-rings dimensions: 0.078in.x0.016in. and 0.035in.x0.016in.
Ability to make sure o-rings are in place in the packaging	All connections (and O-rings) at the back side	
C4 - Plate deflection		
Avoid center connection for thrust bearing gap	No compression on the center of the die	No center O-ring
C5 - IR image		
Ability to observe internal features by IR	Horizontal separation of vertical features when possible	

Appendix E

Turbopump thrust bearing parametric study results

HIGH SPEED : 750,000 RPM

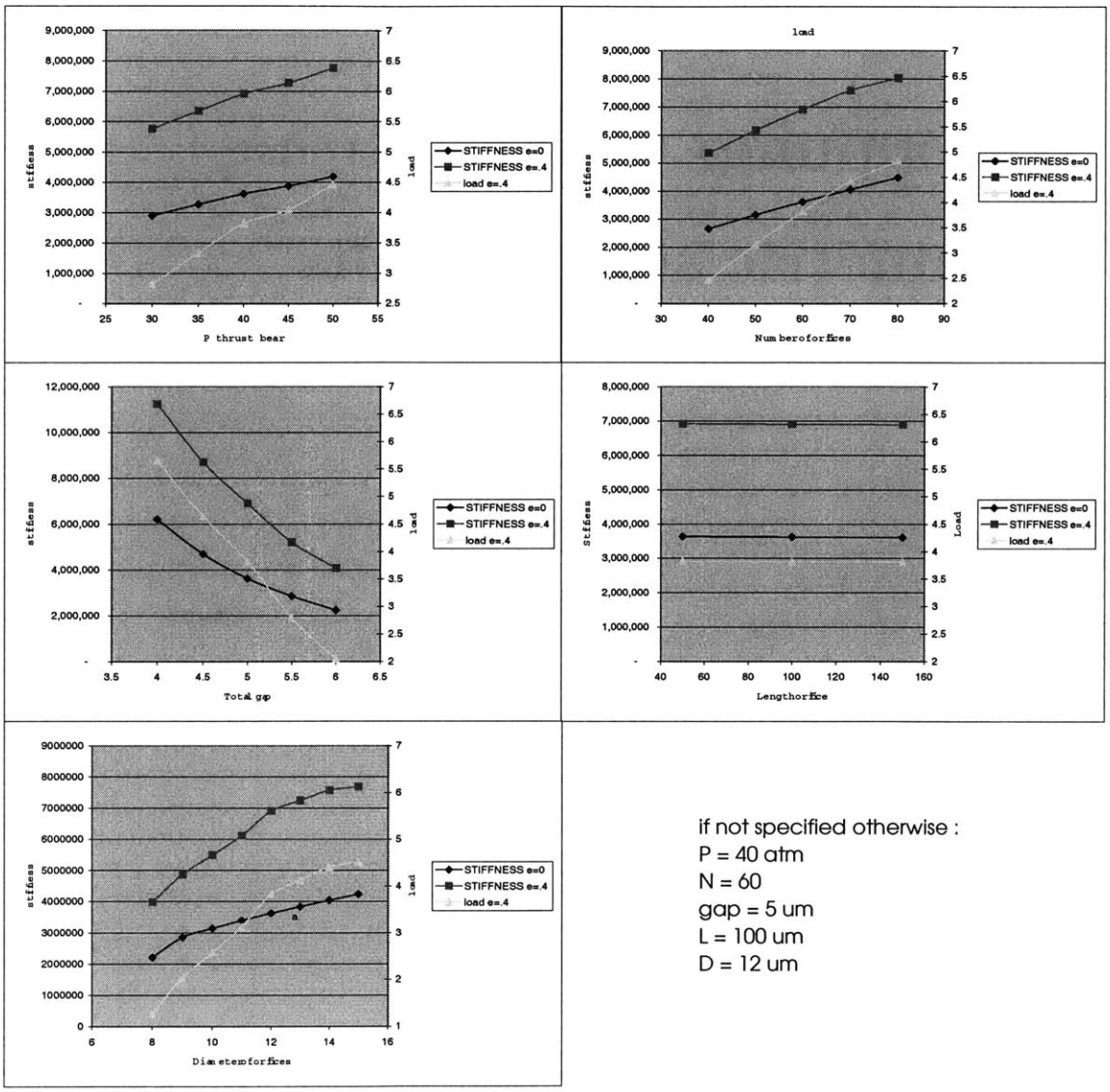

if not specified otherwise :
P = 40 atm
N = 60
gap = 5 um
L = 100 um
D = 12 um

LOW SPEED : 190,000 RPM

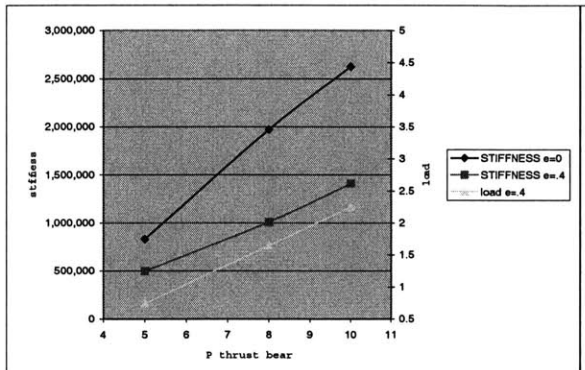

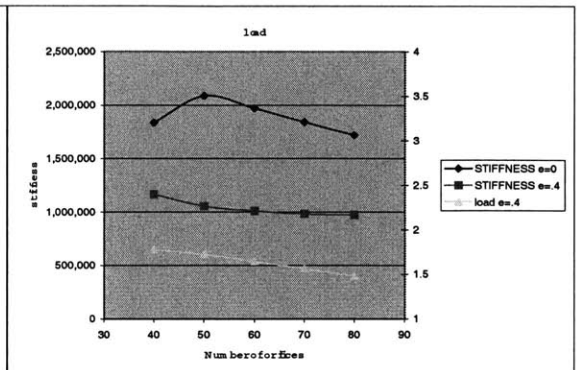

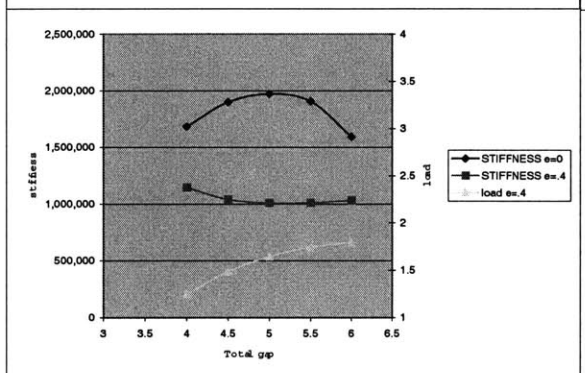

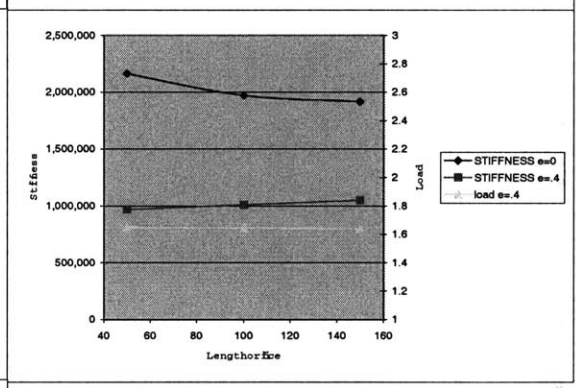

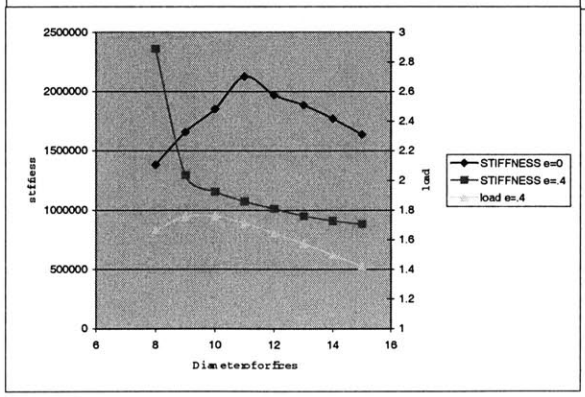

if not specified otherwise :
P = 8 atm
N = 60
gap = 5 um
L = 100 um
D = 12 um

Appendix F

Turbopump masks

Level : 1
Side : FRONT
Wafer Thickness : 450um
Etch Depth : 350um
Etch # : 1/1 front, 1/2 total
Haloes : no

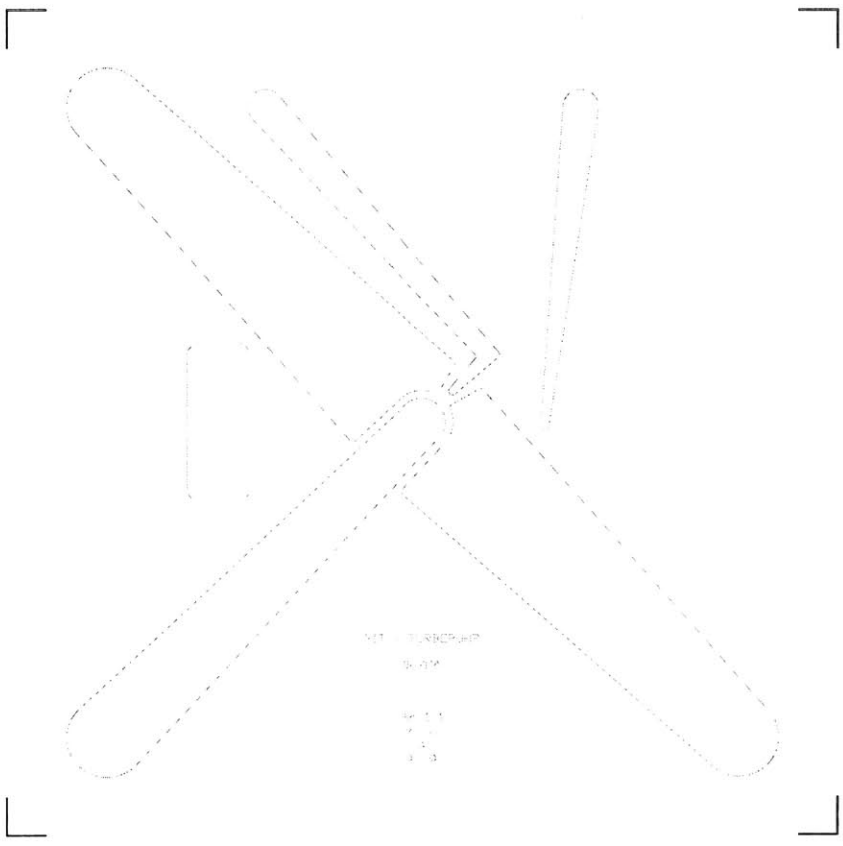

Level : 1
Side : BACK
Wafer Thickness : 450um
Etch Depth : 100um
Etch # : 1/1 back, 2/2 total
Haloes : no

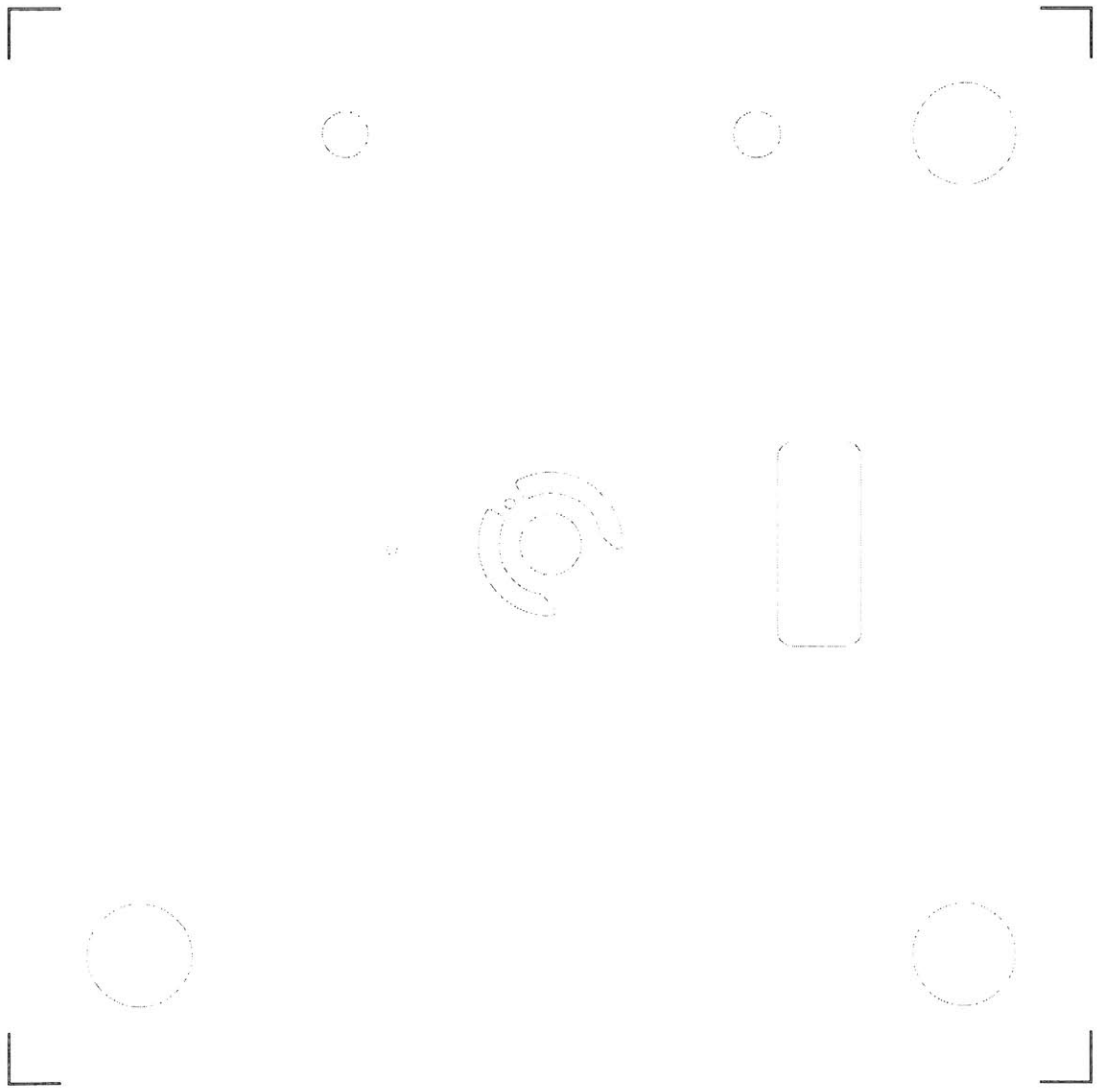

Level : 2
Side : FRONT
Wafer Thickness : 450um
Etch Depth : 350um
Etch # : 1/1 front, 1/3 total
Haloes : no

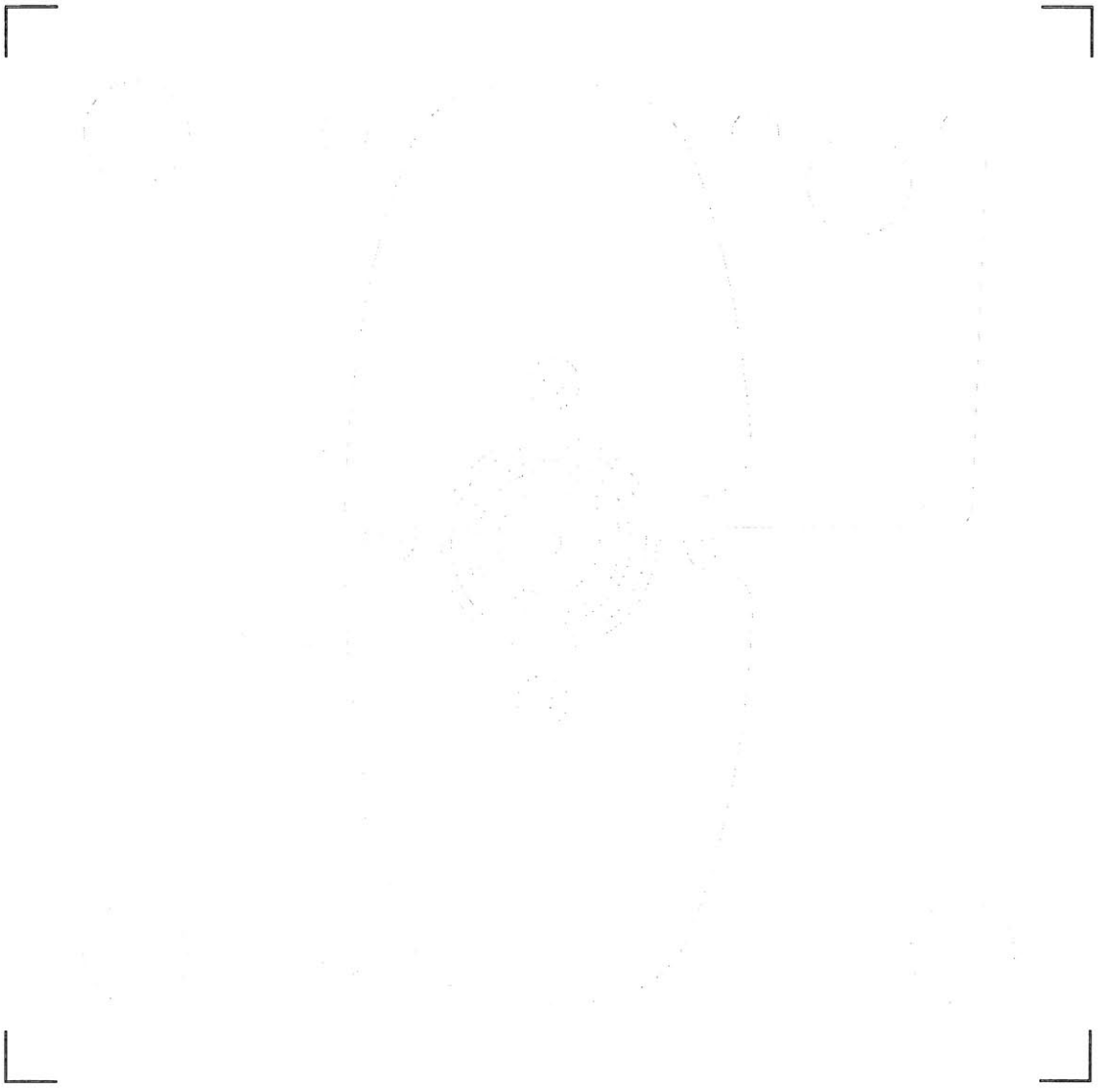

Level : 2
Side : BACK
Wafer Thickness : 450um
Etch Depth : 20um - TIP-CLEARANCE
Etch # : 1/2 back, 2/3 total
Haloes : no

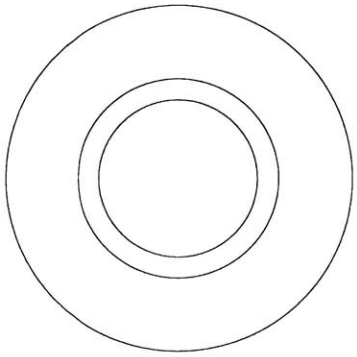

Level : 2
Side : BACK
Wafer Thickness : 450um
Etch Depth : 100um
Etch # : 2/2 back, 3/3 total
Haloes : 30um

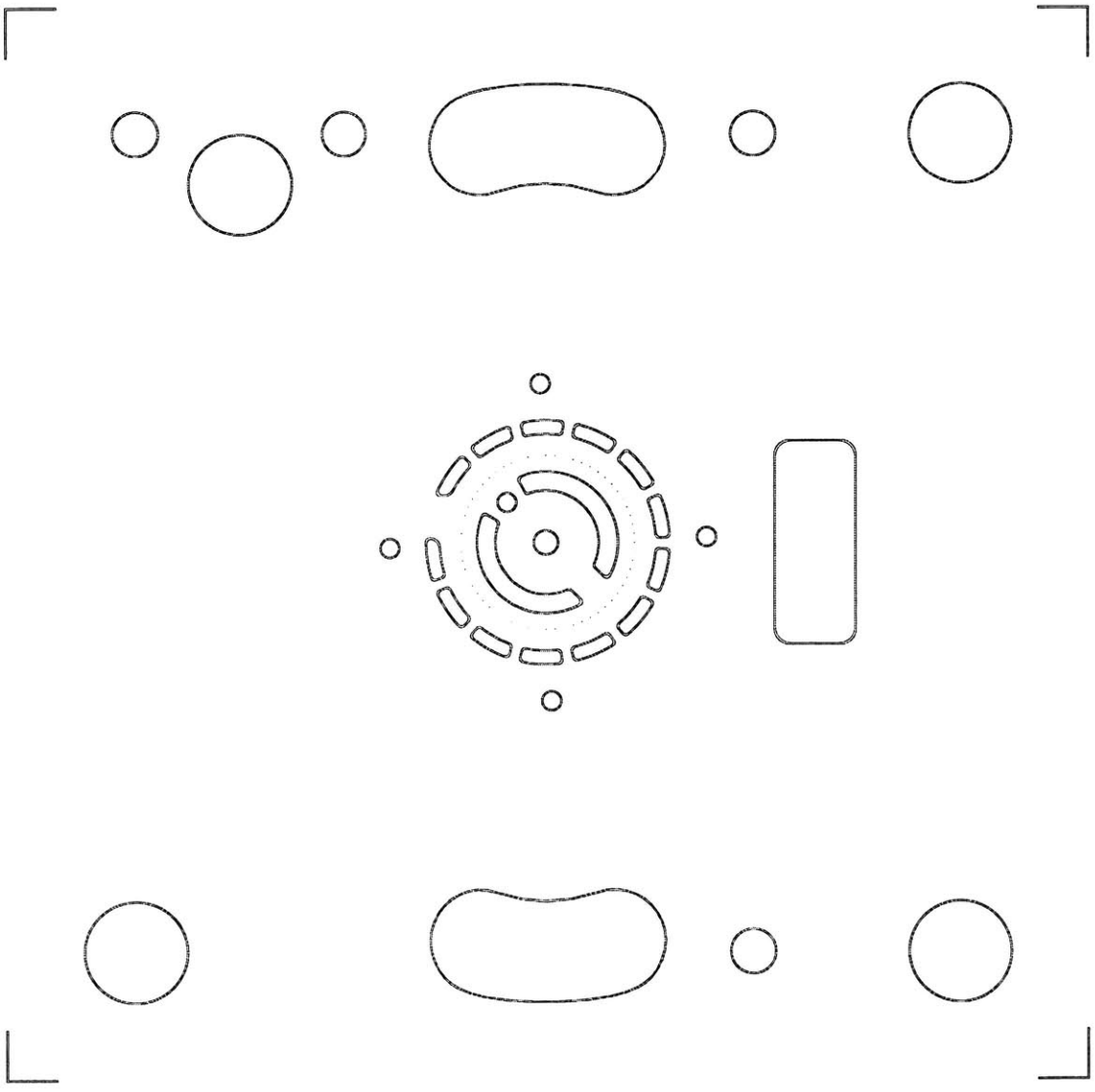

Level : 3
Side : FRONT
Wafer Thickness : 525um
Etch Depth : 0.5um - OXIDE ETCH FOR ROTOR RELEASE
Etch # : 1/2 front, 1/3 total
Haloes : no

Level : 3
Side : FRONT
Wafer Thickness : 525um
Etch Depth : 225um
Etch # : 2/2 front, 2/3 total
Haloes : no

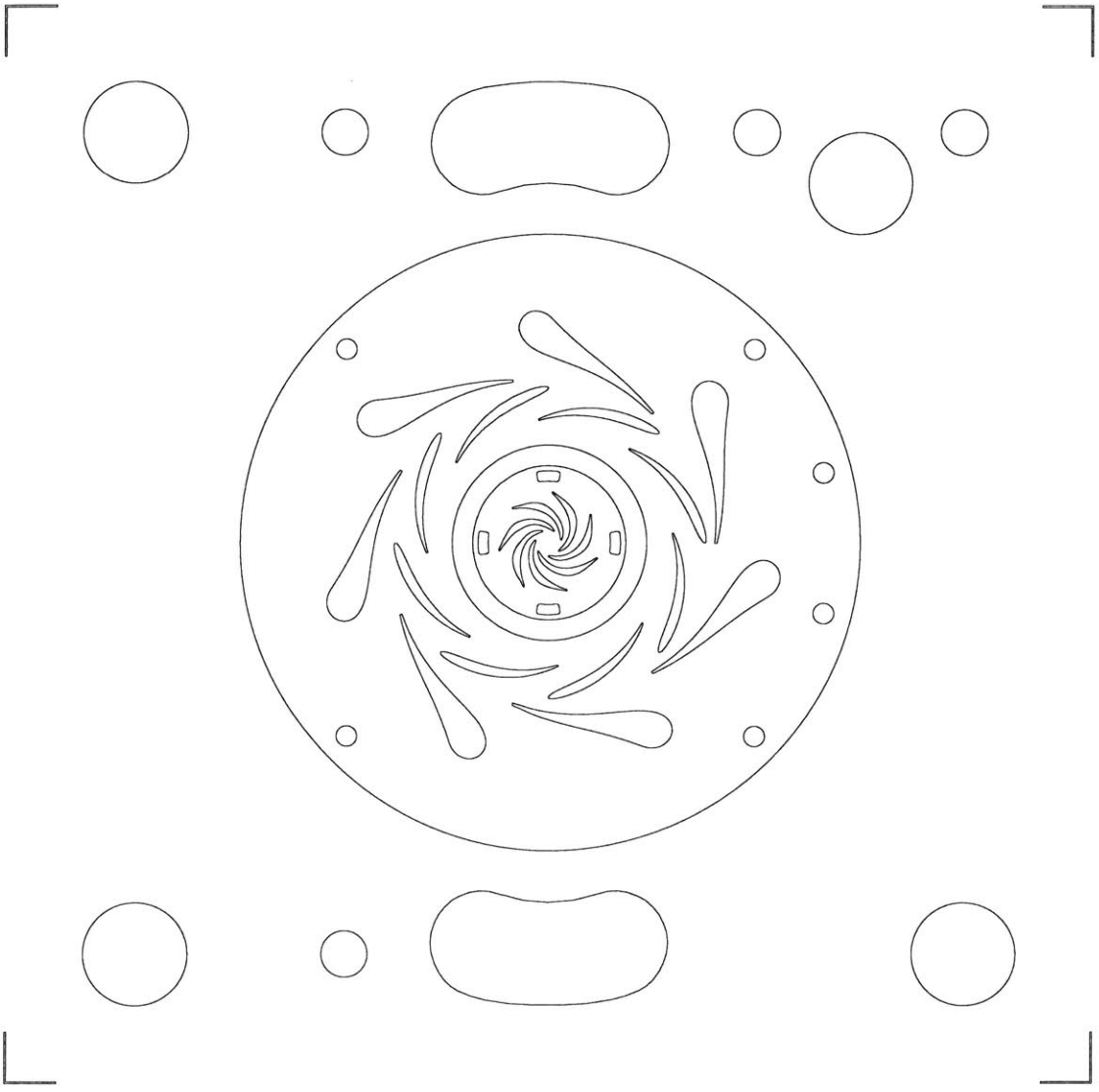

Level : 3
Side : BACK
Wafer Thickness : 525um
Etch Depth : 300um - JOURNAL BEARING
Etch # : 1/1 back, 3/3 total
Haloes : 4um, 6um and 12um

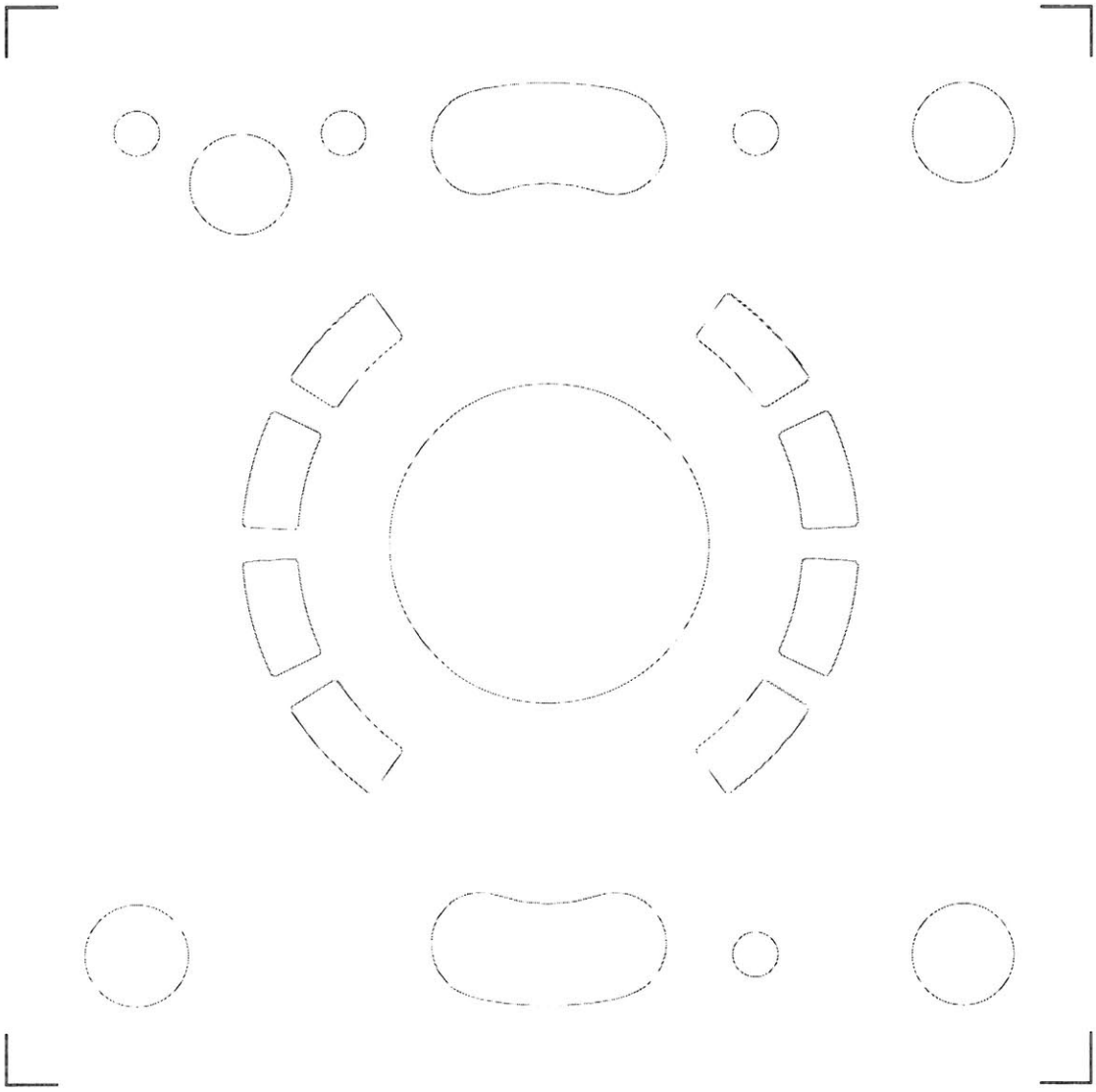

Level : 4
Side : FRONT
Wafer Thickness : 450um
Etch Depth : 4.5um - THRUST BEARING GAP
Etch # : 1/3 front, 1/4 total
Haloes : no

Level : 4
Side : FRONT
Wafer Thickness : 450um
Etch Depth : 50um - BACK PLENUM GAP
Etch # : 2/3 front, 2/4 total
Haloes : no

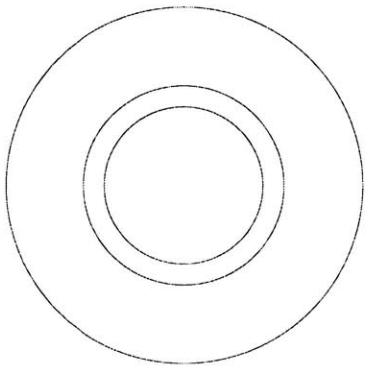

Level : 4
Side : FRONT
Wafer Thickness : 450um
Etch Depth : 100μm
Etch # : 3/3 front, 3/4 total
Haloes : no

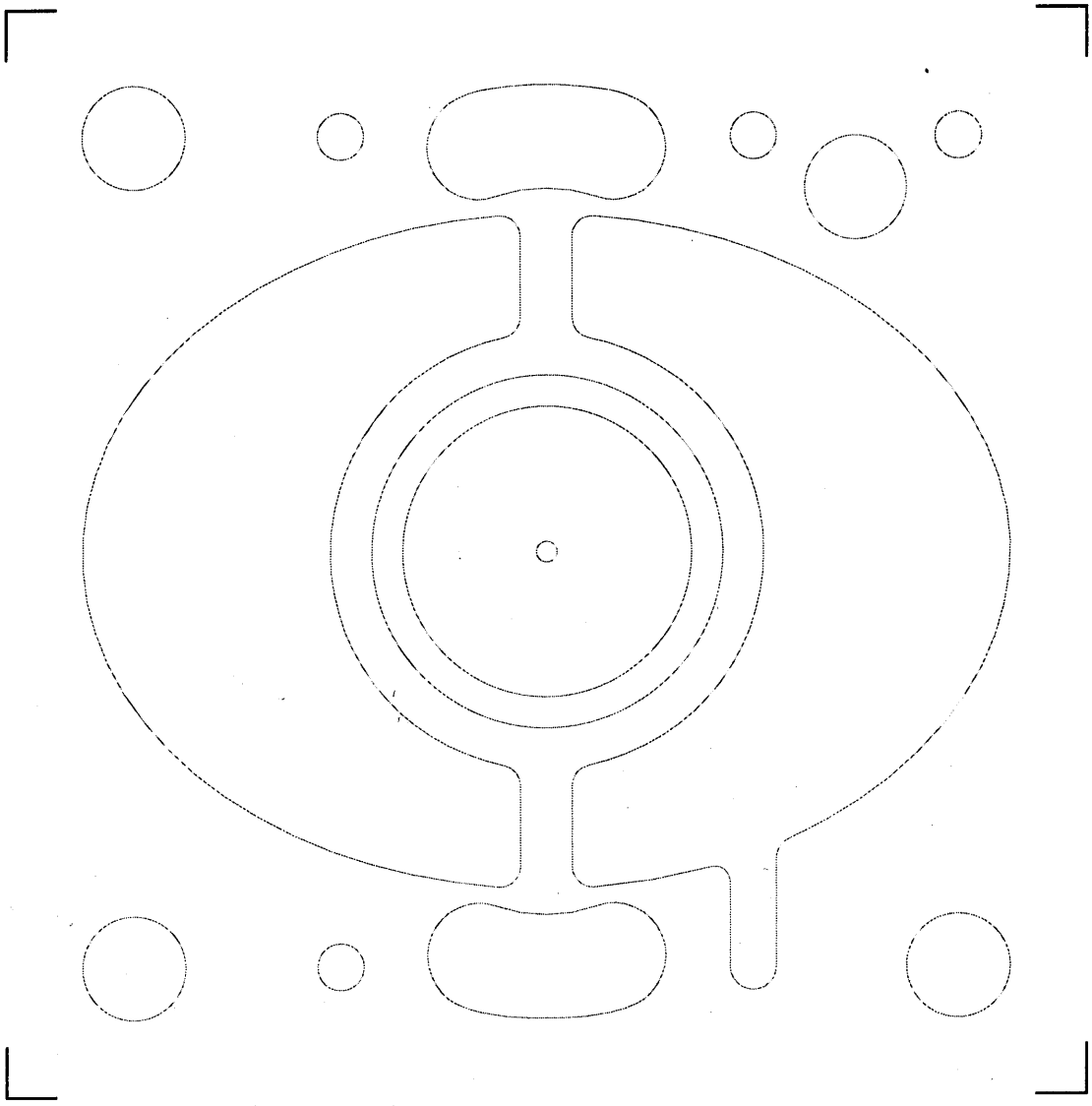

Level : 4
Side : BACK
Wafer Thickness : 450um
Etch Depth : 350um
Etch # : 1/1 back, 4/4 total
Haloes : no

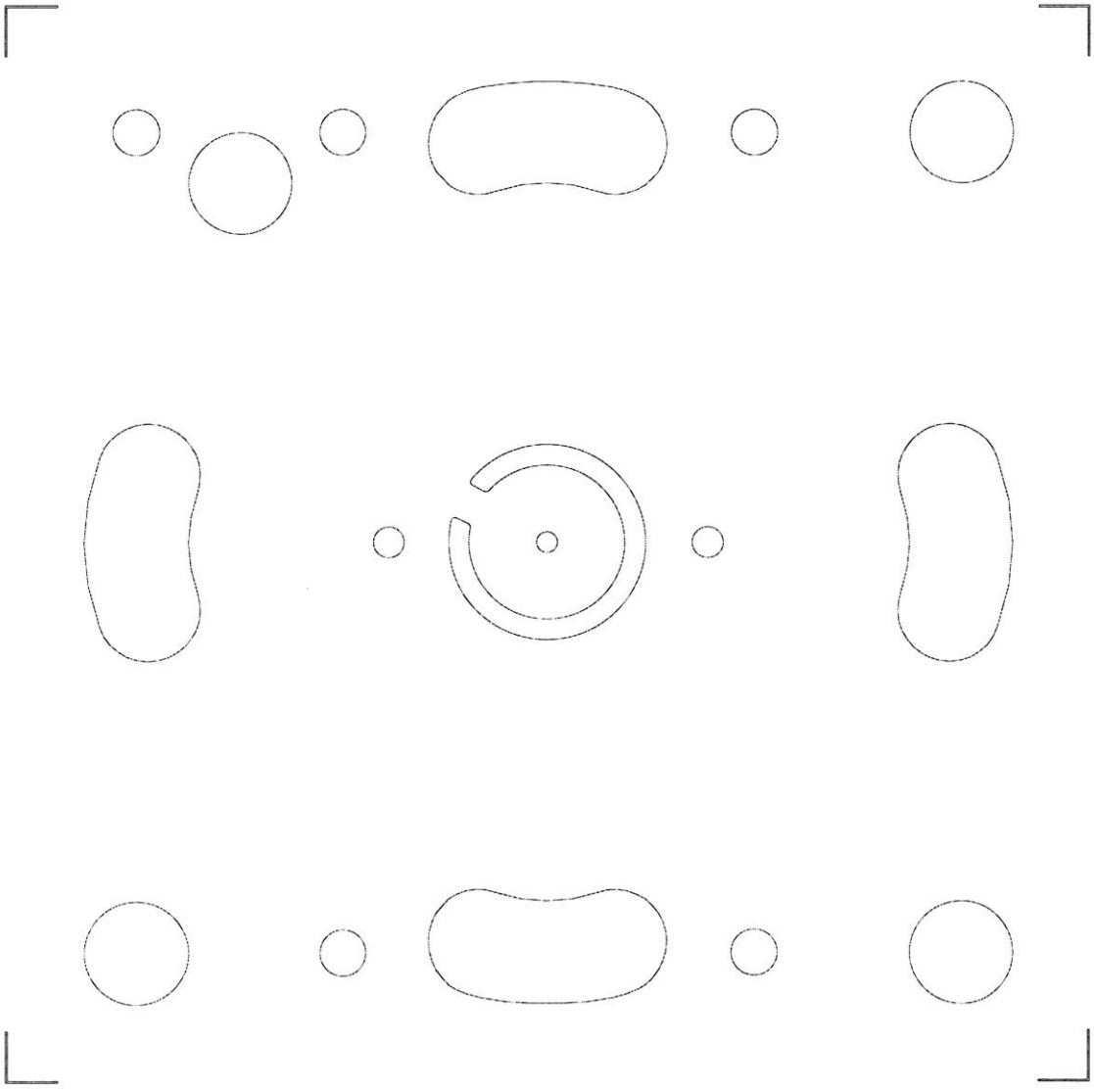

Level : 5
Side : FRONT
Wafer Thickness : 450um
Etch Depth : 350um
Etch # : 1/1 front, 1/2 total
Haloes : no

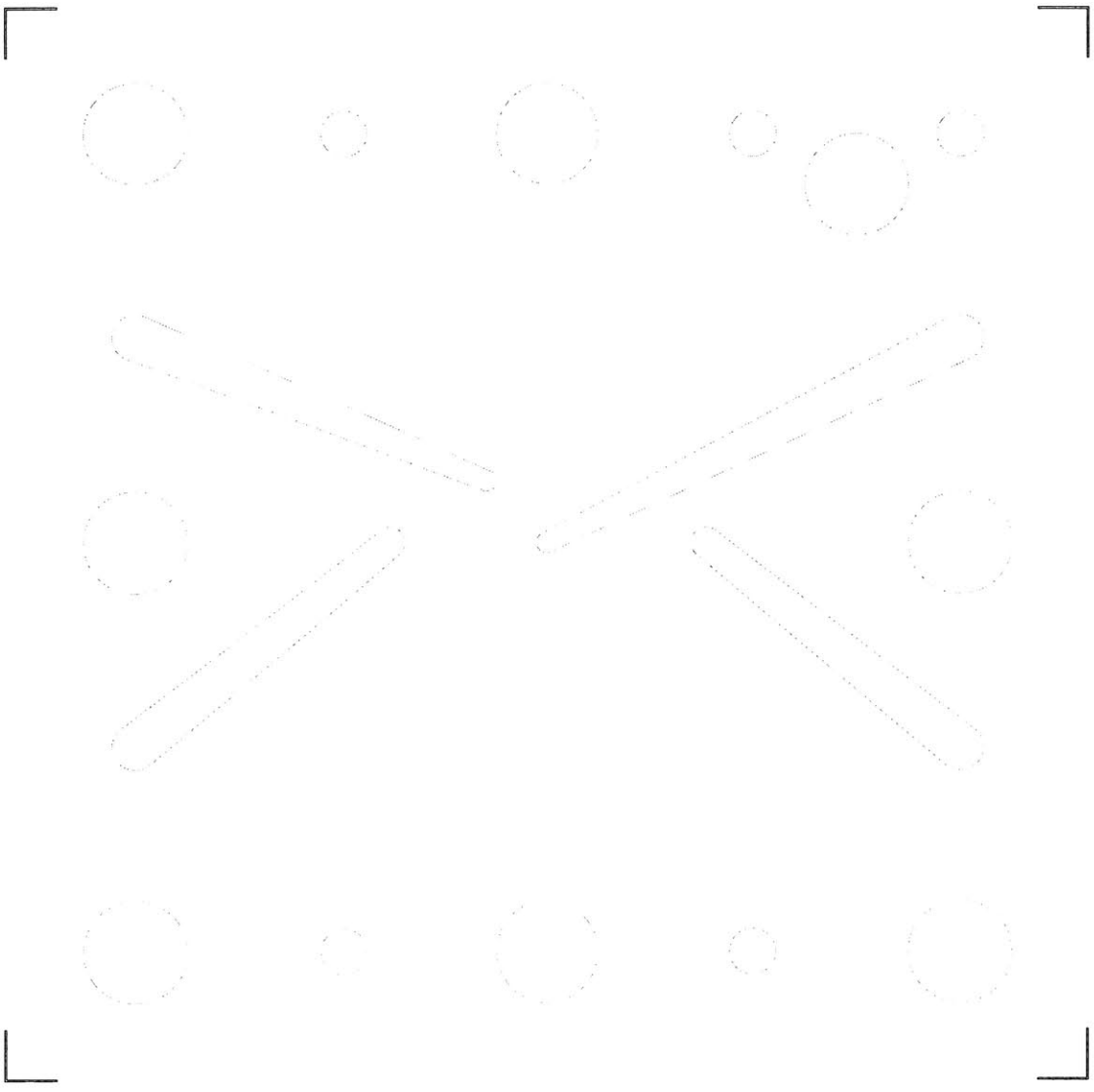

Level : 5
Side : BACK
Wafer Thickness : 450um
Etch Depth : 100um
Etch # : 1/1 front, 2/2 total
Haloes : no

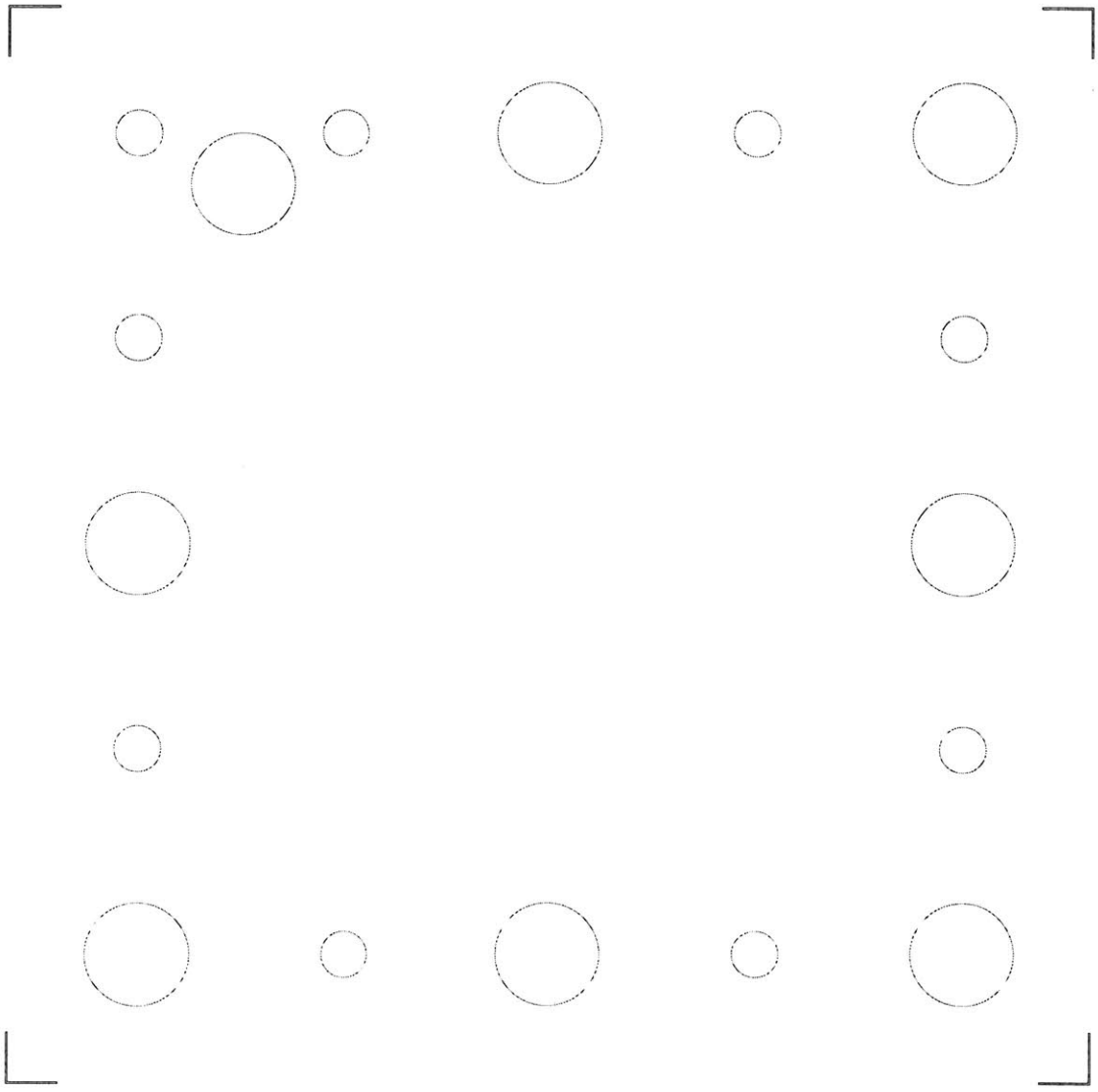

Bibliography

[1] *Design of gas bearings.* Mechanical Technology Incorporated.

[2] R. A. Braff R. Khanna-H. H. Sawin M.A. Schmidt A. A. Ayon, D. Z. Chen. A novel integrated process using fluorocarbon films deposited with a deep reactive ion etcher. *presented at the Fall meeting of the Materials Research Society, Boston, MA*, Nov. 29 - Dec. 3, 1999.

[3] G. Anathasuresh A Ayon K. Breuer K-S Chen F. Ehrich E. Esteve G. Gauba R. Ghodssi C. Groshenry S. Jacobson J. Lang C-C Lin A. Mehra J. Mur Miranda-S. Nagle D.J. Orr E. Piekos M. Schmidt G. Shirley S. Spearing C. Tan Y-S. Tzeng I. Waitz A.H. Epstein, S.D. Senturia. Power mems and microengines. *presented at IEEE Conference on Solid State Sensors and Actuators, Chicago, IL.*

[4] O. Al-Midani G. Anathasuresh A Ayon-K. Breuer K-S Chen F. Ehrich E. Esteve L. Frechette G. Gauba R. Ghodssi C. Groshenry-S. Jacobson J. Kerrebrock J. Lang C-C Lin A. London J. Lopata A. Mehra J. Mur Miranda S. Nagle D.J. Orr-E. Piekos M. Schmidt G. Shirley S. Spearing C. Tan Y-S. Tzeng I. Waitz A.H. Epstein, S.D. Senturia. Micro-heat engines, gas turbines, and rocket engines - the mit microengine project. *presented at the 28th AIAA Fluid Dynamics Conference and the 4th AIAA Shear Flow Control Conference, Snowmass Village, CO No. 97-1773*, June 1997.

[5] Omar Al-Midani. Preliminary design of a liquid bipropellant microfabricated rocket engine. Master's thesis, Massachusetts Institute of Techonology, Department of Aeronautics and Astronautics, June 1998.

[6] Kurt Broderick. personal communication.

[7] S.P. Carfagno and J.T. McCabe. *Summary of investigations of entrance effects on circular thrust bearings.* Franklin Institute Research Laboratories Technical Report I-A2049-24.

[8] Cole Parmer Instrument Company. Vernon Hills, IL, USA.

[9] Mark Drela. *Two-dimensional transonic aerodynamic design and analysis using Euler equations.* Phd thesis, Massachusetts Institute of Techonology, 1986.

[10] Fred F. Ehrich. personal communication.

[11] Alan Epstein. personal communication.

[12] S.A. Jacobson-F.F. Ehrich K.S. Breuer E.S. Piekos, D.J. Orr. Design and analysis of microfabricated gas journal bearings. *AIAA Paper AIAA-97-1966*, June 1997.

[13] Luc Fréchette. *Development of a microfabricated silicon motor-driven compression system.* Phd thesis, Massachusetts Institute of Techonology, Department of Aeronautics and Astronautics, September 2000.

[14] Erwin Fried. *Flow resistance - a design guide for engineers.* IE Idelchick, 1989.

[15] Dongqing Li Gh. Mohiuddin Mala. Flow characteristics of water in microtubes. *International Journal of Heat and Fluid Flow*, (20):142–148, 1999.

[16] Yifang Gong. personal communication.

[17] Melles Griot. Albany, New York, USA.

[18] Bernard J. Hamrock. *Fundamentals of Fluid Film Lubrication.* McGraw-Hill, 1994.

[19] I.E. Idelchik. *Handbook of hydraulic resistance.* 3rd ed, CRC Press, 1994.

[20] Stuart Jacobson. personal communication.

[21] Laurent Jamonet. personal communication.

[22] J.E. Jones. Whip vibrations on journal bearings. Master's thesis, Massachusetts Institute of Techonology, Department of Mechanical Engineering, 1957.

[23] Carole Joppin. personal communication.

[24] Jack L. Kerrebrock. *Aircraft Engines and gas Turbines.* The MIT Press, 1996.

[25] Chuang-Chia Lin. *Development of a microfabricated turbine-driven air bearing rig.* Phd thesis, Massachusetts Institute of Techonology, Department of Mechanical Engineering, 1999.

[26] Adam London. *Development and test of a microfabricated bipropellant rocket engine.* Phd thesis, Massachusetts Institute of Techonology, Department of Aeronautics and Astronautics, June 2000.

[27] Harold Youngren Mark Drela. A user's guide to mises 2.1. *MIT computational aerospace sciences laboratory*, 1995.

[28] Doyle J. Orr. *Macro-scale investigation of high speed gas bearings for MEMS devices.* Phd thesis, Massachusetts Institute of Techonology, Department of Aeronautics and Astronautics, 2000.

[29] L.J. Kircka P. Wilding, M.A. Shoffner. Manipulation and flow of biological fluids in straight channels micromachined in silicon. *Clin. Chem.*, pages 40:43–47, 1994.

[30] Yoav Peles. personal communication.

[31] Sumita Pennathur. Cavitation. Master's thesis, Massachusetts Institute of Techonology, Department of Aeronautics and Astronautics, June 2001.

[32] Baudoin Philippon. personal communication.

[33] Christopher Protz. Systems analysis of a microfabricated storable bipropellant rocket engine. Master's thesis, Massachusetts Institute of Techonology, Department of Aeronautics and Astronautics, January 2000.

[34] Jonathan Protz. *An assessment of the aerodynamic, thermodynamic, and manufacturing issues for the design, development, and microfabrication of a demonstration micro engine.* Phd thesis, Massachusetts Institute of Techonology, Department of Aeronautics and Astronautics, September 2000.

[35] H.H. Richardson R.H. Larson. A preliminary study of whirl instability for pressurized gas bearings. *Journal of Basic Engineering*, pages 511–520, December 1962.

[36] W.B. Rowe. *Hydrostatic and Hybrid Bearing Design.* Butterworths, 1983.

[37] Nicholas Savoulides. Low order models for hybrid gas bearings. Master's thesis, Massachusetts Institute of Techonology, Department of Aeronautics and Astronautics, February 2000.

[38] Stephen D. Senturia. personal communication.

[39] John Tuzson. *Centrifugal pump design.* John Wiley & Sons, 2000.

[40] J.H. Vohr. An experimental study of flow phenomena in the feeding region of an externally pressurized gas bearing. *Paper presented at the ASME 1966 spring lubrication symposium in New Orleans, LA.*

[41] Alfred Kruse Wolfgang Wagner. *Properties of water and steam.* Springer-Verlag, 1998.

[42] Chee-Wei Wong. Design, fabrication, experimentation and analysis of high-speed microscale gas bearings. Master's thesis, Massachusetts Institute of Techonology, Department of Mechanical Engineering, January 2001.

[43] et al. X.N. Jiang. *Transducers 95*, pages 317–320, Stockholm, Sweden, June 25-29, 1995.

[44] Harold Yougren. personal communication.